Sintering of
Aerosol Agglomerates

Thesis by

Melissa Mae Lunden

In Partial Fulfillment of the Requirements

for the Degree of

Doctor of Philosophy

Advisor: Professor Richard C. Flagan

California Institute of Technology

Pasadena, California

1995

(Submitted May 26, 1995)

Acknowledgements

First and foremost, I would like to thank my advisor, Dr. Richard Flagan, for constant encouragement during a long and arduous process. He allowed me enough freedom to fully explore all aspects of the project, even though it must have seemed at times that I was lost. I enjoyed our many enthusiastic discussions concerning all aspects of the research (and science in general), and I hope that they can continue.

Additional thanks go to others who helped me to complete my research. Discussions with Dr. Channing Ahn helped to get a grasp on my image processing tasks. Pat Koen assisted me with microscopy and photo processing, and was always there to discuss golf, baseball, and other important scientific matters.

The members of the joint Flagan/Seinfeld/Cass group made my stay here an enjoyable one. To those that were here when I arrived, and who taught me all the fine points of working in the lab, I am grateful: Barb Wyslouzil, Hung Nguyen, Steve Rogak, Rob Harley, and Martha Shaw. To those that helped me finish, I am indebted: Lynn Russell, Hali Forstner, Pat Chuang, Shouhua Zhang, Donald Dabdub, and Richard McClurg. I would happily share a 9/16ths wrench with any of them. I have also had the honor to share office space with two of the best, Aaron Rulison and Paul Drayton. They suffered through my failures and triumphs, and helped me with many thing, both scientific and non. Their constant support helped me to perservere.

In addition, I have had the pleasure of sharing many non-scientific hours with a great group of friends. Special thanks go to the members of the scum; Mike Rock, Dan Jones, Steve and Laura Buratto, Gary and Dawn Guthart, and Marc Hillmyer.

Our adventures were often epic, and never dull, and have filled with good memories of card games, softball, and evenings at the bungelow. I also thank Bill and Delores Bing, Phoebe Ray, Chris Price, and Jamie Schlessman for helping me to fullfill my musical interests. Most of all, I would like to thank Alison McCurdy and Wayne Larson...I could not ask for two better friends.

Finally, I thank my family for all their unwavering support. A special thanks to my father, who first put my feet on the path of knowledge and taught me that I could do anything. Sometimes, I think he left his slide rule out on purpose to try to win me over to all things engineering at an early age. And also to my mother, who saw to it that I had experiences that were decidedly non-scientific, and who helped to keep me focussed these last few months. And last, but not least, to my "additional" parents; Liz for her unconditional support and pep talks, and George for his words of encouragement and true understanding of the task at hand.

Abstract

Fundamental studies of the sintering of aerosol agglomerates have been undertaken. A model has been developed that closely follows the sintering kinetics of the two-sphere system. The model solves a detailed description of the evolving geometry as the particles sinter, allowing neck growth to be calculated beyond the small neck limit. Contributions due to multiple mechanisms are calculated by integrating the sum of the individual sintering mechanism fluxes. It has been demonstrated that the relative contributions of individual mechanisms can change as the neck grows. Moreover, changes in sintering temperature can drastically alter which of the sintering mechanisms is predominant.

Experiments performed on model bisphere show that neck formation occurs quickly, until the difference between the surface free energy and the grain boundary energy of the aggregate becomes small. This metastable configuration depends upon the equilibrium, or dihedral, angle of the particle. Following neck growth, coalescence proceeds slowly.

The projected area and hence, the mobility-equivalent diameter of an agglomerate will generally decrease as coalescence occurs. However, experimental observations of larger model agglomerates reveal some unexpected behavior, including apparent increases in the mobility-equivalent size. These effects may be caused by particle orientation in the mobility classifier. It is postulated that the rotation of individual particles to preferred grain boundary orientations leads to an increase in the projected area of the particle during sintering.

Contents

List of Figures

List of Tables

Chapter 1

Introduction

Sintering is the movement of material, usually through diffusion, that results in the bonding and densification of a system of particles. An important process in the ceramic industry, sintering is the final processing step where a compact of loosely packed or pressed powder adhere together to form a dense, solid body. The driving force for sintering is the excess surface free energy of the particle system. Changes in curvature create corresponding differences in vapor pressure over neighboring surfaces and gradients in the chemical potential, causing material to migrate to the neck region between two contacting particles. Simple theoretical models of the sintering kinetics have been developed, but they are limited by assumptions concerning the particle morphology and material transport mechanisms.

Sintering has lately been recognized as an important process in the aerosol synthesis of refractory particles from the vapor phase. In these aerosol systems, particles form by nucleation of supersaturated vapor, and grow primarily by coagulation of solid particles. While the particles are small, they coalesce rapidly upon coagulation.

As the aerosol population grows and the temperature decreases, sintering slows until the particles only partially coalesce as they coagulate. The particles that then result are aggregates with complex structures. An understanding of the competing kinetics of coalescence and sintering is necessary to predict the final agglomerate structure. A number of heuristic models have been devised that incorporate a coalescence term into the aerosol population balance equations. However, little attention has been paid to the fundamental processes involved in the sintering term in the development of these models.

The focus of this document is to develop a clearer understanding of the physical processes involved in sintering. To that end, a thorough review of the development of the sintering flux equations is presented in Chapter 2. Care is taken to derive flux equations with as few assumptions as possible so that they can be used to model the entire neck growth process. A review of the traditional neck growth equations is presented, with the assumptions involved in arriving at these relations clearly stated. The proposed coalescence terms for use in models of agglomerate growth are described, and the underlying assumptions discussed.

Chapter 3 outlines a dynamic model that closely follows the sintering kinetics. A detailed description of the evolving geometry of the two-sphere system is presented. The model allows for the integration of all relevant sintering mechanisms. Results from the model are compared to previous modeling work and experimental data from the literature.

Experiments involving the sintering of model aerosol agglomerates are discussed

in Chapter 4. We have produced bisphere silicon agglomerates by low temperature coagulation of dense spheres. The bispheres were processed at high temperatures while still entrained in the gas stream. This enables detailed study of the structural changes due to sintering. Structural information was obtained from Transmission Electron Microscopy (TEM) observations of individual particles. Results are compared to the model developed in Chapter 3.

Chapter 5 describes sintering studies of larger agglomerates of silicon particles, with the focus on the mobility changes due to the structural evolution of the particles due to sintering. Model agglomerates were produced by low temperature coagulation of dense, spherical particles. Changes in particle mobility were measured using a differential mobility analyzer. Limited morphological information was obtained from TEM observations.

Chapter 2

A Review of Solid-State Sintering Models

2.1 Introduction

Sintering is an important step in the production of ceramics. During sintering, a compact of loosely packed or pressed powder adhere and grow together to form a dense, solid body. During processing, a mixture of ceramic powder, water, and a binder is pressed into a mold. The resulting compact contains about 25 to 60 percent porosity [1]. Increasing the density of the green compact improves material properties including strength, electrical or thermal conductivity, or corrosion resistance. The final processing step, sintering generally takes place in furnaces at temperatures below the melting point of the solid. As the particles in the compact sinter, they change shape, increase in size, and eventually leave only isolated pores in a continuous solid.

The driving force for sintering is the excess surface free energy of the particle system. Changes in surface curvature create corresponding differences in pressure on neighboring surfaces, gradients in chemical potential, and differences in local surface

tension. Sintering usually occurs by solid-state diffusion, but in some cases it is aided by a liquid phase. To decrease their surface energy, particles will change their shape, either rounding sharp edges or developing facets that favor low energy lattice planes. Necks that form between particles substitute lower energy grain boundary area for surface area. These effects can be quite large for small particle sizes, i.e., below a few microns in radius. The net decrease in free energy from sintering 1 micron sized material is on the order of 1 cal/g [1].

Sintering also plays an important role in the formation of refractory aerosol particles. The process begins upon cooling of vapor-laden gases to produce a supersaturated state. Homogeneous nucleation then produces a large number of very fine particles that undergo rapid coagulation. Process temperatures in powder synthesis reactors are generally below the melting point of the material, so the coagulating particles are solid. Initially, when the particles are small, they coalesce rapidly upon coagulation. As the particles grow, however, sintering slows to the point that particles only partially coalesce between coagulation events. The particles then grow as agglomerates with complex ramified structures that are often described as "fractal-like." Predictions of the structures that evolve requires an understanding of the competing coagulation and sintering kinetics. For a few applications, particles with large specific surface area are preferred, but the ideal powder for most ceramic applications consists of spherical, non-aggregated particles.

Frenkel[2] and Kuczinski [3] pioneered the theoretical description of sintering. Kuczinski devised a simple geometrical model for sintering using a sphere on a plate.

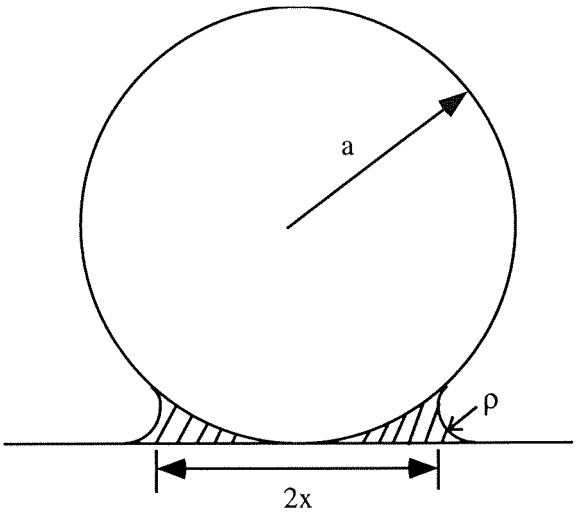

Figure 2.1: The first geometry for sintering as described by Kuczinski.

(Fig. 2.1) The early phase of sintering was described in terms of the growth of the neck between the sphere and the plate by a single transport mechanisms in terms of the neck radius, i.e.,

$$\left(\frac{x}{a_i}\right)^n = \frac{B(T)}{a_i^m} t \tag{2.1}$$

where a_i is the initial particle radius, m and n depend on the individual sintering mechanism, and t is time. $B(T)$ is a term that contains relevant material properties that is a function of temperature T. These growth expressions are based upon simplified system geometries that limit their applicability to a neck radius ratio below $x/a_i \approx 0.3$. Later investigators developed and refined equations of the form Eq. (2.1) for additional transport mechanisms [4, 5, 6, 7]. There have been a few attempts to model the evolving particle morphology more accurately, but few couple the kinetics with the geometry [8, 9, 10, 11]. Most recent modeling efforts have focused on the densification of systems of particles and the behavior of pores within these systems

[12, 13, 14, 15, 16]. Others have performed extensive numerical calculations for the coalescence of the two-sphere system under the surface-tension-driven flow of viscous sintering [17, 18, 19, 20].

A number of investigators [21, 22, 23, 24, 25, 26, 27, 28] have applied the simple early-stage neck growth models to the structural evolution of agglomerating aerosol particles. Most of these models are phenomenological descriptions of simultaneous coagulation and coalescence, with little attention being paid to the sintering term. A physically based sintering term is needed for inclusion in an agglomerate evolution model. This paper reviews sintering theory with an eye toward application to aerosol agglomerates.

2.2 Basic Principles

The primary objective of theoretical treatments of sintering is understanding the mechanisms of material transport in the system and their respective contributions to neck growth. These contribution's depend on the physical properties of the material as well as such parameters as particle size, temperature, or time. Six transport mechanisms are thought to contribute to the movement of material during sintering. These transport pathways are illustrated in Fig. 2.2. The mechanisms include evaporation and condensation, surface diffusion, grain boundary diffusion, two distinct forms of volume diffusion, and viscous flow. Evaporation and condensation is the movement of material through the vapor phase. Volume, surface, and grain boundary diffusion move material through the system via the volume, surface, or grain boundary of the

lattice. Viscous flow is a process of slow deformation under the influence of surface tension where the solid viscosity is related to the self diffusion coefficient of that material.

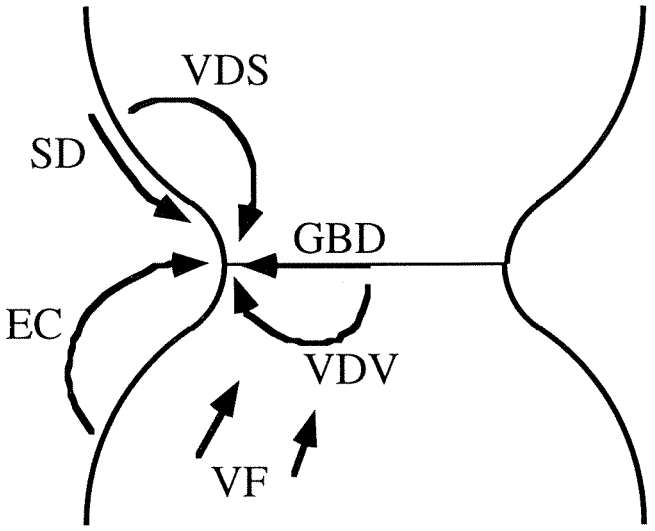

Figure 2.2: Material movement pathways for the different sintering mechanisms: Evaporation and Condensation (EC), Surface Diffusion (SD), Grain Boundary Diffusion (GBD), Volume Diffusion from the Interior of the Particle (VDV), Volume Diffusion from the Surface of the Particle (VDS), and Viscous Flow (VF).

Study of the sintering behavior for simple model geometries has proved valuable. Beginning with the work of Frenkel and Kuczinski [2, 3], the description of the spherical or cylindrical systems has provided important physical understanding of sintering, particularly for the early stages of neck growth. Experimentally, neck growth has been measured from heat treated systems of spheres or wires. The data were generally fitted using Eq. (2.1) and the resulting values of n were used to elucidate which transport mechanism predominates. Some of the experimental results are reviewed in Table 2.1. Once the predominant mechanism had been identified, the neck growth data were often used in combination with the sintering rate equation to

calculate the diffusion coefficients relevant to the identified mechanism.

Material	Exponent n	Implied Mechanism	Ref.
Alumina	5 - 6	Volume Diffusion (S & V)	[29]
Copper	5	Volume Diffusion	[3]
	5.0-5.5	Volume Diffusion	[4]
	5.0	Volume Diffusion	[30]
Silver	5	Volume Diffusion	[3, 31]
Sodium Chloride	2.8-3.4	Evaporation & Condensation	[4]
Glass	2.1	Viscous Flow	[4]

Table 2.1: Experimentally determined values of the exponent n and implied sintering mechanism.

This method of analyzing the results from sintering experiments is complicated by the fact that it is rare that one mechanism dominates to such an extent that others can be neglected. [5, 6] In his work, Rockland [6] solved the equation for neck growth using both surface and volume diffusion contributions. By comparing the solution to results from copper, he found that although it seemed to fit the data, the solutions for surface and volume diffusion, while not giving as good a fit, came quite close. This result suggested that surface diffusion should not be neglected in this case. Moreover, it emphasized the ambiguity in inference of a single mechanism from such measurements. To further his point, Rockland showed that when relative contributions of surface, grain boundary, and volume diffusion are all considered for copper over a large range of temperatures, the mean exponent value was 5.3. Taken alone, this value would suggest that only volume diffusion was active. He concluded:

"The theoretical exponent of the rate equations and of the scaling equations are very sensitive to changes in variables during the process" and that "the determination of the mechanisms of sintering with the exponential method is a completely unreliable procedure."

Just as a single exponent (and a single mechanism) cannot be used to describe sintering for all processing conditions, the simple neck growth equations cannot describe the process past initial neck growth. The models require assumptions or approximations that can greatly influence the predictions as growth progresses. The most important of these are the "small neck" approximations that are based on simplified geometries for early growth times. The neglect of the grain boundary energy and the simplification of the morphology of the neck contour further limit the applicability of these models. In his review, Exner [32] states that "the agreement between experimentally determined values for shrinkage in aggregates of many particles and the theoretical equations for two particle models is often purely coincidental."

2.2.1 Driving Force

The driving force for sintering is the excess free energy in the system. Variations in local surface curvature manifest themselves as gradients in local pressures and, therefore, gradients in chemical potential and concentration of lattice vacancies. These gradients cause vacancies to diffuse to regions of lower energy or, concurrently, atoms to diffuse to regions of higher energy. Herring's [33] phenomenological description illustrates how such concentration gradients evolve. The area near the interface be-

tween the two particles has a large radius of curvature and a correspondingly high surface energy. This energy can be lowered by decreasing the surface area, with an accompanying increase in the interface volume. This increase in neck volume can only be generated by raising the concentration of vacancies in that region. If the surface area is convex, as on the surface of the particle, its surface free energy can be reduced by reducing the volume of the region that it bounds, leading to a decrease in the concentration of lattice defects. By these mechanisms, the neighboring convex and concave regions establish a concentration gradient that results in diffusion currents. In a powder, these diffusion currents cause particles to change their shapes by rounding sharp corners or developing facets in low energy configurations. Necks form between particles substituting lower energy grain boundary area for higher energy surface area. Eventually, as the particles coalesce, the grain boundary may migrate out of the system.

The change in total surface energy can be written as

$$dE = \gamma dA, \tag{2.2}$$

where γ is the specific surface energy. To model sintering kinetics, we require the change of energy due to a local change in volume. If a volume element, dV, is moved from a region with principle radius of curvature r_1 to a region of curvature r_2, the change in surface energy can be written as [32]

$$\frac{dE}{dV} = \gamma\left(\frac{1}{r_1} + \frac{1}{r_2}\right) = \sigma, \tag{2.3}$$

where dE/dV is equivalent to a stress. The volume under a concave surface, such as the neck regions, will be under a tensile stress ($\sigma < 0$), while the volume under a convex surface of the particle surface will be under a compressive stress.

The chemical potential of the material is related to the stress in the system by

$$\mu = \mu_0 + \sigma\Omega, \tag{2.4}$$

where μ_0 is the chemical potential under a flat surface and Ω is the atomic volume. The change in chemical potential can be related to the curvature in the system as

$$\mu - \mu_0 = \gamma\Omega\left(\frac{1}{r_1} + \frac{1}{r_2}\right). \tag{2.5}$$

The chemical potential can also be written as a function of the concentration of vacancies [34]

$$\mu = \mu_0 + kT\ln\frac{c}{c_0}, \tag{2.6}$$

and vapor pressure

$$\mu = \mu_0 + kT\ln\frac{P}{P_0}, \tag{2.7}$$

where c_0 and P_0 are the vacancy concentration and vapor pressure due to a flat surface. By combining Eq. 2.5 with Eqs. 2.6 and 2.7, the variation in vacancy concentration and vapor pressure with surface curvature become

$$\ln\frac{c}{c_0} = \frac{\gamma\Omega}{kT}(\frac{1}{r_1} + \frac{1}{r_2}), \tag{2.8}$$

the Gibbs-Thompson equation, and

$$\ln \frac{P}{P_0} = \frac{\gamma \Omega}{kT}(\frac{1}{r_1} + \frac{1}{r_2}), \tag{2.9}$$

the Kelvin equation.

Under the influence of these gradients in stress (Eq. 2.3), chemical potential (Eq. 2.8), and vapor pressure (Eq. 2.9), material migrates into the neck region between the two spheres. Several mechanisms contribute to the migration of material. The evolution of the bisphere system geometry depends on which mechanisms are active. Four mechanisms, evaporation-condensation, viscous flow, surface diffusion, and volume diffusion-S (material moves from the surface of the particle to the neck through the volume of the particle) involve migration of material from the particle surface toward the neck. These mechanisms are referred to as adhesion mechanisms. Because no material is removed from the area between the particles, the centers of the particles do not move towards one another. In the other mechanisms, i.e., grain boundary diffusion and volume diffusion-V (material moves from the interior of the particle near the grain boundary to the neck through the volume of the particle), migration of material from the region between the particles toward the neck causes the centers to move together. These mechanisms are called densification mechanisms because they cause shrinkage in the particle system.

Most sintering theories assume that the surface tension and diffusion coefficients are isotropic. This is not the generally true. The minimum energy surface may not be a sphere, but may include facets along preferred crystal orientations. High energy

grain boundaries may produce deep dihedral angles, complicating the neck geometry. Carbides and nitrides and other covalently bonded materials are the particularly difficult cases [35]. For the present, however, all discussion in this chapter will be confined to the isotropic assumption.

2.3 Individual Mechanism Flux Equations

To describe the rate of sintering, a description of the change of the volume of the neck (the shaded region shown in Fig. 2.3) as a function of time is needed. This change can be written as

$$\frac{dV}{dt} = AJ, \tag{2.10}$$

where A is the area through which the atoms are diffusing to the neck, and J is the flux for the specific mechanism. The key to writing the proper flux equation is to identify the volume that is changing and the area through which the atoms are diffusing to the volume.

If the concentration gradient is known, the flux can be written using Fick's equation

$$J = -D\nabla c. \tag{2.11}$$

In some cases it is more convenient to derive a stress gradient instead of a concentration gradient necessitating an expression for the flux as a function of stress. The flux

can be written as a function of chemical potential,

$$J = -\mathcal{M}\nabla\mu, \tag{2.12}$$

where the atom mobility, $\mathcal{M}$, can be written as a function of the diffusion coefficient using the Nersnt-Einstein relation

$$\mathcal{M} = \frac{D}{kT}. \tag{2.13}$$

Combining Eqs. (2.12) and (2.13) with the relation between chemical potential and stress, Eq. (2.4), gives flux as a function of the stress

$$J = -\frac{D}{kT}\nabla\sigma. \tag{2.14}$$

It is possible, given a flux relation and the appropriate flux field, to derive a model for the increase of the neck region due to sintering via several pathways.

Since Kuczinski's original attempt, there have been myriad attempts to formulate "new and improved" sintering models, resulting in a large and sometimes confusing number of differing models. In spite of this work, most sintering data cannot be fitted satisfactorily by any one model. The difficulty lies in the specification of the appropriate flux field and boundary conditions. This is due, in part, to the complex geometry involved. The difficulties are further compounded because multiple mechanisms are generally active. With these problems in mind, an historical review of the deriva-

tion of each mechanism will be presented. The relevant flux equation and associated volume and areas will be discussed first in general. Then the standard geometrical assumptions will be introduced, and the equations reduced to the traditional form of Eq. (2.1).

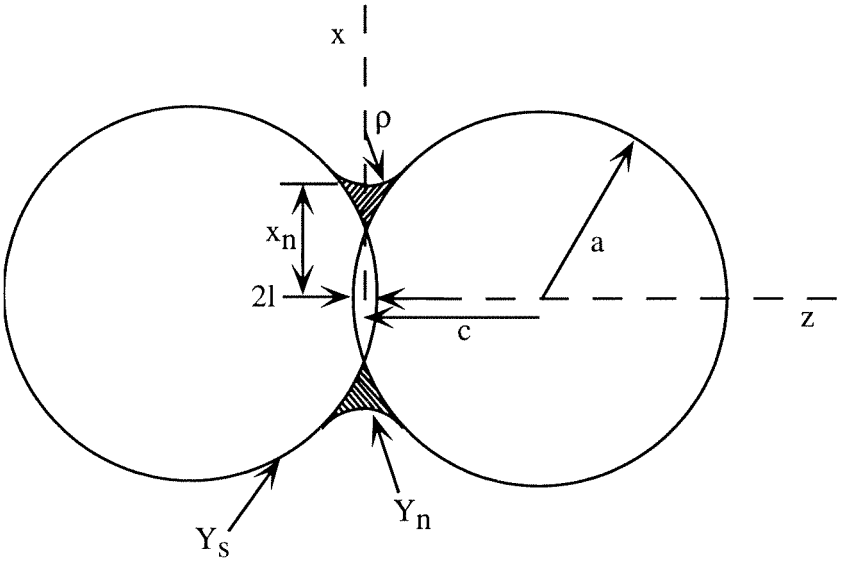

Figure 2.3: The two-particle sintering geometry. The shaded volume is the neck volume, V_{neck}.

Some definitions of the two-particle system are required for the following discussion. The standard geometry of the two-particle system is illustrated in Fig. 2.3. The radius of the sintering particle is a, the neck radius is x_n, and the radius of the neck interface is ρ. c denotes the location of the center of the particle from the plane of symmetry which divides the neck. The particle and neck surfaces are assumed to be circular, and the particles are assumed to maintain their spherical shape while sintering. The description of the neck and particle surfaces are defined as $Y_n(z)$ and $Y_s(z)$ respectively. The point at which the neck and particle surfaces meet is defined as z_i. The overlap between the two spheres is l. The volume of the neck is usually

described as a torus, and can be written as

$$V_{neck} = \int_0^{z_i} 2\pi Y_n(z)dz - \int_{c-a}^{z_i} 2\pi Y_s(z)dz. \tag{2.15}$$

2.3.1 Surface and Volume Diffusion-S

Surface and Volume Diffusion-S move material from the particle surface to the neck via the surface and the volume of the particle, respectively. They are grouped together because they share a common source of material, namely the surface of the particle, and are driven by similar gradient and flux conditions. The diffusion pathways of the two mechanisms are shown in Fig. 2.4. Both mechanisms were originally outlined by Kucyinski [3].

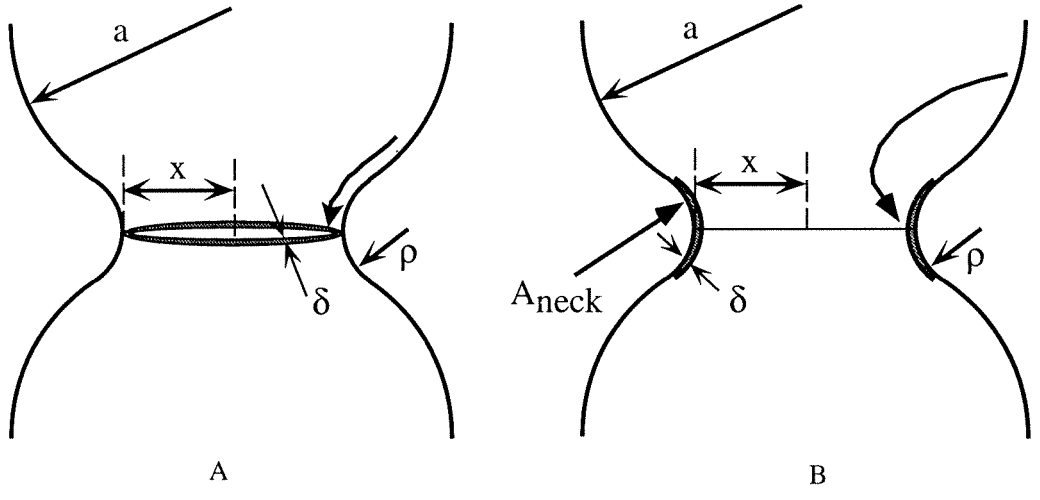

Figure 2.4: The diffusion pathways and flux areas for surface diffusion (A) and Volume Diffusion-S (B).

As discussed above, the variation in the concentration of vacancies due to surface

curvature (Eq. 2.8) is

$$\ln \frac{c}{c_0} = -\frac{\sigma\delta^3}{kT}\mathcal{K}, \tag{2.16}$$

where $\mathcal{K}$ is the difference in curvature between the neck and the particle surface for the two-sphere system, and can be written as

$$\mathcal{K} = \frac{1}{\rho} - \frac{1}{x} - \frac{2}{a}. \tag{2.17}$$

If we denote the vacancy concentration in terms of the deviation from the equilibrium value, $c = c_0 - \Delta c$ becomes

$$\ln \frac{c_0 - \Delta c}{c_0} = -\frac{\sigma\delta^3}{kT}\mathcal{K}. \tag{2.18}$$

To simplify this equation, let $\frac{c-\Delta c}{c} = 1 + x$, where $x = \frac{-\Delta c}{c}$. Then $\ln(1+x)$ can be expressed as

$$\ln(1+x) = x - \frac{1}{2}x^2 + \frac{1}{3}x^3 \ldots. \tag{2.19}$$

For small $\Delta c/c$, only the first order term is significant,

$$\ln \frac{c_0 - \Delta c}{c_0} \approx -\frac{\Delta c}{c_0}, \tag{2.20}$$

and Eq. (2.18) can be approximated by

$$\Delta c = \frac{\sigma\delta^3}{kT}\mathcal{K}c_0. \tag{2.21}$$

In the flux equation (Eq. 2.11) the concentration gradient, ∇c, is usually approximated by $\frac{\Delta c}{\Delta x}$, where Δc is estimated by approximating with Eq. 2.21 and Δx is estimated to be the length along the concave section of the neck, usually approximated as ρ. Substitution into Eq. (2.11) gives

$$J = -\frac{\sigma\delta^3}{kT\rho}\mathcal{K}c_0 D. \tag{2.22}$$

Equation (2.22) has been derived in terms of the concentration of vacancies in the neck region. The diffusion coefficient, D, is the coefficient of self-diffusion of vacancies. The equilibrium concentration of vacancies, c_0, can be written as

$$c_0 = e^{E_h/kT} \tag{2.23}$$

where E_h is the energy needed to create a hole in the lattice. The coefficient of volume self-diffusion is the product of the vacancy diffusivity and the equilibrium vacancy concentration, i.e.,

$$D_v = D_{h,v}e^{E_{h,v}/kT}, \tag{2.24}$$

and has units of cm^2/s. Equation (2.22) thus becomes

$$J = -\frac{\sigma\delta^3}{kT\rho}\mathcal{K}D_v. \tag{2.25}$$

Similarly, in the case of surface diffusion, the value of D in Eq. (2.22) becomes the coefficient of surface diffusion for vacancies, and c_0 becomes the energy needed to

create a vacancy near the surface. Equation (2.24) becomes

$$D_s = D_{h,s}e^{E_{h,s}/kT}, \tag{2.26}$$

where D_s also has units of cm^2/sec. In this case, the surface diffusion flux can be written as

$$J = -\frac{\sigma\delta^3}{kT\rho}\mathcal{K}D_s. \tag{2.27}$$

For volume diffusion, the area through which material diffuses into the neck is the total surface area of the concave region of the neck, i.e. the shaded region in Fig. 2.4a, and can be written as

$$A = 2\int_0^{Zi} 2\pi Y n(z)\sqrt{1+Yn^2(z)}dz. \tag{2.28}$$

In surface diffusion, the area through which material diffuses can be described as an annulus around the center of the neck, the shaded area in Fig 2.4b,

$$A = 2\pi x\delta. \tag{2.29}$$

2.3.2 Grain Boundary and Volume Diffusion-V

Grain boundary and volume diffusion-V both remove material from the area between the two particles, causing the particle centers to approach one another as the neck grows. The grain boundary is a high mobility path for atoms because it takes less energy for an atom to move along the boundary. It also serves as an efficient va-

cancy sink for volume diffusion. The diffusion pathways of the two mechanisms are illustrated in Fig. 2.5. Johnson first modeled these sintering mechanisms [7].

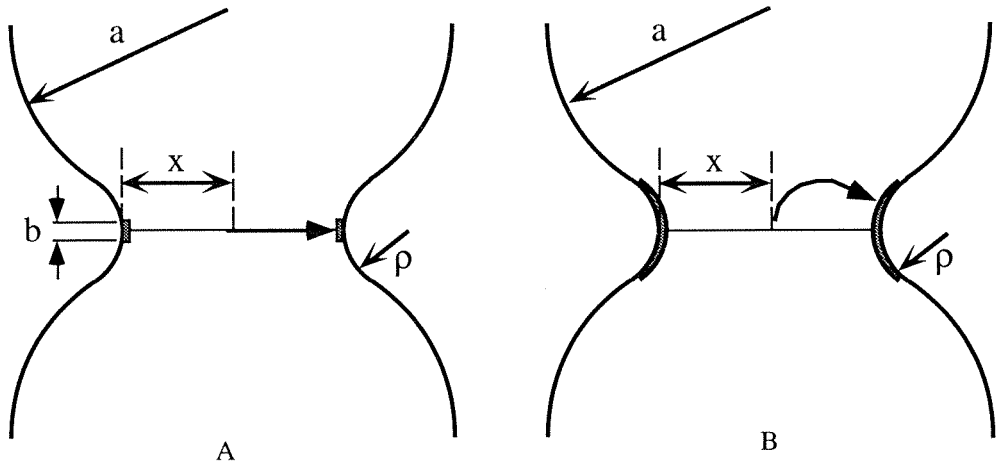

Figure 2.5: The diffusion pathways and flux areas for grain boundary diffusion (A) and Volume Diffusion-V (B).

In his derivations, Johnson expressed the flux in terms of stress gradients rather than concentration gradients. The stress distribution is a function of radial position along the grain boundary. Assuming that only volume and grain boundary diffusion are active, and that a quasi-steady-state exists, $\nabla^2\mu$ is a constant everywhere along the grain boundary, hence

$$\nabla^2\mu = \nabla^2\sigma = C. \tag{2.30}$$

In cylindrical coordinates, this can be written as

$$\frac{1}{r}\frac{\delta}{\delta r}(r\frac{\delta\sigma}{\delta r}) = C. \tag{2.31}$$

The boundary conditions are

$$\sigma = \gamma(\frac{\cos\alpha}{x} - \frac{1}{\rho}) \quad \text{at} \quad r = x_n, \tag{2.32}$$

$$\frac{\delta\sigma}{\delta r} = 0 \quad \text{at} \quad r = 0, \tag{2.33}$$

$$\int_0^{x_n} \sigma(r)\delta A = 2\pi \int_0^{x_n} \sigma(r) r dr = 2\pi x \gamma \cos\alpha, \tag{2.34}$$

where α is related to the grain boundary interface angle $\alpha = \pi/2 - \gamma/2$. The first equation describes the stress immediately below the neck surface. The expression in the parentheses in Eq. 2.32 describes the change in the surface curvature. The third equation is total energy of the grain boundary.

Integration of Eq. (2.31) gives

$$\sigma = \frac{1}{4}\mathcal{C}r^2 + \mathcal{B}\ln r + \mathcal{A}, \tag{2.35}$$

where the constants of integration are:

$$\mathcal{A} = \frac{\gamma(3\cos\alpha\rho + x_n)}{\rho x_n}, \tag{2.36}$$

$$\mathcal{B} = 0, \tag{2.37}$$

$$\mathcal{C} = -\frac{8\gamma(\cos\alpha\rho + x_n)}{{x_n}^3\rho}. \tag{2.38}$$

The diffusive flux becomes,

$$J = \frac{D}{kT}\frac{4\gamma(\cos\alpha\rho + x_n)}{\rho {x_n}^2}. \tag{2.39}$$

The area through which the material diffuses for the Volume Diffusion-V case is the area of the concave part of the neck as derived in Eq. (2.28). For grain boundary diffusion, this area is a cylinder around the neck, $A = 2\pi x_n b$,where b is the enhanced thickness for diffusion, usually assumed to be a few interatomic distances.

2.3.3 Evaporation and Condensation

The rate of sintering due to evaporation and condensation was briefly sketched by Kuczinski [3] in his initial work on sintering. The more detailed presentation developed by Kingery and Berg [4] is usually cited in the literature. Their flux equation is valid in the free molecular regime when the void around the neck region is small enough that little vapor remains in the gas phase. This mechanism is illustrated in Fig. 2.6.

The vapor pressure over the neck region is smaller than that over the bulk material due to its small negative radius of curvature, described by the Kelvin equation (Eq. 2.9),

$$\ln\frac{P}{P_0} = \frac{\gamma\Omega}{kT}\mathcal{K}. \tag{2.40}$$

Employing a similar approximation for pressure as in the previous case for concen-

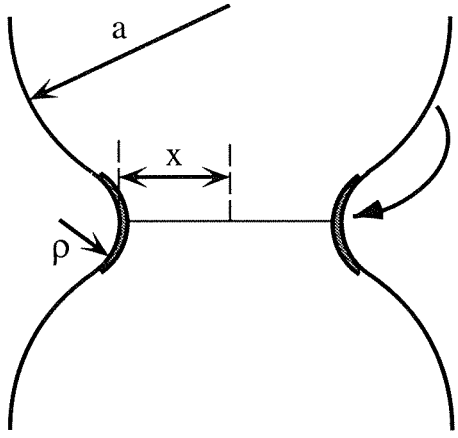

Figure 2.6: The diffusion pathways and flux areas for the evaporation & condensation mechanism.

tration, Eq. (2.8), gives

$$\frac{\Delta P}{P_0} = \frac{\gamma\Omega}{kT}\mathcal{K}, \tag{2.41}$$

or in terms of the gas constant, R,

$$\frac{\Delta P}{P_0} = \frac{\gamma M}{dRT}\mathcal{K}, \tag{2.42}$$

where d is the density of the material. For sufficiently small particles, the rate of material transfer can be approximated by the free molecular flux

$$J = \frac{n\bar{c}}{4}M \tag{2.43}$$

where $\bar{c}$ is the mean free speed of the species, $\bar{c} = \sqrt{\frac{8RT}{\pi M}}$, where M is the molecular weight, and n is the number concentration of vapor molecules. Assuming the ideal gas law and that the available volume for vapor is small enough that a steady-state

is rapidly established between evaporation and condensation, the molecular flux can be written as

$$\frac{\Delta n \bar{c}}{4} M = \Delta P \sqrt{\frac{M}{2\pi kT}}. \tag{2.44}$$

Substituting for ΔP as shown in Eq. (2.42) and dividing by the density d yields the volume flux onto the exterior surface of the neck (Eq. 2.28),

$$J = \frac{\gamma M P_0}{d^2 RT} \sqrt{\frac{M}{2\pi kT}} \mathcal{K}. \tag{2.45}$$

The limitations of the traditional evaporation and condensation model have previously been recognized by Rockland [6], but there appears to have been no attempt to refine the model. The implicit assumption that vapors emanating from the convex surfaces immediately find their way to the neck region may be reasonable for sintering of dense compacts, but may not be valid for the sintering of low density aerosol agglomerates. Implicit in this assumption is the presence of saturated vapor throughout the gas. If the gas is subsaturated, vapors may diffuse away from the surface of the particles and remain in the vapor phase until the gases cool. The vapors may then condense anywhere on the particle, or they may undergo homogeneous nucleation to produce new particles.

2.3.4 Viscous Flow

Frenkel developed the theory for the viscous sintering of spheres in 1945. [2] He treated the process as a slow deformation of amorphous or crystalline particles under

the influence of surface tension. This type of diffusion is different than the ordinary plastic flow of viscous bodies. It is now generally accepted that viscous flow cannot take place in crystalline materials [32], but can be an important mechanism in glasses and other amorphous materials.

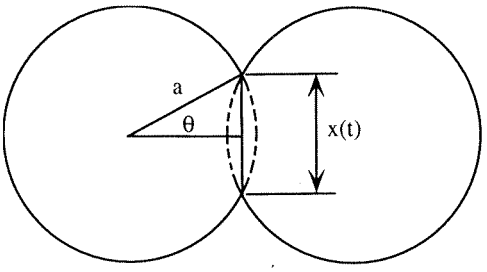

Figure 2.7: Geometry for the viscous flow derivation.

Frenkel modeled the coalescence of two liquid drops that initially contact with one another at a single point. The contact area at later times was described as a circle with radius $x(t)$ as illustrated in Fig. 2.7. Except for the contact, the drops maintain a spherical shape. The decrease in surface area can be written as

$$S_0 - S = 8\pi {a_0}^2 - 4\pi a^2(1 + cos\theta). \tag{2.46}$$

For small values of θ, Eq. (2.46) can be approximated by

$$S_0 - S = 2\pi {a_0}^2\theta^2. \tag{2.47}$$

The surface tension work during the initial stage of coalescence,

$$-\gamma\frac{dS}{dt} = 2\pi a_0\gamma\frac{d\theta^2}{dt} \tag{2.48}$$

must equal the rate of energy dissipation due to viscous flow. The flow can be described in terms of the decrease of the distance between the drop center and the contact surface, i.e.,

$$a(1-\cos\theta) \approx 1/2a\theta^2. \tag{2.49}$$

The velocity gradient with which all points approach the center of the system, α, can be written as the ratio of Eq. (2.49) to the radius a, i.e.

$$\alpha = \frac{d}{dt}\frac{\theta^2}{2}. \tag{2.50}$$

With these assumptions, the rate of viscous dissipation becomes

$$\frac{16}{3}\pi a^3 \eta \alpha^2. \tag{2.51}$$

Equating the viscous dissipation rate to the surface tension work gives

$$\frac{16}{3}\pi a^3 \eta \alpha = 4\pi a^2 \gamma \tag{2.52}$$

from which the velocity gradient can be written as

$$\alpha = \frac{3}{4\pi a}\frac{\gamma}{\eta}. \tag{2.53}$$

Hence,

$$\theta^2 = \frac{3}{2\pi}\frac{\gamma}{a\eta}t. \tag{2.54}$$

The area between the drops, $\pi y^2 \approx \pi a^2\theta^2$, is thus seen to increase at a uniform rate according to the formula

$$\pi x^2 = \frac{3}{2}\frac{a\gamma}{\eta}t. \tag{2.55}$$

2.3.5 Summary

The fluxes, J and the areas A through which the atoms migrate are summarized in Table 2.2. Although the flux fields and the length scales over which they are active used in these models involve a number of approximations, the flux expressions presented in Table 2.2 are reasonable approximations throughout the entire neck growth process.

Mechanism	Flux	Flux Area
Surface Diffusion	$J = -\frac{2\sigma\delta^3}{kT\rho}\mathcal{K}D_s$	$2\pi x\delta$
Volume Diffusion S	$J = -\frac{2\sigma\delta^3}{kT\rho}\mathcal{K}D_v$	$A = 2\int_0^{Zi} 2\pi Y_n(z)\sqrt{1+Y_n^2(z)}dz$
Volume Diffusion V	$J = \frac{D}{kT}\frac{4\gamma(\cos\alpha\rho+x)}{\rho x^2}$	$A = 2\int_0^{Zi} 2\pi Yn(z)\sqrt{1+Yn^2(z)}dz$
Grain Boundary Diffusion	$J = \frac{D}{kT}\frac{4\gamma(\cos\alpha\rho+x)}{\rho x^2}$	$2\pi xb$
Evaporation & Condensation	$J = \frac{\gamma M P_0}{d^2 RT}\sqrt{\frac{M}{2\pi kT}}\mathcal{K}$	$A = 2\int_0^{Zi} 2\pi Y_n(z)\sqrt{1+Y_n^2(z)}dz$
Viscous Flow	$\frac{x^2}{a} = \frac{3\gamma}{2\pi\eta}t$	

Table 2.2: Summary of individual sintering fluxes and areas.

2.4 Small Neck Approximations

To derive analytical expressions for neck growth, the traditional sintering models make geometric approximations for the various volumes and areas that are required to evaluate the fluxes. In particular, the neck size is commonly assumed to be small, leading to $\rho \ll a$. This small-neck approximation limits the classical predictions to $x/a \leq 0.3$ for the reasons discussed below.

Referring to Fig. 2.3, ρ can be written as

$$\rho = a(1 - \cos\theta) = \frac{x^2}{2a} \tag{2.56}$$

since $\theta \approx x/a$ in this limit. The area for diffusion and volume of the neck then become

$$A \approx \pi \frac{x^3}{a}, \tag{2.57}$$

and

$$V \approx \pi \frac{x^4}{2a}, \tag{2.58}$$

respectively. The sphere size is assumed to remain constant during sintering. These expressions are valid only for adhesion mechanisms, i.e., those mechanisms for which the particles centers do not approach each other. Substituting into Eq.(2.10), and approximating

$$\frac{dV}{dt} = \frac{dV}{dx}\frac{dx}{dt} \tag{2.59}$$

they reduce to the familiar x/a form in which they are usually reported. These

equations are listed in Table 2.3.

When the particle centers move towards one another as a result of material being removed from the grain boundary area via grain boundary diffusion or volume diffusion V, the early neck growth assumptions are not as clear. The geometry will change as a result of the linear shrinkage in the particle system. The fractional linear shrinkage of the two particles can be written as

$$y = \frac{\Delta l}{l_0}, \tag{2.60}$$

where l_0 is the diameter of the unsintered particle. Johnson and Clarke [36] solved the geometry equations for the neck radius x_n, neck surface radius ρ, and area A_n as a function of fractional linear shrinkage y and initial particle size a, and then fitted power laws to the solution. These approximations, which are valid for the first 3.5% of shrinkage, are:

$$\rho \approx 2.32 a y^{1.14} \tag{2.61}$$

$$x \approx 1.92 a y^{0.49} \tag{2.62}$$

$$A_n \approx 50.4 a^2 y^{1.54}. \tag{2.63}$$

Again, the sphere size is assumed to remain constant during sintering. The three equations were combined to give ρ and A_n as a function of particle and neck radius

$$\frac{\rho}{a} \approx .509 \left(\frac{x}{a}\right)^{2.32} \tag{2.64}$$

$$\frac{A_n}{a^2} \approx 6.48\left(\frac{x}{a}\right)^{3.14}. \tag{2.65}$$

Equations (2.64) and (2.65) were then substituted into the flux and area equations for grain boundary diffusion and volume diffusion-V, leading to the neck growth equations that are given in Table 2.3.

Mechanism	Sintering Rate Equation	n	m	Ref
Surface Diffusion	$\frac{x^7}{a^3} = \frac{56\gamma\delta^4}{kT} D_s t$	7	4	[3]
Volume Diffusion I	$\frac{x^5}{a^2} = \frac{40\gamma\Omega}{kT} D_v t$	5	3	[3]
Volume Diffusion II	$\frac{x^{4.12}}{a^{1.12}} = \frac{75\gamma\Omega}{kT} D_v t$	4.12	3	[4]
Grain Boundary Diffusion	$\frac{x^{6.22}}{a^{2.22}} = \frac{114\gamma\Omega}{kT} b D_b t$	6.22	4	[7]
Evaporation& Condensation	$\frac{x^3}{a} = \frac{2\pi M\gamma(M/2\pi RT)^{1/2} P_0 t}{d^2 RT}$	3	2	[7]
Viscous Flow	$\frac{x^2}{a} = \frac{3\gamma}{2\pi\eta} t$	1	2	[2]

Table 2.3: The standard neck growth rate equations from the literature.

2.5 Agglomerate Sintering Models

Particles evolving from high temperature aerosol processes often evolve as aggregates. Particles of this nature occur in several processes. Large flocs of agglomerated particles can be found in soots or in flame produced oxide products [37, 22, 38, 39, 40]. Metallic particles produced by condensation of vapors derived from solid precursors are aggregated [41, 42, 43]. These aggregates are generally ramified or "fractal-like" in structure and are made up of discernible sub-units, or primary particles. The size of the primary particles may be interpreted as the particle size at which the sintering

time began to exceed the coagulation time in the process. Prior to that time the particles coalesce completely, but subsequent collisions lead to partially fused spherical particles. This transition would, of course, be related to the time/temperature history of the process involved.

The equations that govern coagulation of spherical particles, i.e., when sintering is instantaneous, are well developed. This is not the case, however, when coagulation and coalescence take place on comparable time scales. The first attempt to describe the growth of agglomerates following both collision and coalescence contributions was presented by Ulrich [22, 37]. Ulrich modeled the viscous coalescence that occurs when a single primary particle contacts a number of other particles, α. He followed the decrease in the number of identifiable primary particles, N_T through the equation

$$-\frac{dN_T}{dt} = \frac{2N_T\alpha}{(\alpha+2)\tau}. \tag{2.66}$$

Each of these peripheral particles is assumed to coalesce with the central particle. Particles were assumed to sinter via viscous flow, using the characteristic time for complete fusion given by Frenkel [2]

$$\tau = \mu R_P/\sigma \tag{2.67}$$

where μ is the viscosity and σ is the surface tension.

Since Ulrich and coworkers were working with silica, their assumption that particles sinter primarily by viscous flow is valid. Their model does, however, assume that

the coalescence time does not depend upon particle coordination. Equation (2.67) was derived for a two-particle system, and the time required for coalescence of more that two particles can probably be assumed to increase as the particle coordination number, α, increases. In general, their model underpredicts the specific surface area for the coagulating and coalescing silane fume, suggesting that their model overpredicts coalescence rates. Some disagreement is to be expected since the characteristic time for viscous coalescence was estimated from an early stage sintering model.

More recently, Koch and Friedlander [23] developed a similar model in which they expressed the coalescence rate in terms of the surface area. In extending the sintering model beyond the early stage of neck growth, they cited a numerical analysis of neck growth by viscous flow of Hiram and Nir [17] which found that the neck radius approaches the final value exponentially. On this basis, they hypothesized that the surface area of the particle would undergo a first-order approximation for the decay, even for long times ($t \gg \tau_S$)

$$\left(\frac{ds}{dt}\right)_{coalescence} = -\frac{s - s_S}{\tau_S}. \tag{2.68}$$

Here, s_S is the surface area of the fully coalesced particle, and τ_S is the characteristic time for sintering. This expression is valid only at high temperatures when coalescence is fast, i.e. $\tau_{coal} \ll \tau_{coag}$. As shown in Koch and Friedlander, this model for viscous flow of a bisphere over-estimates the rate of coalescence initially and only approaches the Hiram and Nir result late in the sintering process.

From this beginning, approximate and detailed predictions of the size and surface

area distribution function have evolved [44, 25, 26, 28]. Although considerable effort has been invested in developing and solving representations of the coupled coagulation/coalescence problem, remarkably little attention has been given to the form of the sintering term itself. We anticipate the development of sintering models that more precisely follow the approach to complete coalescence by writing the rate equation for the surface area evolution in the form,

$$\left(\frac{ds}{dt}\right)_{coalescence} = f(s, T, t). \tag{2.69}$$

This formulation will allow the incorporation of more quantitative models of the neck geometry and multiple transport mechanisms.

2.6 Conclusions

Sintering plays an important role in the processing of materials at high temperatures. Traditionally associated with the processing of ceramics, sintering is the process by which a compact of loosely pressed particles adhere and grow together to form a dense, solid body. Recent studies of the formation of refractory particles from the gas phase have highlighted the importance of sintering in controlling the structures of particles produced in high temperature aerosol processes.

Historically, theoretical investigations of sintering have derived power-law relations for neck growth as a function of time under the action of a single transport mechanism. These growth expressions are based upon simplified geometries that

limit their applicability to a neck radius ratio below $x/a_i \approx 0.3$. Experimental observations of neck growth with time for a particular material were used to deduce the power-law exponents and to identify the predominant transport mechanism for the sintering of that material. This approach is experimentally confining since it is limited to initial neck formation. Furthermore, it can be misleading since all sintering mechanisms simultaneously contribute to neck growth to varying degrees. It is rare that one mechanism dominates to such an extent that others can be neglected.

This chapter has reviewed the different sintering mechanisms and derived flux expressions describing their individual contributions to neck growth. Using a simplified geometry and simplified models of the flux fields that exist within the particle, but relaxing the most serious assumptions of the classical sintering models, rate equations for neck growth that are valid for the entire neck growth process have been derived.

Applications of sintering theory to the coalescence of coagulating particles has been limited to simple models that include only one sintering mechanism. The use of the traditional, power-law descriptions of neck growth cannot, however, adequately describe the entire coalescence process. Rockland's results [6] clearly show that the use of a single value of the exponent n is misleading. The simple equations cannot reflect process sensitivity to changes in variables such as temperature and particle size. Since most aerosol processes encompass many changing characteristic sizes, times, and temperatures, this lack of sensitivity will prove most severe.

Chapter 3

Modeling the Sintering of the Bi-Sphere System

3.1 Introduction

Sintering is the movement of material, usually through diffusion, that results in the bonding and densification of a system of particles. The driving force for sintering is the excess surface energy of the system. Changes in local curvature create gradients in vapor pressure, stress, and chemical potential, causing a movement of material along these gradients. Necks form and grow between particles, substituting lower energy grain boundary area for surface area, and resulting in a decrease in system surface area. Knowledge and understanding of the sintering process is necessary to predict the rate of neck formation for different processing conditions.

Sintering can occur through a variety of material transport mechanisms. There are currently six individually recognized sintering mechanisms as shown in Fig. 3.1;

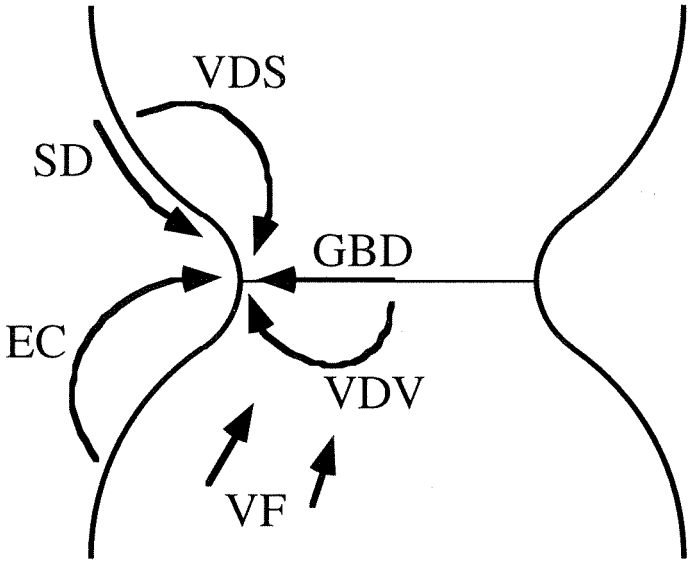

Figure 3.1: The individual sintering mechanisms and their transport paths.

surface diffusion, evaporation & condensation, grain boundary diffusion, two volume diffusion processes that use either the particle surface or the neck interior as a source of material, and viscous flow [2, 3, 4, 7]. Evaporation and condensation involves the movement of material through the vapor phase. Surface diffusion and volume diffusion-S move material from the surface of the particle to the neck via diffusion along the surface and volume of the particle respectively. Grain boundary diffusion and a second, distinct volume diffusion-V mechanism move material from the neck region between the particles to the neck surface along the grain boundary and through the volume of the particle, respectively. The viscous flow mechanism is a process of slow deformation under the influence of the surface tension where the coefficient of viscosity is related to the self-diffusion coefficient of the material, and is generally accepted to take place only in amorphous materials [32].

Identification of the dominant sintering mechanism is important not only to un-

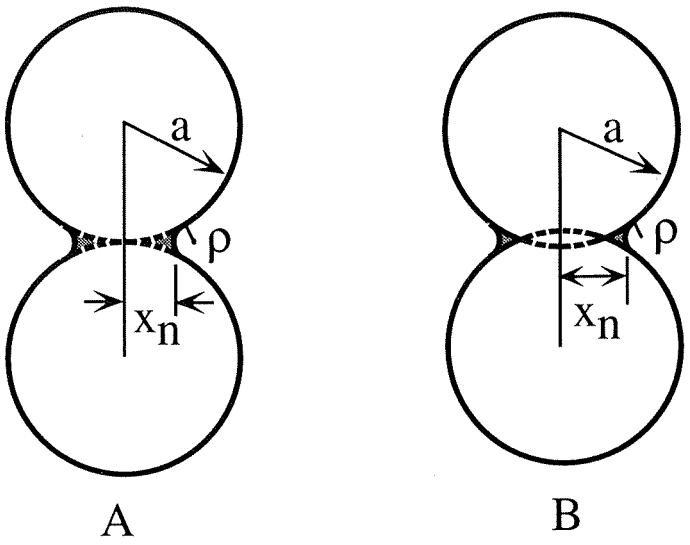

Figure 3.2: Two models for the initial stages of sintering of two spheres, one for adhesion (A) and one for densification (B).

derstand the kinetics, but also because different mechanisms effect the morphology of the particle system in different ways. This system is historically modelled using a two-sphere model as illustrated Fig. 3.2 [3]. Sintering may occur in two ways. Material may either simply fill in the areas between the spheres (Fig. 3.2A) or the centers of the spheres may approach one another (Fig. 3.2B). In the latter case, material diffuses from the region in and around the grain boundary causing the particles to move closer together and decreasing the total length of the particle system. The two mechanisms that use this source, grain boundary diffusion and volume diffusion-V, are called densification mechanisms because they result in the shrinkage of a powder compact. In the former case, material moves from the surface of the particle to the neck. The particle centers move no closer together. These mechanisms, evaporation & condensation, surface diffusion, volume diffusion-S, and viscous flow, are called the

adhesion mechanisms.

Traditionally, sintering by a single mechanism is described in terms of the increase in neck radius, x_n, with time,

$$\left(\frac{x_n}{a}\right)^n = \frac{B(T)}{a^m}t, \tag{3.1}$$

where a is the intial size of the contacting particle and the coefficient $B(T)$ is a function of the relevant material properties. The exponents m and n depend on the sintering mechanism and are presented in Table 3.1. Much of the early sintering work focussed on comparing results from model experiments involving spheres or wires to the neck growth equations. Based on the exponents determined from experimental measurements of neck growth versus time, conclusions were drawn as to the predominant sintering mechanism. The absolute neck growth times were rarely compared with model predictions, although, in many cases, a diffusion coefficient was estimated from the data and assumed mechanism. This method has given questionable results [6, 32]. One reason for observed discrepancies is that several sintering mechanisms generally work simultaneously. Although limited regimes during sintering may be fit with the simple sintering expressions, the attempt to describe the system with a single mechanism may give misleading results.

One of the primary problems in developing more precise sintering models lies with the complex geometry involved. Equation 3.1 is based upon simplified geometric assumptions about the particle system that limit their applicability past neck radius ratios of $x_n/a \approx 0.3$. The values of the neck radius, x_n, particle radius, a, and neck

Mechanism	n	m	Ref.
Surface Diffusion	7	4	[3]
Volume Diffusion I	5	3	[3]
Volume Diffusion II	4.12	3	[4]
Grain Boundary Diffusion	6.22	4	[7]
Evaporation & Condensation	3	2	[7]
Viscous Flow	2	1	[2]

Table 3.1: Values of the exponents m and n in the traditional sintering neck growth equations.

surface radius, ρ, all affect the magnitute of the gradients driving the flow of material. One of the most problematic assumptions is that the particle radius a does not change during sintering. As a result, the total system volume is not conserved. While this is not a bad assumption for very small neck sizes, it becomes potentially hazardous for predicting the time required for any substantial neck growth.

There have been some attempts to better model the evolving system geometry [8, 9, 10, 45, 11]. Other shapes have been assumed for the neck, including elliptical [46] and cartenoid [47]. The first successful attempt at a more accurate evaluation of the true morphology was due to Nichols and Mullins [8, 9]. They numerically simulated sintering due to surface diffusion, using a finite-difference approximation of an arbitrary surface of revolution to describe the neck region. They showed that the tangent circle model is not a good representation of the system. As can be seen by a sketch of their results superimposed on the circular assumption (Fig. 3.3), some

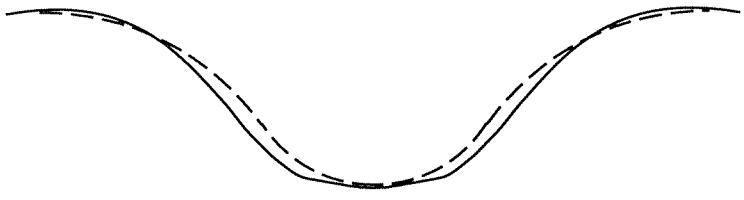

Figure 3.3: A sketch of the surface predicted by Nichols, the solid line, superimposed on a circular neck, represented by the dashed line.

undercutting of the particle surface occurs during sintering by surface diffusion alone.

Later investigators have performed similar numerical evaluations of the neck contour [10, 11]. Bross and Exner [10] employed a method similar to Nichols and Mullins for simultaneous surface and grain boundary diffusion. They also found significant undercutting, particularly in the early stages of sintering. In addition, they reported that the region influenced by material transport due to difference in curvature extends beyond that given by the circular model. Neither model included conservation of volume as an explicit constraint. More recently [11], simulations performed requiring volume conservation, but expressing the neck contour in a different way, give qualitative agreement with the previous work. However, they only examined the neck geometry and did not probe the time dependent flux problem.

We seek to achieve a better estimate of the time for neck growth that can in-

corporate all relevant sintering mechanisms and extend beyond the small neck limit. To that end, a model solving the geometry of the bisphere system in more detail is presented. This model will be coupled to the solution of the flux equations to give sintering rates. In addition, all sintering mechanisms will be solved simultaneously, allowing for the magnitude of an individual mechanism's contribution to be determined.

3.2 Description of Model Geometry

The formulation is based on sintering of two spherical particles that have some small initial neck formed between them, as shown in Fig. 3.4. The system is assumed to be cylindrically symmetric about the line joining the particle centers. This reduces the geometry solution to two dimensions. Both particles are assumed to be of the same size, meaning the particle system is also symmetrical about the grain boundary. The particles are assumed to retain their spherical shape during sintering. In addition, as the neck grows, it is assumed that a grain boundary forms between the two particles.

The particle system is described by six variables: x_n is the neck radius, a is the radius of the sphere, ρ is the radius of the neck surface, z_i is the distance at which the concave neck region contacts the convex particle surface, c is the location of the center of the particle, and α a measure of the grain boundary groove angle. The value of c gives an indirect measure as to the mechanisms at work. Its value will only decrease from its initial value if material is moved from between the particles by grain boundary or volume diffusion-V. This geometry, as defined, is valid only until $x_n = a$.

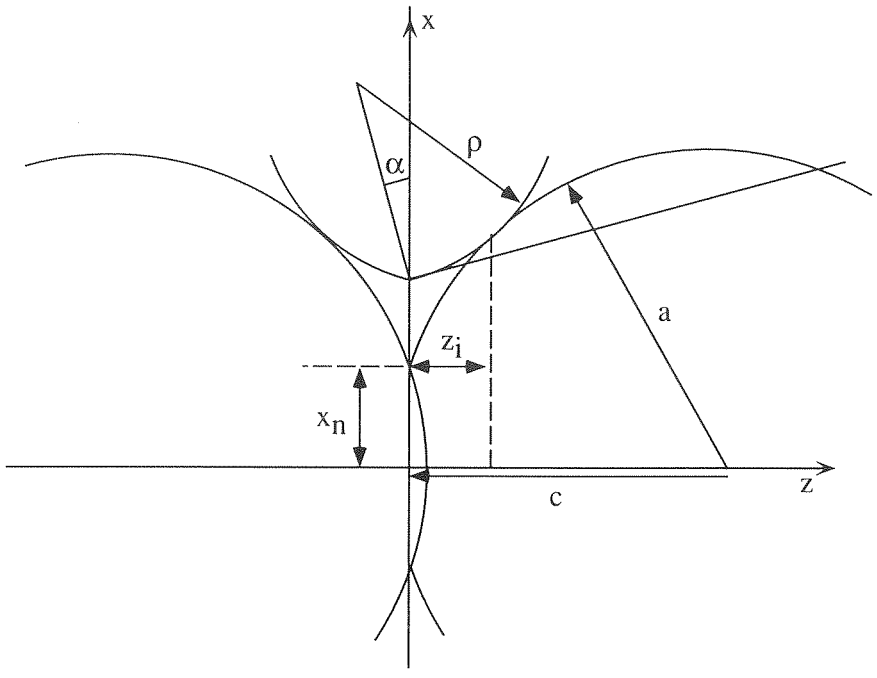

Figure 3.4: Proposed geometry used in the present model.

At this value, ρ approaches infinity as the neck surface becomes cylindrical, and the system assumes a "pill" shape. This is sufficient for modelling the neck growth, but cannot follow the system all the way to complete coalescence.

The surface of the neck and particle are assumed to be circular. Their descriptions are $Y_n(z)$ and $Y_s(z)$, respectively, and can be defined as follows;

$$Y_n(z) = x_n + \rho\cos\theta - \sqrt{\rho^2 - (z + \rho\cos\theta)^2} \tag{3.2}$$

$$Y_s(z) = \sqrt{a^2 - (z - c)^2}. \tag{3.3}$$

As was previously discussed, the circular description of the neck and particle surfaces

is not a true representation. The curvature values will differ from the more exact solution, and the effective length for material transfer will be smaller. While important, the errors introduced by the circular assumption, however, should be much smaller than the improvement in the overall system description. Following the geometry throughout the sintering process will greatly improve estimates for important process variables like the volume of the neck, the area through which material diffuses, and the difference in surface curvature.

The geometry of the bisphere system can be described with the following equations. The first requires that the volume of the system remains constant. This can be written numerically as,

$$\frac{4}{3}\pi {a_0}^3 = \frac{4}{3}\pi a^3 + V_n - \frac{1}{6}\pi(a-c)(3(a^2-c^2)+(a-c)^2), \tag{3.4}$$

where the volume of the neck, V_n, is that of the toroid

$$V_n = \int_0^{z_i} 2\pi {Y_n}^2(z)dz - \int_{Max(0,c-a)}^{z_i} 2\pi {Y_s}^2(z)dz. \tag{3.5}$$

The last term in Eq. (3.4) describes the overlap of the spheres due to removal of material from between the particles by the densification mechanisms. The two surfaces (neck and particle) must meet at z_i,

$$Y_s(z_i) = Y_n(z_i), \tag{3.6}$$

and must be tangent to each other at their interface,

$$\frac{\rho}{(z_i + \rho \sin\alpha)} = \frac{\rho + a}{(c + \rho \sin\alpha)}. \tag{3.7}$$

Lastly, the calculated V_n from the integration of the sintering flux equations must be equal to the geometric description,

$$V_{n,c} = V_{n,g}, \tag{3.8}$$

where $V_{n,g}$ is given by Eq. (3.5). The distance of the particle center from the plane of symmetry, c, becomes

$$c = 2a_0 \cos\left[\cos^{-1}\left(-\frac{1}{4}(2{a_0}^3 - \frac{3}{\pi}V_{dens})^2\right) + \frac{4}{3}\pi\right]. \tag{3.9}$$

The volume of material contributed by the densification mechanisms to the neck, V_{dens}, is determined by simultaneous integration of the flux equations for those mechansims.

These four equations, (3.4), (3.6), (3.7), and (3.8) are solved simultaneously for the variables x_n, ρ, z_i, and a. The equations were cast in dimensionless form by dividing by the initial particle radius a_0, and solved using a multi-dimensional non-linear equation package based on a modification of the Powell hybrid method [48]. The dimensionless forms of the equations are listed below, where $\hat{x}_n = x/a_0$, $\hat{\rho} = \rho/a_0$, $\hat{z}_i = z_i/a_0$, $\hat{a} = a/a_0$, and $\hat{c} = c/a_0$:

$$
\begin{aligned}
f_1 &= \frac{4}{3}\pi(\hat{a}^3 - 1^3) + \pi\hat{z}_i(\hat{x}_n^2 + 2\hat{\rho}^2\cos^2\alpha + 2\hat{x}_n\hat{\rho}\cos\alpha) + \pi\hat{z}_i^2\hat{\rho}\sin\alpha - \\
&\quad \pi(\hat{x}_n + \hat{\rho}\cos\alpha)((\hat{z}_i + \hat{\rho}\sin\alpha)\sqrt{\hat{\rho}^2(1-\sin^2\alpha) - 2\hat{z}_i\hat{\rho}\sin\alpha - \hat{z}_i^2} \\
&\quad + \hat{\rho}^2\sin^{-1}(\frac{\hat{z}_i + \hat{\rho}\sin\alpha}{\hat{\rho}}) - \hat{\rho}^2\cos\alpha\sin\alpha - \alpha\hat{\rho}^2) - \\
&\quad \pi(\hat{z}_i(\hat{a}^2 - \hat{c}^2) + \hat{z}_i^2\hat{c}) - \pi(\frac{2}{3}\hat{a}^3 + \frac{1}{3}\hat{c}^3 - \hat{a}^2\hat{c}) \qquad (3.10)
\end{aligned}
$$

$$
f_2 = \hat{x}_n + \hat{\rho}\cos\alpha - \sqrt{\hat{\rho}^2 - (\hat{z}_i + \hat{\rho}\sin\alpha)^2} - \sqrt{\hat{a}^2 - (\hat{z}_i - \hat{c})^2} \qquad (3.11)
$$

$$
f_3 = \hat{\rho}\hat{c} - \hat{\rho}\hat{z}_i - \hat{a}\hat{z}_i - \hat{a}\hat{\rho}\sin\alpha \qquad (3.12)
$$

$$
\begin{aligned}
f_4 &= \pi\hat{z}_i(\hat{x}_n^2 + 2\hat{\rho}^2\cos^2\alpha + 2\hat{x}_n\hat{\rho}\cos\alpha) + \pi\hat{z}_i^2\hat{\rho}\sin\alpha - \\
&\quad \pi(\hat{x}_n + \hat{\rho}\cos\alpha)((\hat{z}_i + \hat{\rho}\sin\alpha)\sqrt{\hat{\rho}^2(1-\sin^2\alpha) - 2\hat{z}_i\hat{\rho}\sin\alpha - \hat{z}_i^2} \\
&\quad + \hat{\rho}^2\sin^{-1}(\frac{\hat{z}_i + \hat{\rho}\sin\alpha}{\hat{\rho}}) - \hat{\rho}^2\cos\alpha\sin\alpha - \alpha\hat{\rho}^2) - \\
&\quad \pi((\hat{a}^2 - \hat{c}^2)(\hat{z}_i - Max(0, \hat{c} - \hat{a}) + \hat{c}(\hat{z}_i^2 - Max(0, \hat{c} - \hat{a})^2) + \\
&\quad \frac{1}{2}Max(0, \hat{c} - \hat{a})^3)) - V_{n,c} \qquad (3.13)
\end{aligned}
$$

3.2.1 Comparison of Proposed Geometry to Standard Geometrical Assumptions

As noted above, geometrical assumptions place severe restrictions on the range of applicability of the traditional sintering models. In the "small neck" limit, $\rho \ll a$, the radius of curvature for the neck becomes, approximately [3]

$$
\rho \approx \frac{x_n^2}{2a}. \qquad (3.14)
$$

The difference in surface curvature, $\mathcal{K}$, reduces to

$$\mathcal{K} = \frac{1}{\rho} - \frac{1}{x_n} + \frac{2}{a} \approx \frac{1}{\rho}. \tag{3.15}$$

The neck volume becomes,

$$V_n \approx \pi \frac{x_n^4}{2a} \tag{3.16}$$

and the area of the concave neck region is,

$$A_n \approx \pi \frac{x_n^3}{a}. \tag{3.17}$$

When the particle centers move towards one another as a result of material being removed from the grain boundary area via grain boundary diffusion or volume diffusion-V, the early neck growth assumptions are not as clear. The geometry will change as a result of the linear shrinkage in the particle system. The fractional linear shrinkage can be written as

$$y = \frac{a - c}{2a_0}. \tag{3.18}$$

Johnson and Clarke [36] solved the geometry equations for the neck radius x_n, neck surface radius ρ, and area as a function of linear fractional shrinkage y and initial particle size a, and then fitted power laws to the solution. These approximations, which are valid for the first 3.5% of shrinkage, are:

$$\rho \approx 2.32 a y^{1.14} \tag{3.19}$$

$$x \approx 1.92ay^{0.49} \tag{3.20}$$

$$A_n \approx 50.4a^2y^{1.54}. \tag{3.21}$$

The sphere size is assumed to remain constant during sintering. The three equations were combined to give ρ and A_n as a function of particle radius and neck radius

$$\frac{\rho}{a} \approx .509\left(\frac{x}{a}\right)^{2.32} \tag{3.22}$$

$$\frac{A_n}{a^2} \approx 6.48\left(\frac{x}{a}\right)^{3.14}. \tag{3.23}$$

Note that quations (3.22) and (3.23) differ only slightly from the assumptions for no penetration as given in Eq. (3.14) and Eq. (3.17).

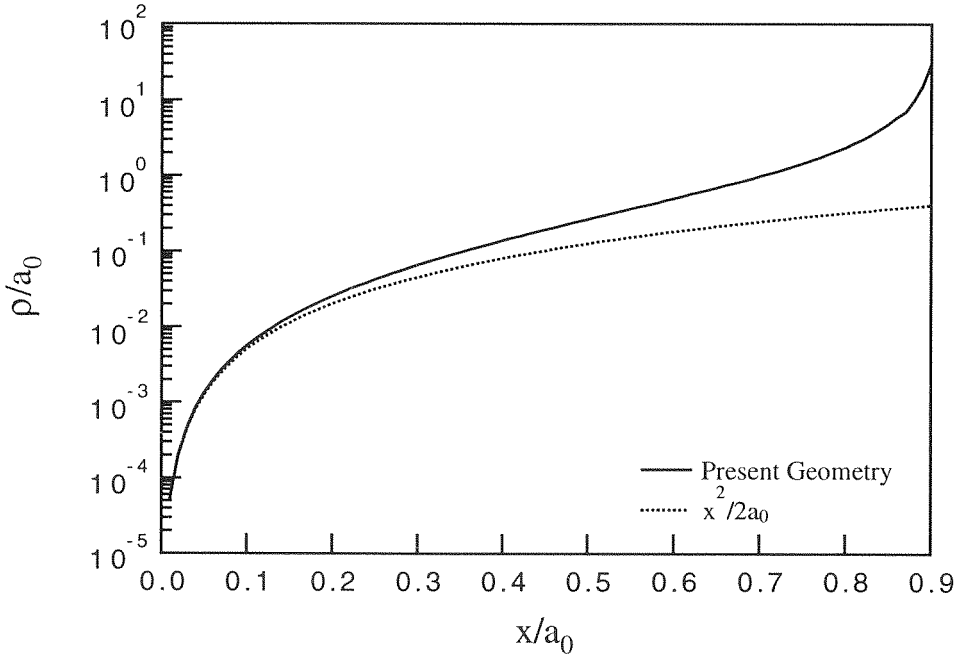

Figure 3.5: Graph of the difference in the small neck approximation for $\hat{\rho}$ and the results of the present geometry.

Figures 3.5 and 3.6 compare the values of $\hat{\rho}$ and $\hat{A}_n$ calculated using the model

geometry to the approximations given in Eqs. (3.14) and (3.17). For small x_n, the two models are in close agreement, but at $x_n = 0.3$, the commonly stated limit of the early stage sintering, the values from the assumptions for $\hat{\rho}$ and $\hat{A}_n$ underestimate those predicted by the model by 45% and 85%, respectively. These errors continue to increase with increasing x_n, and will affect values upon which the sintering flux is determined and thus cause large errors in the sintering rate as estimated using the early stage sintering model. The more realistic geometric model employed in this study should significantly improve the predictions of the sintering time.

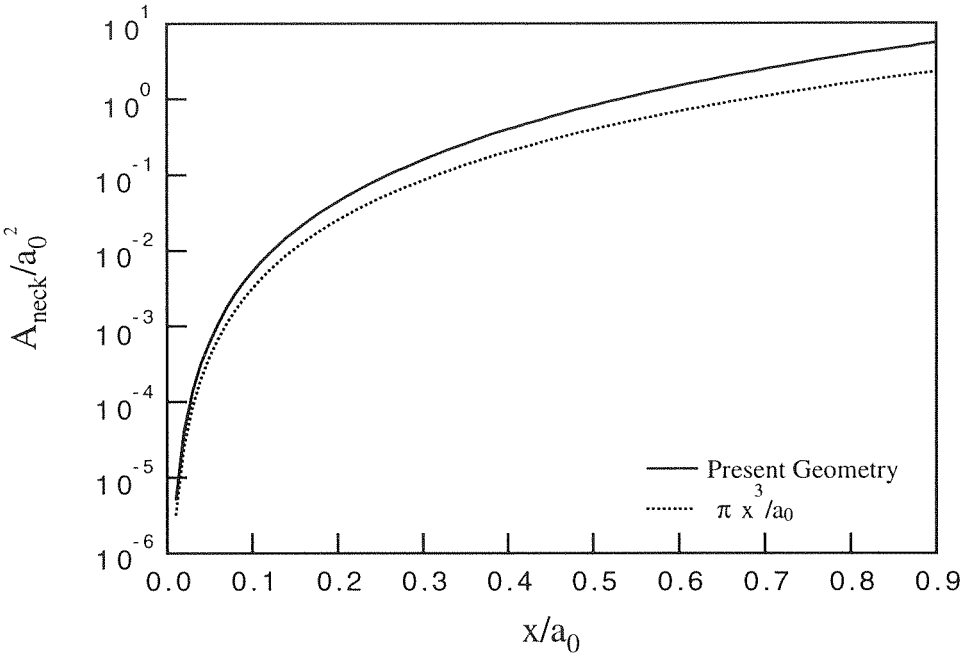

Figure 3.6: Graph of the difference in the small neck approximation for $\hat{A}_{neck}$ and the results of the present geometry.

3.3 Sintering Rate Equations

The total flux to the neck is the sum of the contributions of the individual mechanisms

$$\left(\frac{dV}{dt}\right)_{total} = \left(\frac{dV}{dt}\right)_{SD} + \left(\frac{dV}{dt}\right)_{VDS} + \left(\frac{dV}{dt}\right)_{EC} + \left(\frac{dV}{dt}\right)_{GBD} + \left(\frac{dV}{dt}\right)_{VDV} + \left(\frac{dV}{dt}\right)_{VF}. \tag{3.24}$$

The contributions of densification mechanisms to neck growth can be evaluated concurrently with the total neck contribution

$$\left(\frac{dV}{dt}\right)_{densf} = \left(\frac{dV}{dt}\right)_{GBD} + \left(\frac{dV}{dt}\right)_{VDV}. \tag{3.25}$$

The neck volume change due to densification is needed to determine how much the spheres have "penetrated" one another, as measured by the center separation, $2c$. The contribution of the various sintering mechanisms are also calculated individually to probe their importance in the sintering process. A multiplier is used to exclude mechanisms from the integration, e.g. excluding viscous flow when performing calculations for crystalline materials. A summary of the rate equations for the individual mechanisms is given in Table 3.2.

The rate equations were nondimensionalized before solving. The various length scales were nondimensionalized by dividing by the original particle radius, a_0. The coefficient of volume diffusion was used to nondimensionalize time,

$$\tau = \frac{D_v t}{{a_0}^2}. \tag{3.26}$$

This coefficient was chosen because it is generally better known than the other diffusivities. For those cases where sintering is volume diffusion controlled, the dimensionless time required for neck growth should be O(1). However, the dimensionless time required for sintering under surface or grain boundary diffusion control may be significantly larger or smaller since each sintering mechanisms has its own characteristic time.

Mechanism	Rate
Surface Diffusion	$-\frac{4\pi x_n \sigma \delta^4}{kT\rho}\left(\frac{1}{\rho}-\frac{1}{x_n}+\frac{2}{a}\right)D_s$
Volume Diffusion I	$-\frac{2\sigma \delta^3}{kT\rho}\left(\frac{1}{\rho}-\frac{1}{x_n}+\frac{2}{a}\right)D_v A_n$
Volume Diffusion II	$\frac{4\gamma(\cos\alpha\rho+x_n)}{kT\rho {x_n}^2}D_v A_{neck}$
Grain Boundary Diffusion	$\frac{8\pi x_n \gamma(\cos\alpha\rho+x_n)}{kT\rho {x_n}^2}bD_b$
Evaporation & Condensation	$\frac{\gamma M P_0}{d^2 RT}\sqrt{\frac{M}{2\pi kT}}\left(\frac{1}{\rho}-\frac{1}{x_n}+\frac{2}{a}\right)A_n$
Viscous Flow	$\frac{{x_n}^2}{a}=\frac{3\gamma}{2\pi\eta}t$

Table 3.2: Sintering rates, $\frac{dV}{dt}$, for individual mechanisms.

3.4 Computational Method

The rate equations for the neck volume and the densification volume were integrated numerically using a Burlish-Stoer integration scheme [49]. At each time step, the simultaneous nonlinear equations were solved using a modified Powell-Hybrid algorithm [48]. An initial neck size, x_n, and sintering time interval are needed to begin solution of the model. The initial neck size is used with the three remaining geometry

equations (as described above) to give initial values for all geometric parameters. The geometric values necesary to solve the individual flux derivatives are calculated simultaneously with the derivatives as a sort of constituative relationship. The non-linear equation solver is "seeded" with the solution of the geometry from the previous time step and the current solution of the neck volume from the integration.

As the integration progresses, the time step used by the program increases. This is logical, as the nature of the sintering process is such that the time scales increase as the process progresses. However, care must be taken not to increase the time step at too great a rate. If the program tries too great a step in time, the corresponding increase in neck volume will be too great for correct solution of the geometry. If the non-linear equation solver is seeded too far away from its solution, it often converges to a non-physical answer.

In addition, the geometry is unstable at small neck sizes. Currently, for values of the neck radius less that about 0.12 ($x_n < 0.12$), the solver will not converge on an answer. The nature of the jacobian often sends the solution in this region to an area where the variable z_i is greater that ρ, leading to an error in the term $sin^{-1}(\rho/z_i)$, and a concurrent failure to converge. In this early neck growth region, the variables z_i and ρ are also changing over several orders of magnitude. The equations are especially sensitive to ρ because it occurs in many terms to the third power. Convergence to a physical answer is possible in this early neck growth region, but the initial guess at the answer must be carefully adjusted. The program cannot currently make these fine adjustments as it integrates.

3.5 Results and Discussion

We have selected silicon and copper as materials for study using the present model. Silicon was selected because we have an experimental interest in the material. Copper was selected because there is a wealth of studies, both experimental and theoretical, using this material in the literature. The property data used are summarized in Table 3.3.

Figures 3.7 and 3.8 show example output from the model for the neck growth of silicon. The results indicate that the time for the same relative amount of neck growth decreases with decreasing particle size and increasing temperature. The model can also compute the relative amount that each individual sintering mechanism contributes to the volume of the neck, as seen in Fig. 3.9 for a 50 μm silicon particle sintered at 1473 K. Surface diffusion totally dominates the sintering of silicon under these conditions, with other mechanisms being negligible.

Calculations can be performed with the present model using any combination of sintering mechanisms. Results of calculations using only one mechanism can be directly compared to the traditional small neck equations of the form of Eq. (3.1). Model results from calculations performed for surface diffusion only, shown in Fig. 3.10, show good aggreement with the traditional model at small neck sizes, but deviate as x_n/a_0 becomes greater than 0.3 as expected.

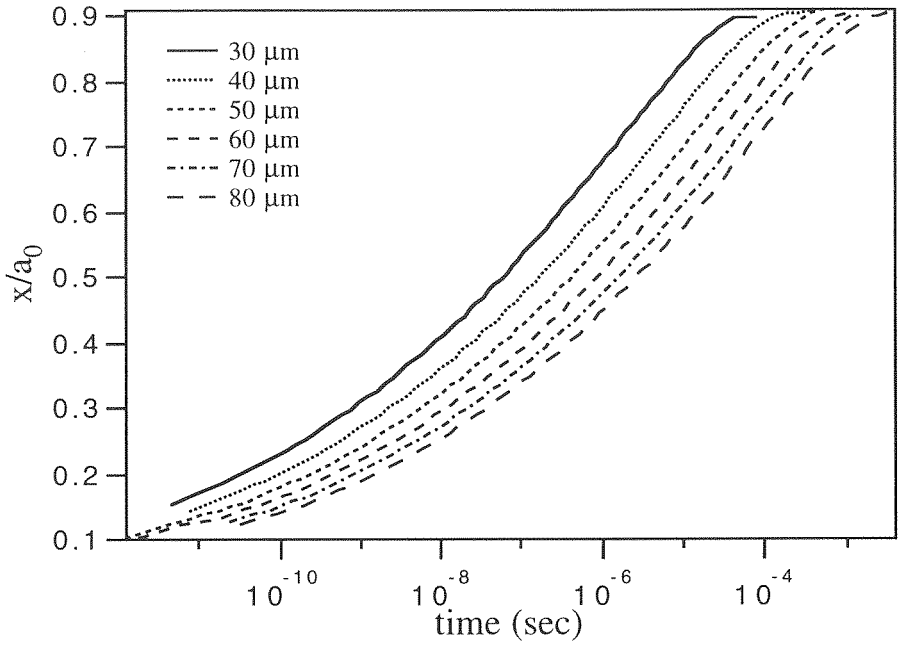

Figure 3.7: Results from the present model for silicon spheres of various sizes sintered at 1273K.

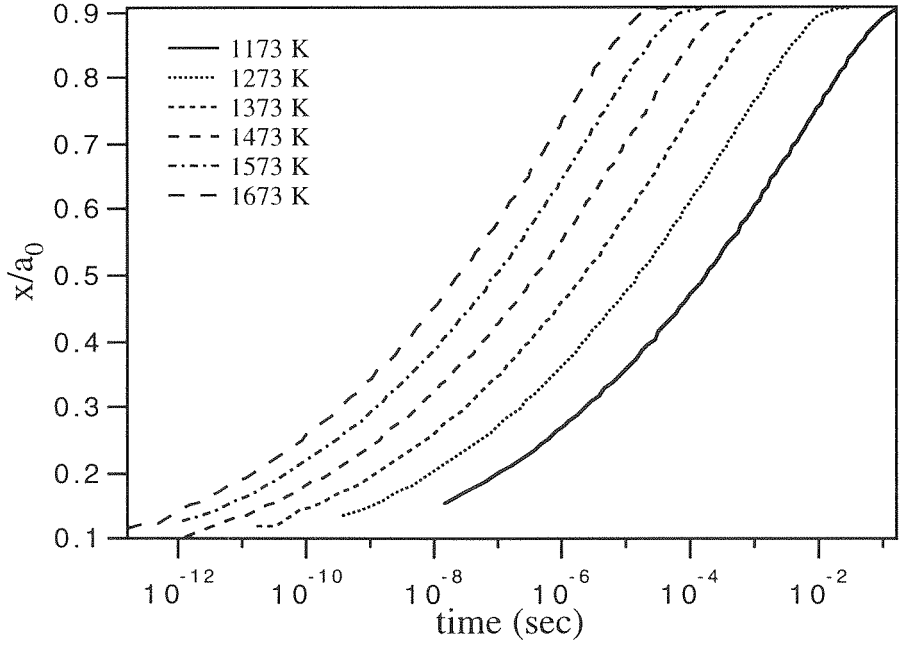

Figure 3.8: Results from the present model for silicon spheres, 50 nm in radius, sintered at various temperatures.

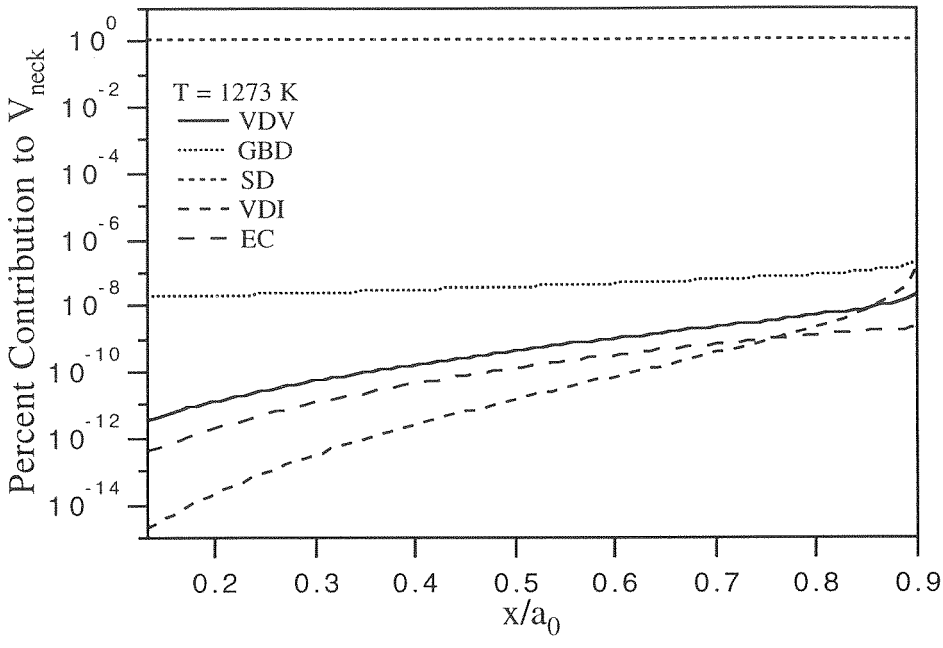

Figure 3.9: The relative importance of individual mechanisms during the sintering of 50 nm silicon spheres at 1273K.

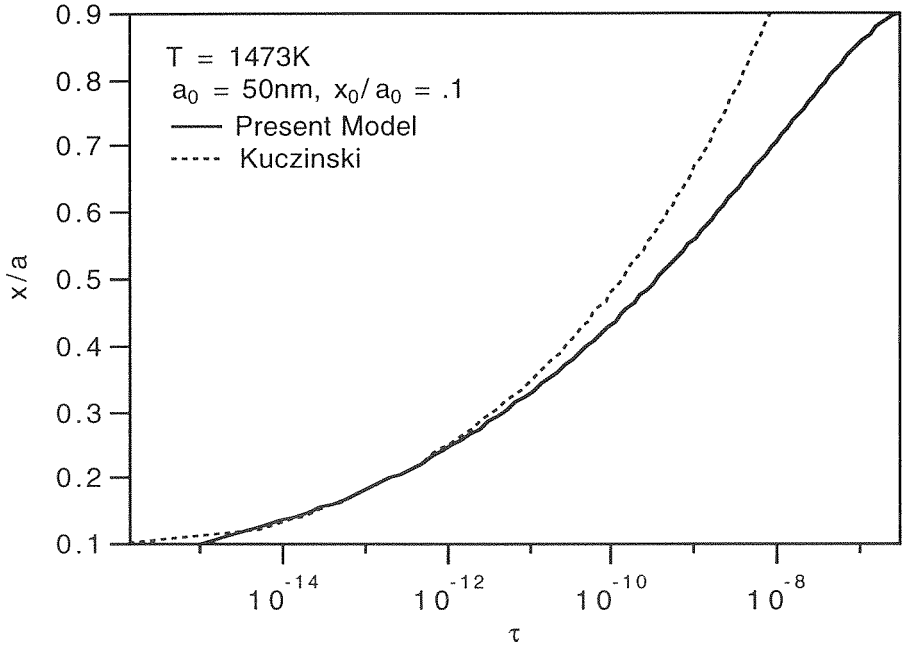

Figure 3.10: Comparison between the standard small neck model for surface diffusion to results from the present model. Results shown are for 50 nm silicon spheres sintered at 1473 K.

3.5.1 Comparison to Other Models

While few sintering models encompassing both geometry and the time dependent flux equations exist, it is worthwhile to compare to those that are available. Model results calculated with surface diffusion as the only active mechanism can be directly compared with results from Nichols' work [9]. Recall that Nichols simulated sintering due to surface diffusion, using a finite-difference approximation of an arbitraty surface of revolution to describe the neck region. The surface of the neck was allowed to change morphology as it sintered. Comparison of the results from the two models for different temperatures are shown in Fig. 3.11. Nichols reported his output in tabular form for a few neck sizes which are indicated by markers in the comparison. Similar comparisons for different sizes sintered at the same temperature are shown in Fig. 3.12. All results shown are for silicon, and Nichols output has been converted to the non-dimensional as defined in Eq. (3.26). Nichols used an initial non-dimensional neck radius, x_n/a_0 of 0.05, while we used 0.1.

In general, the difference between the two models remains constant for different temperatures and particle sizes. The present model predicts faster sintering times for smaller neck sizes. Two possible explanations exist. Firstly, the circular assumption for our surface geometries would result in a smaller mean curvature difference than that due to the undercutting predicted by Nichols, resulting in a larger net flux. The difference in the initial conditions between the two models is also of importance. Due to previously discussed limitations in the solution of the system geometry, the present model starts further on in the sintering process (a larger neck radius), and would not

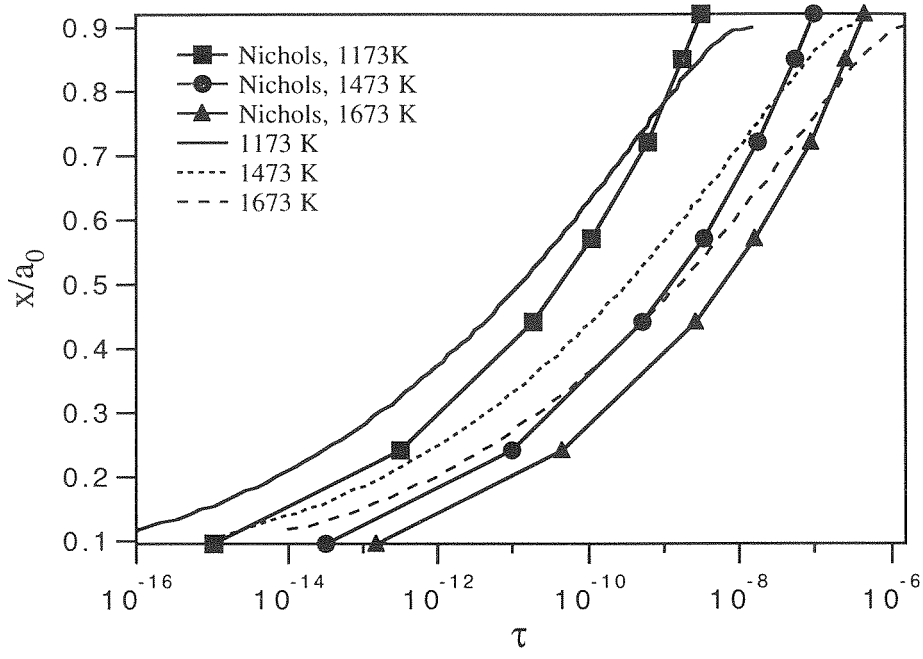

Figure 3.11: Comparison between the results from the present model and Nichols. Lines with markers are from Nichols. All results are for 50 nm silicon spheres.

require as much time to reach a given neck radius. At approximately 0.78, the curves cross. As the two-sphere system approaches the "pill" shape, the assumption that the individual spheres maintain their shape breaks down.

3.5.2 Comparison to Literature Data

During the first decades of the development of sintering theory, many investigators attempted to measure neck growth rates. Experiments performed usually involved sintering of carefully alligned, micron sized spheres or wires that were then sectioned for neck size measurements. Based on the exponents determined from the measurements of neck growth versus sintering time, conclusions were drawn as to the predominant sintering mechanism. Although this method of analysis is now considered to be an

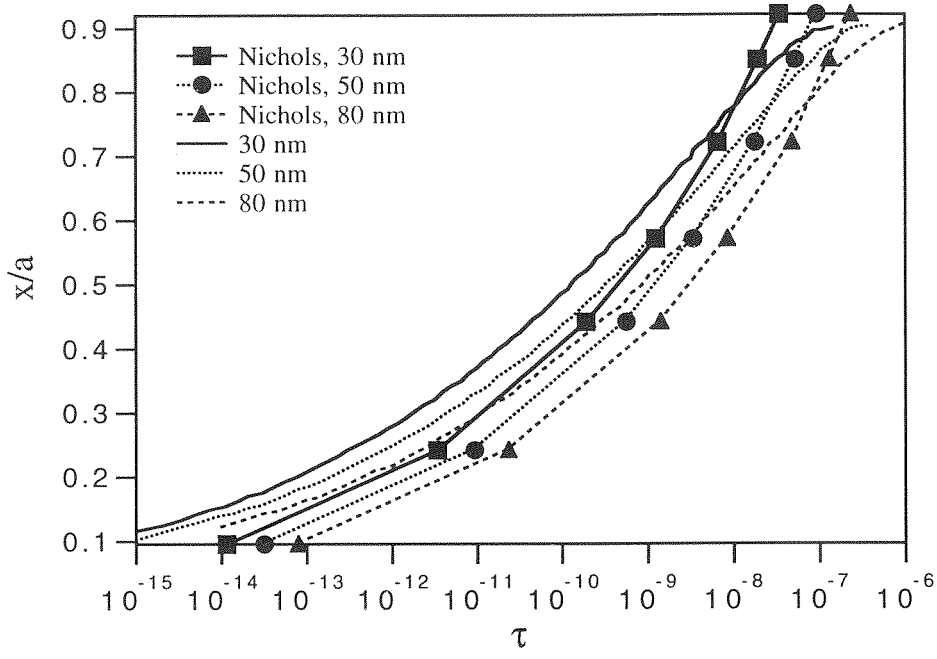

Figure 3.12: Comparison between the results from the present model and Nichols. Lines with markers are from Nichols. All results are for silicon spheres sintered at 1473 K.

unreliable procedure, the published neck growth measurements can be compared to predicted growth from the present model.

Kingery and Berg performed sintering experiments on copper spheres [4]. They measured neck growth for spheres of mean size 50 μm in radius sintered at temperatures between 1223 K and 1323 K. Based upon a fitted value of 5.0-5.5 for the exponent in the small neck growth equation (Eq. 3.1), they concluded that sintering proceeded by a diffusive mechanism. Observation of shrinkage in the center-center distance of the spheres led them to believe that volume diffusion was the predominant mechanism for sintering in copper.

Figure 3.13 shows how the present model compares with the data reported by Kingery and Berg. The results shown are for copper spheres, 50.5 μm in radius, sin-

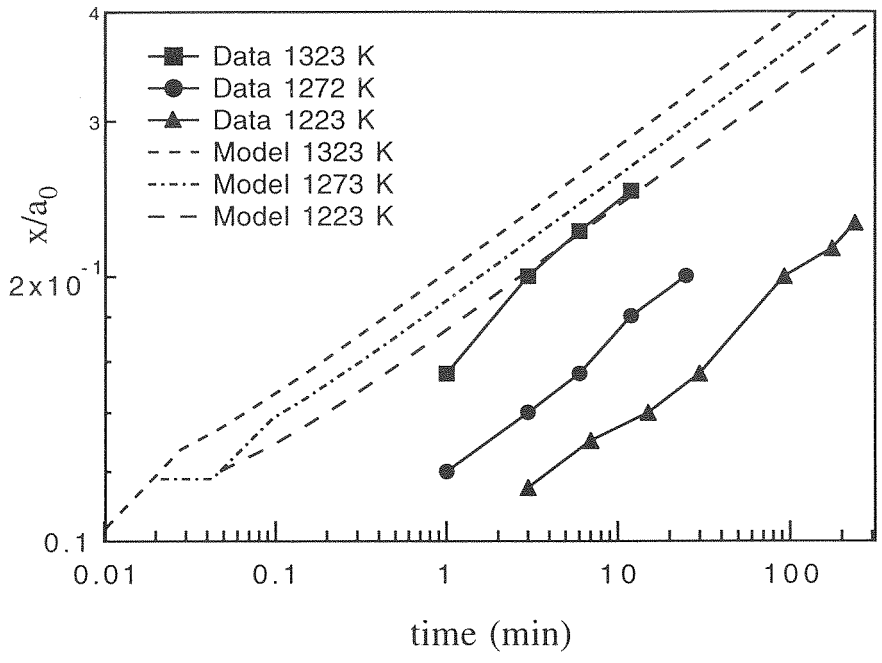

Figure 3.13: Comparison between the resuls from the present model and data from Kingery and Berg. Results shown are for copper spheres, 50.5 μm in radius.

tered at three temperatures. The model underpredicts the time required for sintering. The difference between the experimental results and predictions becomes greater as the sintering temperature decreases. However, the slopes of the growth curves and the experimental results do seem similar.

The relative importance of each mechanism during sintering are shown in Figs. 3.14 through 3.17 for several temperatures and an initial particle radius of 50 μm. At the lower temperature, both grain boundary diffusion and surface diffusion are of about equal importance, with volume diffusion increasing in importance as the neck grows. As the sintering temperature increases, surface diffusion becomes more important at the expense of grain boundary diffusion.

An explanation for the underprediction of the model lies in the previously dis-

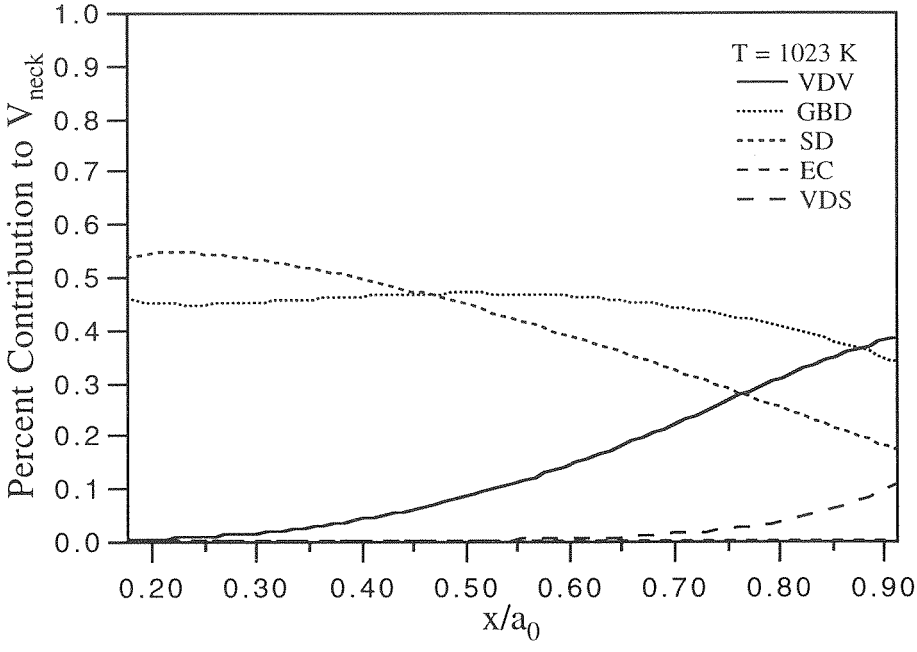

Figure 3.14: The relative importance of individual sintering mechanisms for the sintering of 50.5 μm copper spheres at 1023 K as a function of neck size.

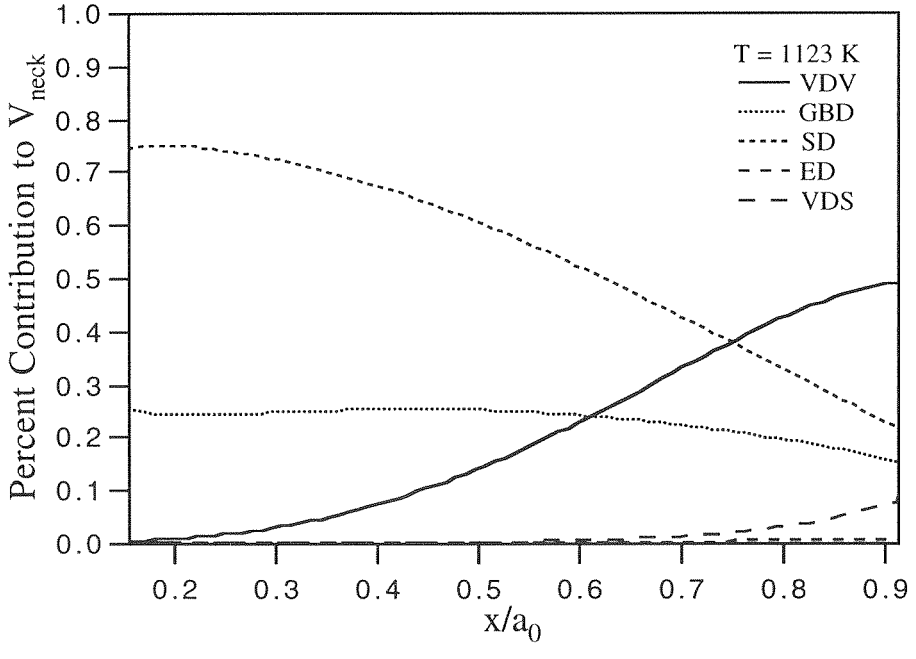

Figure 3.15: The relative importance of individual sintering mechanisms for the sintering of 50.5 μm copper spheres at 1123 K as a function of neck size.

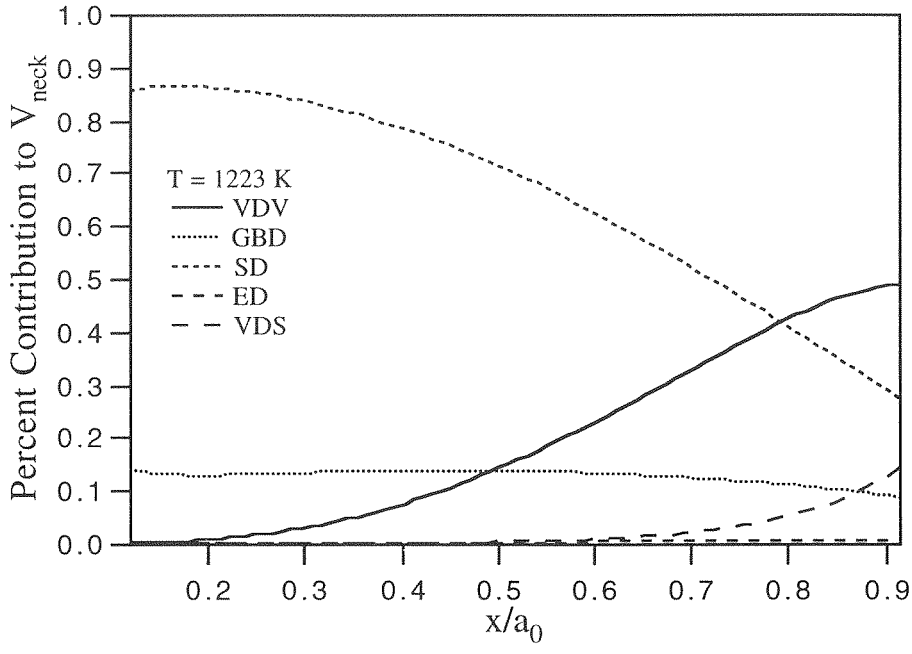

Figure 3.16: The relative importance of individual sintering mechanisms for the sintering of 50.5 μm copper spheres at 1223 K as a function of neck size.

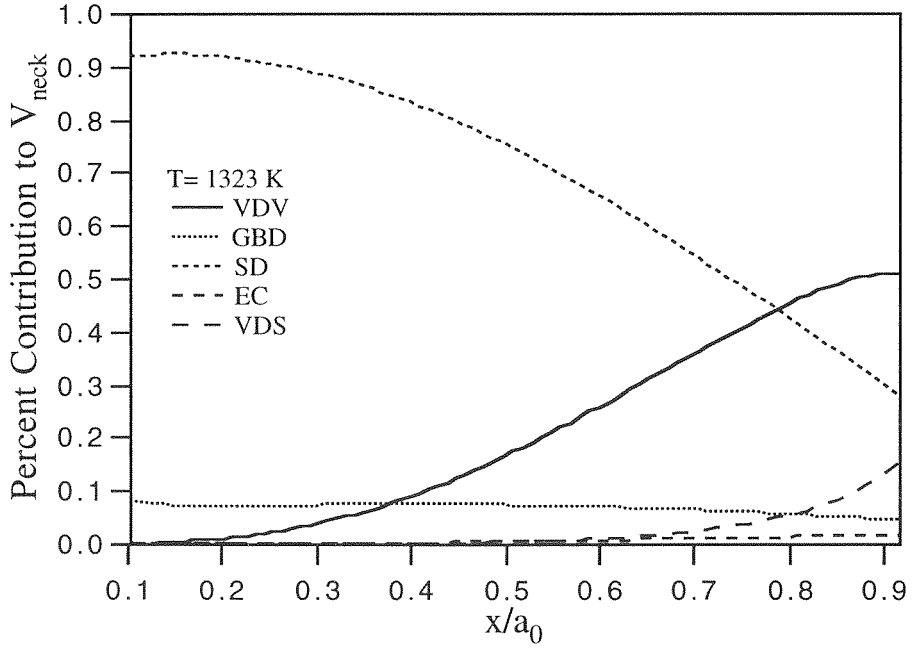

Figure 3.17: The relative importance of individual sintering mechanisms for the sintering of 50.5 μm copper spheres at 1323 K as a function of neck size.

cussed limitations of the circular surfaces assumption. In early neck growth, the assumption leads to a larger curvature difference and thus larger material fluxes. In addition, the present model starts with an initial neck of x_n/a_0 of 0.1, while the experiments had a negligible initial neck. In a sense, the model has a "head start" on the experiment, and will not require as much time to reach a comparable neck size.

The difference in behavior with temperature is more difficult to explain, but a few possibilities exist. The most obvious is that the model results were calculated isothermally, but experimentally the particles will require some time to reach thermal equilibrium with the surrounding gas. Secondly, as the temperature decreases, grain boundary diffusion becomes more important, as discussed above. However, values of the grain boundary diffusion activation energies and pre-exponential factors are often inferred from other materials or given as a percentage of the volume diffusion data. In this case, the grain boundary diffusion properties for copper were inferred by scaling data from material of the same structure and of comparable melting points [46]. Errors in the property data will affect the times predicted by the model.

Wilson and Shewmon have also reported data for sintered copper spheres [53]. They measured neck growth for spheres of sizes ranging from 50 to 155 μm in radius at 1223 K and 1293 K. Based on kinetic studies of neck growth, they determined that surface diffusion predominates sintering, with grain boundary diffusion becoming increasingly more important as the temperature decreased. The results of the present model clearly bear this conclusion out. A comparison of the present model's neck growth results to their data at 1223K shown in Fig. 3.18 shows the same un-

derprediction of the time required for neck growth as seen in the comparison to the Kingery and Berg data. The amount of underprediction does remain constant for different particle sizes. Figure 3.19 show a comparison to the results for two particle sizes at two different temperatures. In contrast with Kingery and Berg, the difference between the model and experimental results does not increase with temperature.

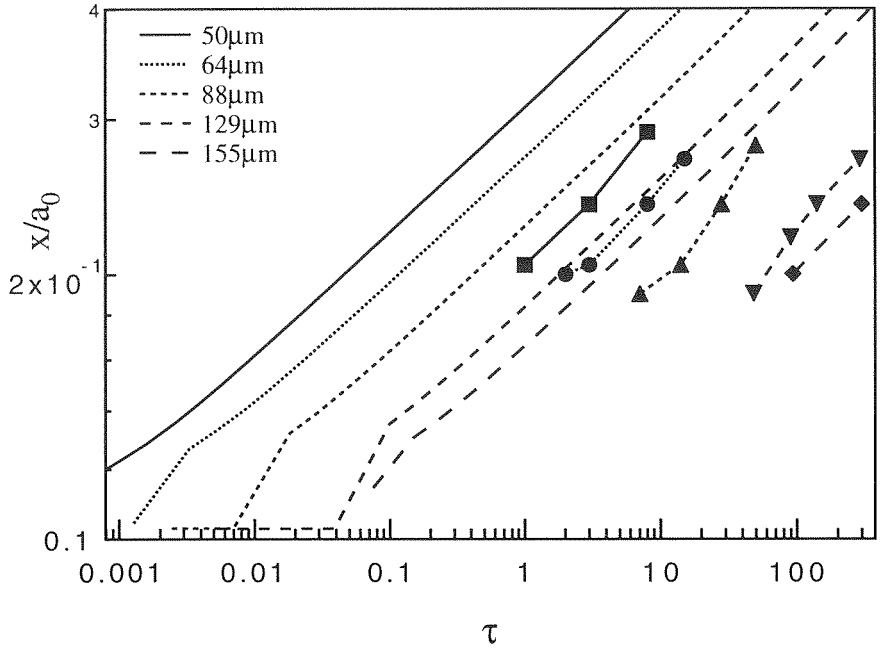

Figure 3.18: A comparison of experimental data from Wilson and Shewmon to model results. Results shown for copper spheres of various sizes sintered at 1223 K.

3.6 Conclusions

A model has been developed that calculates sintering times for the two sphere system. To predict neck growth as a function of time, the model solves for the evolving system geometry as the particles sinter, continuously conserving particle volume. This allows results to be calculated beyond the small neck limit of the traditional sintering models.

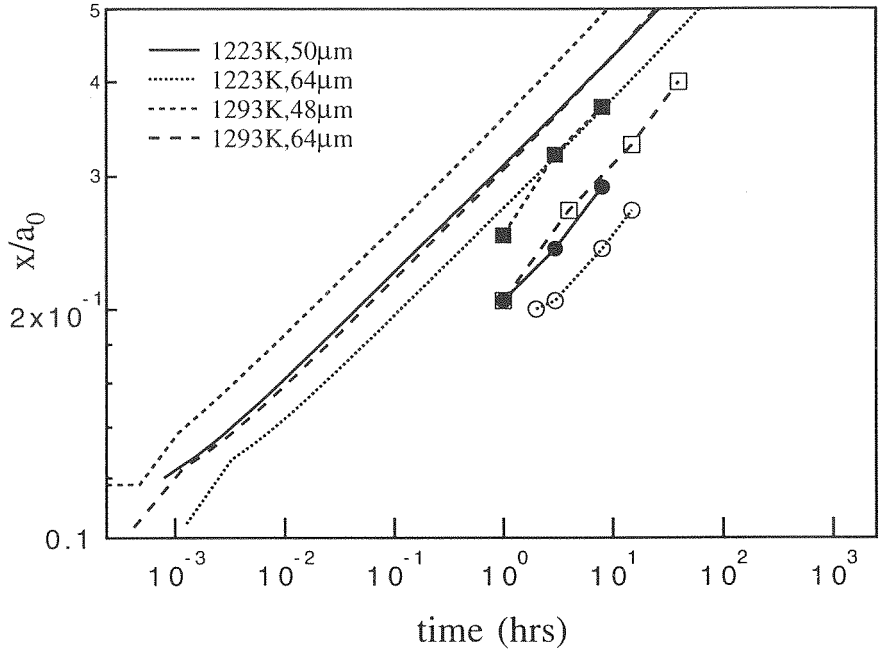

Figure 3.19: A comparison of experimental data from Wilson and Shewmon to model results. Results shown are for two temperatures, 1223K and 1293K, and three particle sizes, 48 μm, 50 μm, and 64 μm.

In addition, the contribution of multiple mechanisms can be calculated by integrating the sum of the individual sintering mechanism fluxes. The model thus makes it possible to examine the relative contributions of the different sintering mechanisms.

Model results show good agreement with a morphologically rigorous surface diffusion simulation performed by Nichols [8, 9]. Comparisons of the predictions of the two models suggest that our assumption of circular neck and particle surfaces leads to a modest overestimate of the fluxes early in the neck growth process.

The present model underpredicts experimental measurements of neck growth for copper spheres presented by Kingery and Berg [4] and Wilson and Shewmon [53]. It is worth noting that the calculations employed literature values of the relevant material properties. No attempt was made to adjust diffusion coefficients or other parameters

to improve the match between the predictions and the experimental observations. The estimated contributions of the different sintering mechanisms agree with those reported by Wilson and Shewmon. Uncertainties in the grain boundary diffusion coefficient are likely responsible for the difference between predicted and observed neck growth.

The model does not yet extend to prediction of neck growth beyond the "pill" shape, when the neck surface becomes cylindrical. The solution for the system geometry is also unstable at small neck times, limiting the range of applicability of the model. The present model does, however, demonstrate the limitations of the traditional small neck models. Inclusion of a more realistic system geometry and all relevant sintering mechanisms gives a much clearer interpretation of the sintering process.

	Silicon		Copper	
Atomic Volume (nm^3)	.01999		.0118	[46]
Density (kg/m^3)	$2348.9 - .0374T$	[50]	8960	[46]
Surface Energy (kg/s^2)	.736	[50]	1.72	[46]
Vapor Pressure (Pa)	$10^{-47.3+.043T-1.1e-5T^2}$	[50]	$1.23 \times 10^{11} e^{-234000/RT}$	[46]
Effective Grain Boundary Thickness (nm)	.543		.512	[46]
D_0, for Surface Diffusion (cm^2/sec)	9.36×10^6	[51]	26355	[46]
Activation Energy for Surface Diffusion, Q_s (kJ)	298	[51]	207	[46]
D_0, for Volume Diffusion (cm^2/sec)	154.88	[52]	.62	[46]
Activation Energy for Volume Diffusion, Q_v (kJ)	447	[52]	205	[46]
D_0, for Grain Boundary Diffusion (cm^2/sec)	300		.1	[46]
Activation Energy for Grain Boundary Diffusion, Q_b (kJ)	390		105	[46]

Table 3.3: Property data used for the model calculations.

Chapter 4

Sintering of Model Bisphere Silicon Aerosol Particles

4.1 Introduction

The engineering demands on ceramic materials has greatly increased in the last few decades. Due to their desirable thermal, mechanical, electrical and mechanical properties, new uses are constantly being discovered. Ceramic materials have not fulfilled all of the expectations for their use, largely due to the high variability in their material properties. That variability can be traced to problems in processing that are ultimately related to the properties of the starting powder. In recognition of this, severe demands are being placed upon the powder from which parts are created. The powder should be of high purity, with carefully controlled composition. Particles should be spherical and not aggregated, with controlled size distribution. Aerosol synthesis of ceramic particles, with its ability to control process composition and particle size

distribution, is an attractive process for forming desirable powders.

Several aerosol methods have been used to produce ceramic powders. Plasma reactors have been used to generate a wide variety of materials [54, 55, 56, 57]. Submicron powders of silicon nitride, silicon carbide, and other materials have been generated by laser induced chemical reaction of gaseous precursors [58]. Thermally induced reactions of gas phase precursors have also be used to produce a number of powders. Oxides have been produced by vapor phase oxidation of metal halides in flames [37, 21, 22] and furnaces [38, 39]. Silicon powder has been obtained by thermal decomposition of silane [59]. Metallic particle has been prepared by vaporization of solid precursors [41, 42, 43].

Regardless of the production technology, the initial stage of particle formation via aerosol vapor routes is production of sufficient vapor to produce a supersaturated state (Fig. 4.1). This vapor nucleates a large number of very small particles that undergo rapid coagulation. While the particles are quite small, they coalesce rapidly upon coagulation. As the aerosol cools, the particles eventually grow large enough that they can no longer coalesce completely between coagulation events. From that time on, the aerosol evolves as an aggregate with a complex ramified shape. Aggregates are generally undesirable in ceramic powders because they lead to substantial density variations in the green powder compact, and produce large voids that become a major cause for failure of the final part.

The equations that govern coagulation of spherical particles, i.e., when coalescence is instantaneous, are well developed. A description of the structual evolution when

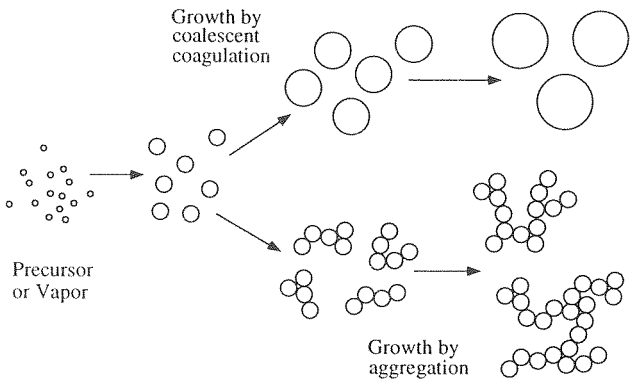

Figure 4.1: Representation of the coagulation/coalescence evolution of an aerosol population.

coalescence and coagulation take place on the same time scale processes is much less well understood. A number of models have been devised that incorporate a coalescence term into the aerosol population balance equations [37, 22, 23]. The coalescence term is usually written as a function of primary particle size or area, and is derived from traditional sintering models that describe the growth of the neck between the two particles [2, 3]. These models involve assumptions that are valid only for the initial neck formation, and may not accurately describe the entire coalescence process. Moreover, these models assume that only one transport mechanism contributes to the coalescence. In reality, many transport mechanisms may simultaneously contribute to coalescence.

In this chapter, we probe the dynamics of the sintering process by isolating it from competing processes. To do this, we have produced model bisphere agglomerates in a laboratory flow reactor. These bispheres are then processed at high temperatures while still entrained in the gas stream to facilitate a detailed study of the structural

changes due to sintering. Structural information is obtained from Transmission Electron Microscopy (TEM) observations of individual particles. Results will be compared to a model developed elsewhere (Chapter 3) that describes the geometry of the sintering of a two-particle agglomerate in detail including the contribution of multiple transport mechansims.

4.2 Particle Coalescence

Our interest is in the time required for coalescence of the bisphere that is produced when two solid spherical particles coagulate. The excess surface free energy of the particle system provides the driving force for coalescence. Variations in local surface curvature produces gradients in local vapor pressure, stress, and chemical potential, causing material to migrate into the neck region that joins the two particles. Several material transport mechanisms may contribute to coalescence, including: diffusion through the particle volume, grain boundary, or surface, transport through the vapor phase, and viscous flow. The contribution of any of these mechanisms depends upon the material properties and the environment in which sintering takes place.

When a single mechanism is active, the early phase coalescence can be described using classical sintering models that predict the increase of the neck radius between the spheres, x, relative to the sphere radius, a, generally expressed in the form

$$\hat{x}^n = \left(\frac{x}{a_0}\right)^n = \frac{B(T)}{{a_0}^m} t, \tag{4.1}$$

where a_0 is the initial radius of the spherical particle and the exponents m and n depend upon the particular sintering mechanism [2, 3, 4, 7]. For example, the values of m and n for surface diffusion are 7 and 4, respectively. These expressions are based upon simplified geometries that limit their applicability to a neck radius ratio of $x/a_0 \leq 0.3$. In spite of this limited range of validity, Eq. (4.1) has been used to estimate characteristic time for neck growth,

$$\tau_s = \frac{{a_0}^m}{B(T)}. \tag{4.2}$$

Ulrich first incorporated a coalescence term into a description of the structural evolution of aerosol particles [21, 22]. He had observed that the sizes of silica particles produced by flame synthesis were smaller than those estimated by coagulation calculations. He attributed this slow growth to rate limitations due to the coalescence of coagulating particles, in contrast with his previous coagulation calculations that were based upon instantaneous particle coalescence. He estimated the characteristic time for coalescence of silica by viscous flow, and calculated the evolution of the total number of primary particles in the silica agglomerates. Although agreement between his observations and the model predictions were poor, his model reproduced some of the qualitative features of his observations. Given the complexity of his experimental system, many factors likely contributed to the lack of quatitative agreement.

More recently, Koch and Friedlander [23] described agglomerate coalescence in terms of surface area. They hypothesized that the decrease in particle surface area

can be written as a first-order process, i.e.,

$$\frac{da}{dt} = -\frac{1}{\tau_s}(a - a_{sphere}). \tag{4.3}$$

This assumption was based upon calculations [17] that suggest for viscous coalescence, the total surface area approaches that of a dense sphere exponetially for $t >> \tau_s$. Koch and Friedlander applied the asymptotic form of the sintering term to the entire particle growth regime, from early times when particles coalesce quickly to later times when agglomerates persist. Most recent works have used this first-order rate expression to describe the evolution of agglomerate structures as they sinter [24, 25, 26, 44, 28]. Although the coalescence term Eq. (4.3) was based upon the assumption that viscous flow was the predominant mechanisms, this recent work has extended the model to include any one of the different sintering mechanisms. Model predictions have been compared to experimental work with limited sucess.

While considerable effort has been invested in solving the coupled coagulation/coalescence problem, following Ulrich's intial efforts, little attention has been paid to the form of the sintering term. Of the many problems associated with using Eqs. (4.1) and (4.3) to estimate the coalescence time, the consideration of a single sintering mechanism is most severe. Several transport mechanisms generally contribute to sintering simultaneously. The relative contribution of the different mechanisms change with variations in temperature, particle size and morphology. In particular, molecular diffusivities are strong functions of temperature, so the temperature variations that occur in all aerosol technologies are particularly important. The small

neck assumptions made in deriving this simple form can also be important.

Elucidating the kinetics and mechanisms of sintering from experimental observations of systems in which coagulation and coalescence occur simultaneously is difficult at best. Important system variables like particle size, initial neck growth, and temperature are nearly impossible to extract. To overcome these difficulties, we have developed methods for production of model aerosol agglomerates. These idealized particles are doublets of spherical silicon particles that are produced by low temperature coagulation. The only neck that exists between them initially is that formed during coagulation. These agglomerates provide a well characterized initial geometry that closely follows that which has been traditionally modeled in sintering studies. The bispheres are processed at a range of temperatures for various times while still entrained in the gas flow. The structures that result from this heat treatment will be compared to a model developed in Chapter 2 that follows the changes in geometry throughout sintering and includes all relevant sintering mechanisms.

4.3 Experimental Method

The experimental system consists of a three-stage aerosol reactor that is illustrated in Fig. 4.2. Briefly, a precursor gas of silane is pyrolized in the first reactor to produce aggregate silicon particles. These particles pass through a second higher temperature reactor stage where they densify into spherical particles. These dense spheres were then allowed to coagulate in an agglomeration chamber to produce small agglomerates (primarily doublets). Finally, the agglomerated spherical particles were heat treated

in a third reactor stage to examine the sintering.

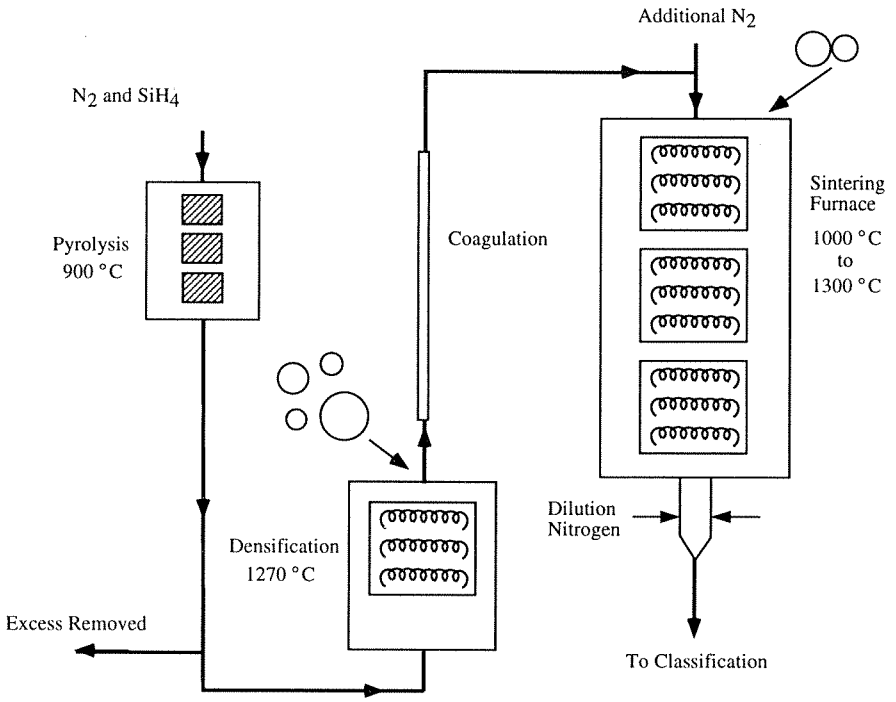

Figure 4.2: Schematic of the experimental setup used to produce and sinter model aerosol bispheres.

Before any of the reactors were turned on, the entire system was evacuated to around 2 mTorr and repeatedly purged with high-purity nitrogen (99.996%) that had been passed over hot copper shavings for additional oxygen removal. Following the purging, nitrogen flowed continuously through the entire system.

The first reactor stage was used to produce the silicon particles by pyrolysis of silane gas. It consists of a 1.3 cm i.d., 51 cm long quartz tube. A 25 cm length of the tube was heated with nichrome resistance wire heating elements to a temperature of 900 °C. A dilute mixture of silane in nitrogen prepared by mixing dilute silane (1% in N_2, Matheson) with additional high-purity nitrogen, was introduced into the top of the reactor. The total flow rate was 1.3 L min^{-1}, with a silane concentration of

0.077 percent by volume.

After exiting the first reactor stage, 87 percent of the flow was exhausted, reducing flow through the densification and sintering furnaces and increasing the residence times. The resulting particle stream was introduced into the bottom of the densification reactor at a flow rate of 0.26 L min^{-1}. This second reactor, which consists of a 1.9 cm i.d., 70 cm long alumina tube, with a total heated length of 23 cm, has reactor heating elements and operated at a temperature of 1270 C. The residence time in the reactor was 15 s.

The spherical silicon particles were then passed through an approximately 1.1 m length of 1/4 in copper tubing to allow for the aerosol to coagulate, and at the exit the aerosol population consisted primarily of bispheres, with some larger agglomerates. The particle stream was then introduced into the final sintering reactor, with high-purity nitrogen being added to the aerosol flow to control the residence time.

The final reactor, where the sintering experiments were performed, is a three-zone Lindberg furnace. (Model No. 54259-VS) It consists of a 1.0 cm i.d., 100 cm long quartz tube, with a total heated length of 65 cm. The furnace was capable of reaching temperatures as high as 1500 °C using silicon carbide heating elements. Previously existing insulation between the heating zones was removed in order to ensure a isothermal heating environment. Five Pt/5%PtRh thermocouples were attached to the surface of the quartz tube to monitor the heating profile. The aerosol stream exiting from the bottom of the Lindberg furnace was cooled by dilution with high-purity nitrogen that was transpired through a porous, sintered-stainless-steel tube to reduce

the gas temperature and minimize particle loss due to thermophoretic deposition onto the cold walls.

After exiting the final furnace, the aerosol stream was passed to the sampling and classification instrumentation, shown in Fig. 4.3. The size distributions of the final aerosol were measured over the size range of 8 to 250 nm by using a differential mobility analyzer (DMA,TSI Model 3071) with a condensation nuclei counter (CNC,TSI Model 3760) as a detector. Particles entering the DMA are passed through a ^{85}Kr source which is used to generate bipolar gas ions that attach to the particles. The aerosol is assumed to acquire a Fuchs distribution of charge [60]. The charged aerosol particles are then classified by their drift velocity in an electric field. Particles that fall within a certain mobility size range are extracted from the DMA and counted with the CNC. The instrument was operated as a Scanning Electrical Mobility Spectrometer (SEMS) in which the size distribution is obtained by exponentially ramping the voltage using computer control, and monitoring the counts obtained from the CNC as a function of time [61]. This allows complete size distributions to be obtained in as little as 1 min.

The DMA/CNC combination, however, only supplies limited, indirect information about the particle structure, namely the mobility equivalent size of the particle. The particle morphology cannot, in general, be deduced from the size distribution. To determine the particle structure, particles were collected on grids using the thermophoretic sampling probe illustrated in Fig. 4.4 for examination under a transmission electron microscope (TEM). The thermophoretic probe collects particles directly

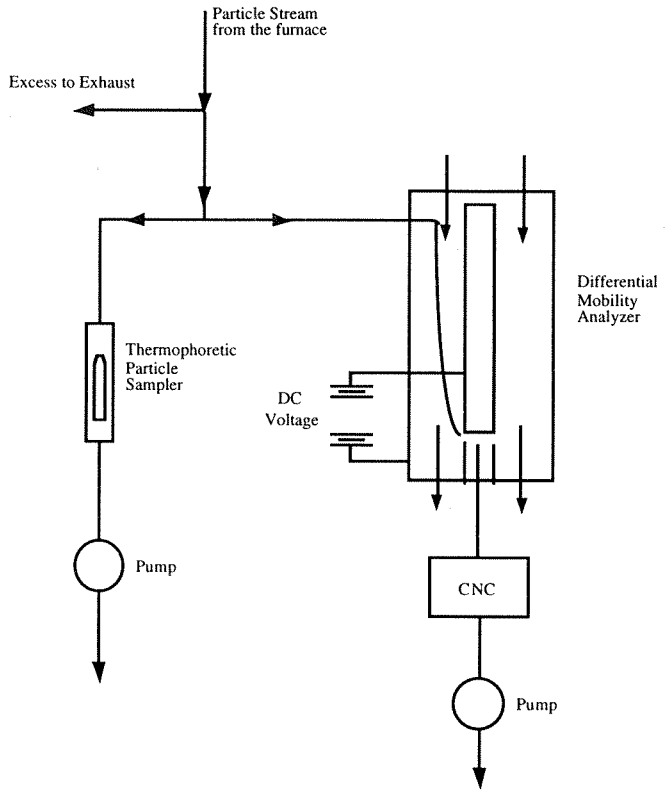

Figure 4.3: The instrumentation used to measure aerosol size distributions and obtain TEM grid samples.

from the particle stream onto a sampling grid by heating the aerosol stream and then passing it over a TEM grid that is mounted on the end of a copper rod. [62] Thermal diffusion of the particles in the sharp temperature gradient, a process called thermophoresis, drives the particles from the hot gas onto the cold grid. The temperature gradient could be enhanced by immersion of the other end of the copper rod in ice water or liquid N_2. The number of particles collected was controlled by adjusting the temperature gradient and collection time. The collection conditions were adjusted so that the particle coverage on the grids would be sparse, allowing for individual particles to be analyzed. Particles were collected on 400 mesh copper grids (Ted Pella Inc.) covered with a formvar or parlodian film.

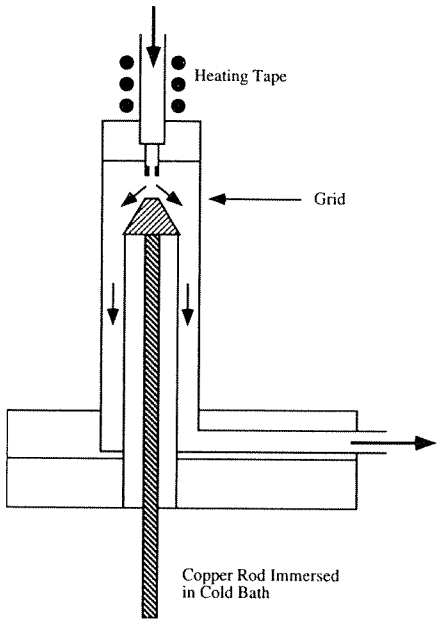

Figure 4.4: Schematic of the thermophoretic sampler used to sample particles entrained in the gas stream.

4.4 Image Analysis

The TEM (Model 210, Phillips Electronic Instruments) magnifications were determined to within 5 percent using a precision grating. During the microscope session, particles were selected and photographed randomly in order to minimize operator bias. Once a particle was selected, however, care was taken to ensure that it appeared to be lying flat on the grid substrate. If the bisphere was not lying flat, a darker "football" region could be seen in the neck area, indicating that the two particles were laying one on top of another, even if only slightly. A thin layer of silica exists on the surface of the silicon particles because the particles were exposed to air after sampling.

The TEM negatives were printed at approximately 7X magnification. These prints were subsequently scanned (HP Scanjet IIcx) in to a microcomputer (Mac-

intosh Quadra 800) using 100 dots per inch resolution. Automatic image processing proved difficult due to shading differences in the background of the print. Instead, the background was manually removed using an image processing program (Adobe Photoshop, V3.0), leaving only the particle. During this procedure, the extraneous surface features of the particle that weren't related to neck growth were removed. In addition, the component particles in each aggregate were separated at the adjoining neck so that the individual particles could be measured.

After background removal, the particles were imported into an image analysis program. (NIH Image, V1.52) Here, the particle images were thresholded and the image calibrated. Several binary operations to aid in thresholding the particle were tried; the total difference in measurements made from different approaches was approximately 2 percent. Measurements of the projected area and perimeter of both the sintered particle and its component particles were performed. The difference between the total bisphere perimeter and the individual particles perimeters gave a measure of the total neck size. In addition, the ellipse major and minor axes fitting each of the component particles were measured. Using these values, the particle volume was inferred from the two-dimensional images.

4.5 Results

The two primary control variables in the sintering study were: (i) the sintering temperature, and (ii) the sintering time (the residence time for particles within the reactor). The bisphere size distribution was constant throughout the experiment, and was

verified in situ using the DMA. The sintering times and temperatures were varied to elucidate general sintering behavior. The sintering temperature ranged from 1000 °C to 1300 °C. Particle residence times were varied between 1 to 11.8 s.

4.5.1 Sintering Behavior

Figure 4.5 shows a typical doublet particle prior to sintering. A small neck has formed between the particles, but it can be considered a weak or "soft" bond. The individual particles are fairly close to spherical. There is some indication that some are poly crytalline, and that twins or related structures have formed in some particles. It is reasonable to expect that some particles will be poly crystalline since the individual spheres were produced by coalescence of agglomerates of smaller particles. Figure 4.16 shows a particle that has been sintered at 1000 °C for 4.6 sec. No appreciable neck growth can be seen. Indeed, no neck growth was observed until the sintering temperature approached 1100 °C.

Figs. 4.17 through 4.21 show a sequence of micrographs obtained from samples that were sintered at 1100 °C for a number of residence times. The particle that was sintered for the shortest time (Fig. 4.17) shows a substantial neck and a distinct grain boundary. In other particles (Figs. 4.18 and 4.20), there is no discernable demarcation between particles. Although the surface structure of the particles changes dramatically with sintering time, the neck size does not change appreciably with a five-fold increase in time. The individual spheres have not, in general, retained a spherical shape during sintering, and in some particles, crystal planes are emerging.

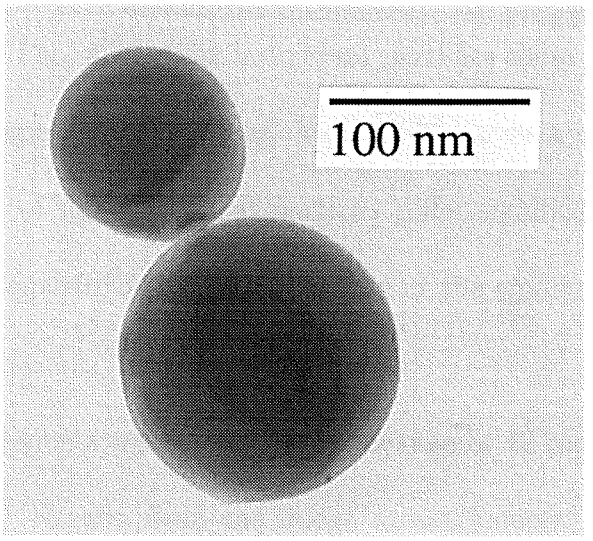

Figure 4.5: An as-produced bisphere that has not been sintered.

Similar results occur for particles sintered at 1200 °C (Figs. 4.22,4.23,4.24). Figure 4.23 shows an obvious grain boundary, and a predominance of crystal planes. The other particles show some evidence of crystal planes, but the surfaces seem more "rounded." Most particles at this temperature show a distinct angle where the surface and the grain boundary meet. Again, all particles seem to have the same degree of neck growth.

It is not until 1300 °C that the bispheres approach their final spherical shape, as shown in Fig. 4.25. A grain boundary can be seen dividing the particle shown in Fig. 4.26 through the middle.. Figure 4.27 shows what appears to be a three particle system approaching spherical shape. The grain boundaries between the original particles can just be made out on either end of the elongated sintered particle. At shorter residence times, some particles retain discernable neck regions, as shown in Figs. 4.28 (2.4 sec) and 4.29 (1.6 sec).

Other interesting structures were found. Three particles that have sintered to each other is shown in Fig. 4.30. The individual particles must have coagulated close to this triangular shape before sintering. Figure 4.31 shows a partially sintered doublet in which the sizes of the component particles differ significantly. The larger particle seems relatively unperturbed by the presence of the smaller one, retaining a nearly spherical shape.

Image measurements were made on an average of 10 particles per sintering time and temperature. Results from the image measurements are summarized in Figs. 4.6 and 4.7. The extent of neck growth is larger for the higher temperature. The average neck growth, x/a_0, appears to be approximately .5 for 1100 °C and .65 to .7 for 1200 °C. The results presented in Fig. 4.7 show that the extent of sintering in the smaller particle increases for increasing particle size ratio, and that this effect becomes more pronounced at the higher temperature. Comparisons with the results of the model developed in Chapter 3 show that a particle of mean size 50 nm should sinter to a similar neck size in 10^{-6} s. Model results for the relative contribution of the different sintering mechanisms to neck growth for a 50 nm particle is shown in Fig. 4.8 and Fig. 4.9 for 1100 °C and 1300 °C respectively. They suggest that surface diffusion should totally dominate the sintering process.

4.5.2 Surface Structures and Morphology

The TEM photos of the particles possess a number of curious surface structures. The nature of the deposited material changes with temperature and residence time. At

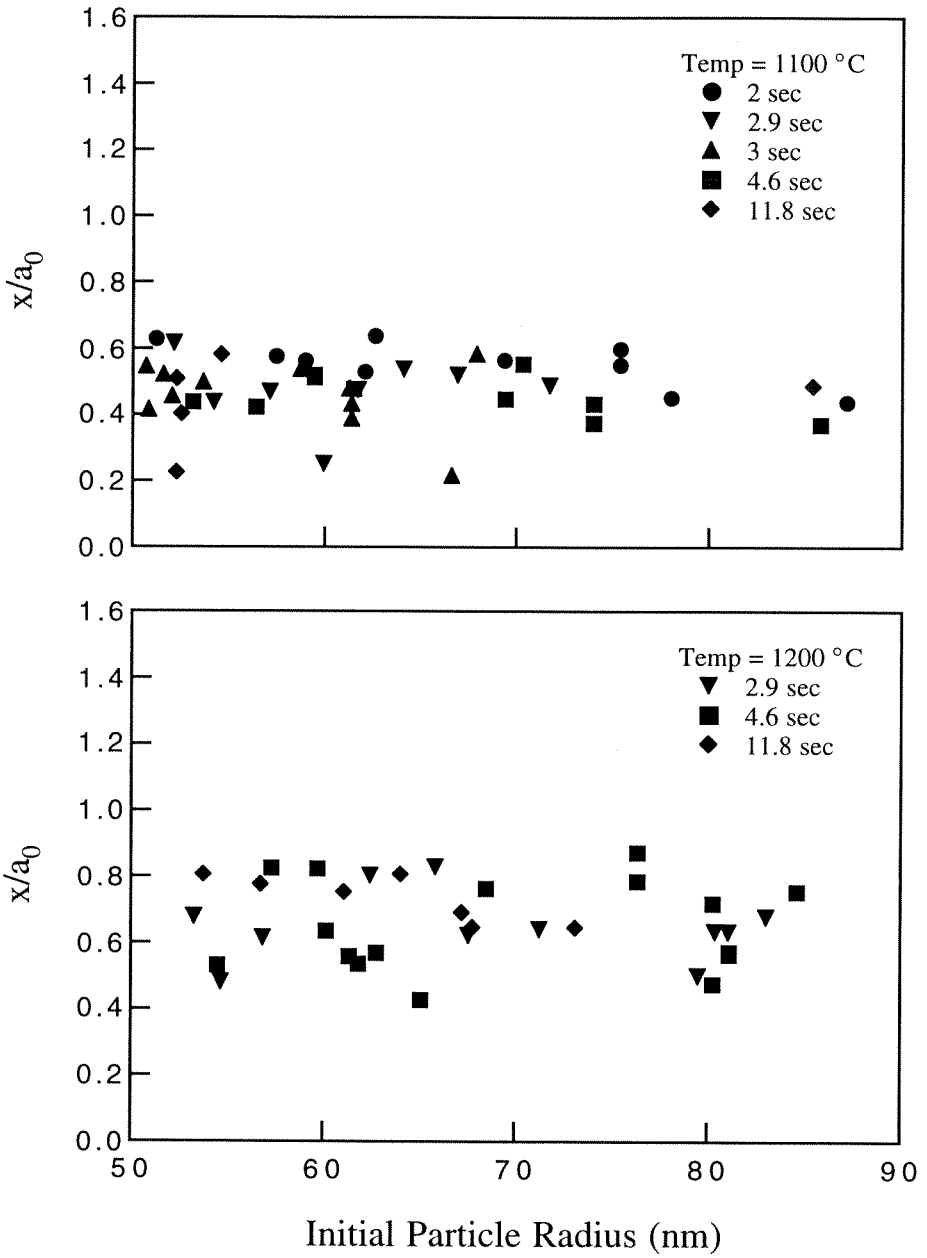

Figure 4.6: Results for neck growth measured from TEM images for particles sintered at 1100 °C and 1200 °C.

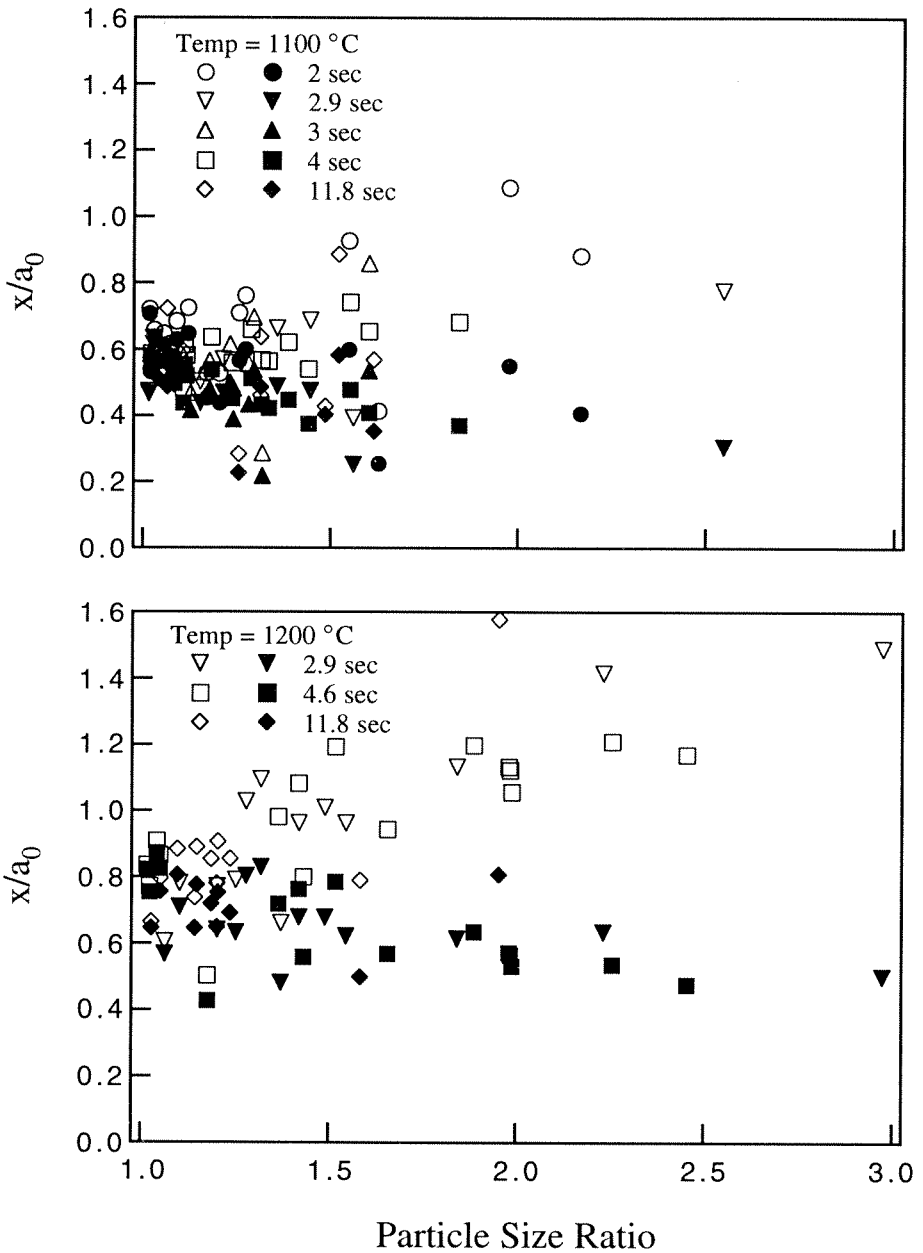

Figure 4.7: Results for neck growth measured from TEM images for particles sintered at 1100 °C and 1200 °C as a function of the ratio between the two particles. The unfilled circles represent neck growth based upon the smaller particle, and the filled circles represent neck growth based upon the larger particle.

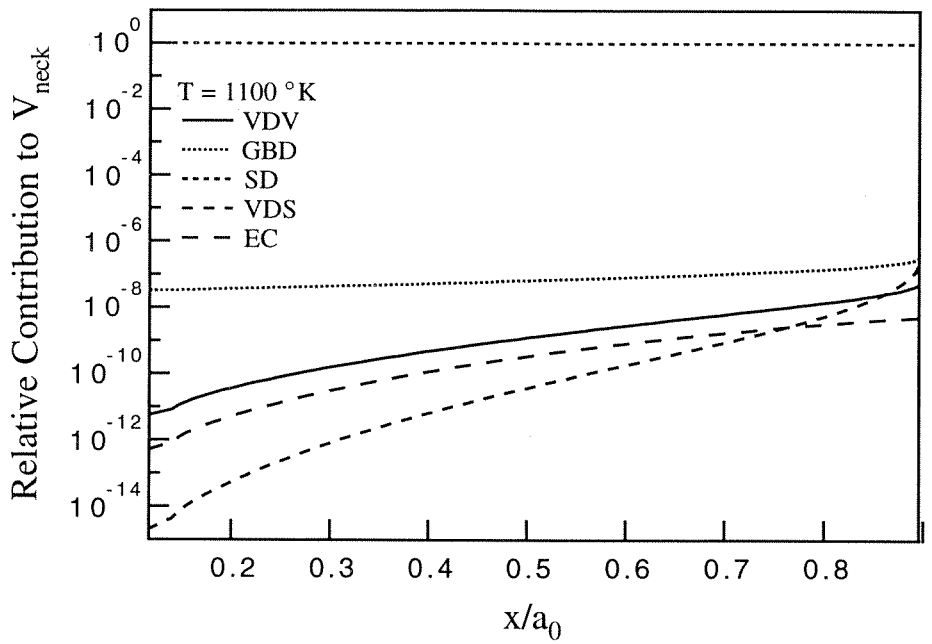

Figure 4.8: The relative importance of individual mechanisms during the sintering of 50 nm silicon spheres at 1100 °C.

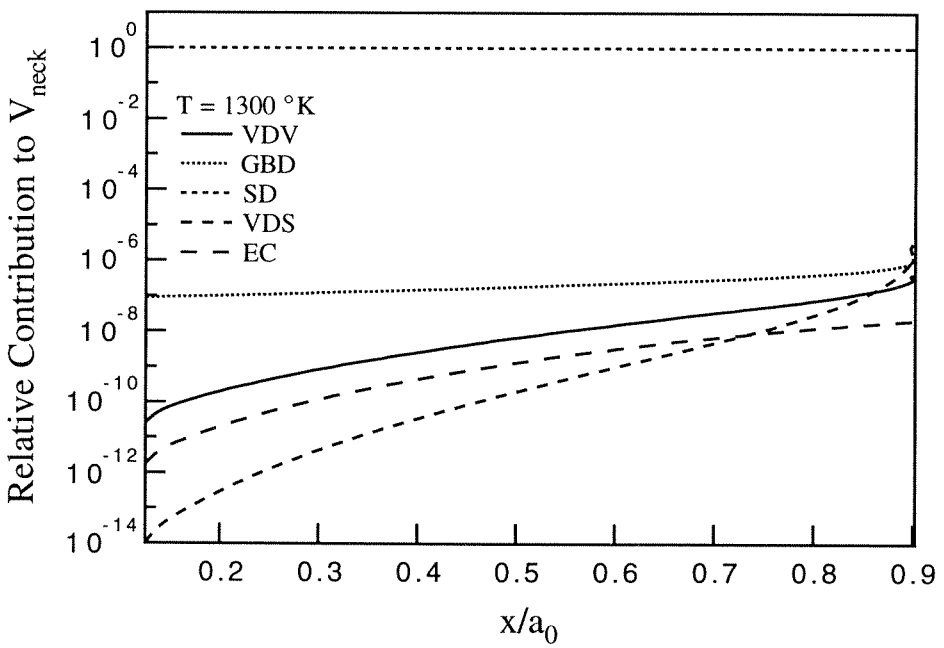

Figure 4.9: The relative importance of individual mechanisms during the sintering of 50 nm silicon spheres at 1300 °C.

long residence times and low temperatures, the deposits are elongated, fairly small (about 5 to 10 nm in size), and uniformly distributed over the particle surface. (Figs. 4.21 and 4.24) At longer residence times, the deposits appear to flatten and coalesce into the particle surface, as seen in Fig. 4.20. Particles sintered for short times show little deposited material. In many cases the small amount of material that is present appears to have migrated to the corners of two planes. This can be seen quite clearly in Fig. 4.23.

One possible explanation for these structures is that the vapor around the particle condensed in a random fashion on the particle surface during sintering. A far more likely explanation is that small scale structures on the surface of the particles are artifacts of the exit region of the furnace. As the particles exit the furnace and cool, vapors that have evolved in the high temperature region of the sintering reactor nucleate, producing a secondary aerosol of small agglomerates that deposit on the particles. Short residence times are accompanied by high cooling rates which produce high supersaturations that favor homogeneous nucleation of the vapor over heterogeneous condensation on the starting particles. The fine nuclei then coagulate amongst themselves to produce a separate mode in the particle size distribution that is seen in Figs. 4.11 through 4.13, or with the starting particle to produce surface structures such as that shown in Fig. 4.10.

The dynamics of formation and growth of these secondary nuclei are complex. The flow rate through the sintering reactor determines the time available for agglomeration of the secondary nuclei with the larger particles. It also affects the rate of

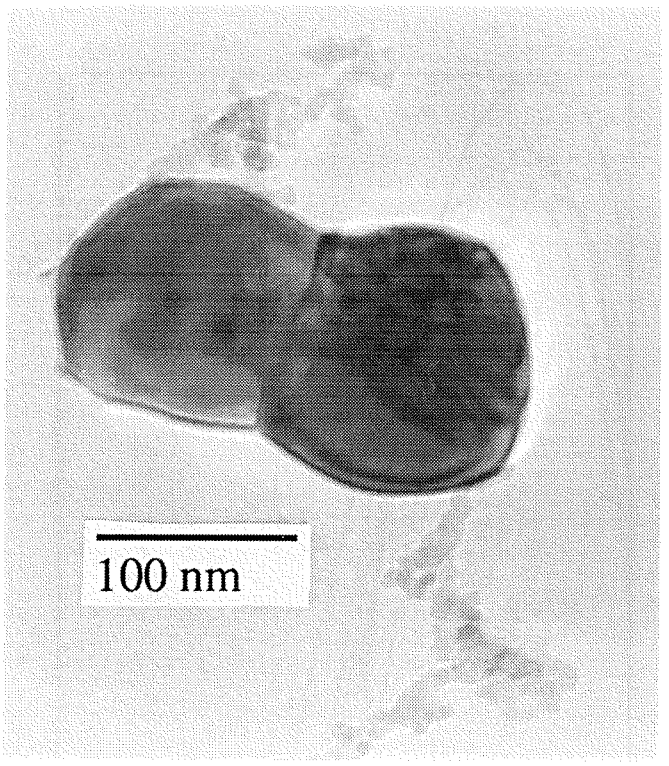

Figure 4.10: Bisphere sintered at 1300 °C for 1 s that shows large nuclei formed from cooled vapors that have deposited onto the particle surface.

cooling which controls both the nucleation process and the extent to which the secondary nuclei coalesce with the larger host particles following agglomeration. The persistence of the surface structures is an indication that cooling is sufficiently rapid that coalescence is slow, even for these very small structures. At low flow rates and long residence times, the deposition of the secondary nuclei is relatively complete, however the particle has cooled sufficiently that coalescence upon deposition is inhibited, leading to the surface structures seen in Fig. 4.21. Higher flow rates accelerate the cooling of the gas, however, the particle temperature remains high enough that coalescence is relatively complete, producing surface structures like those shown in

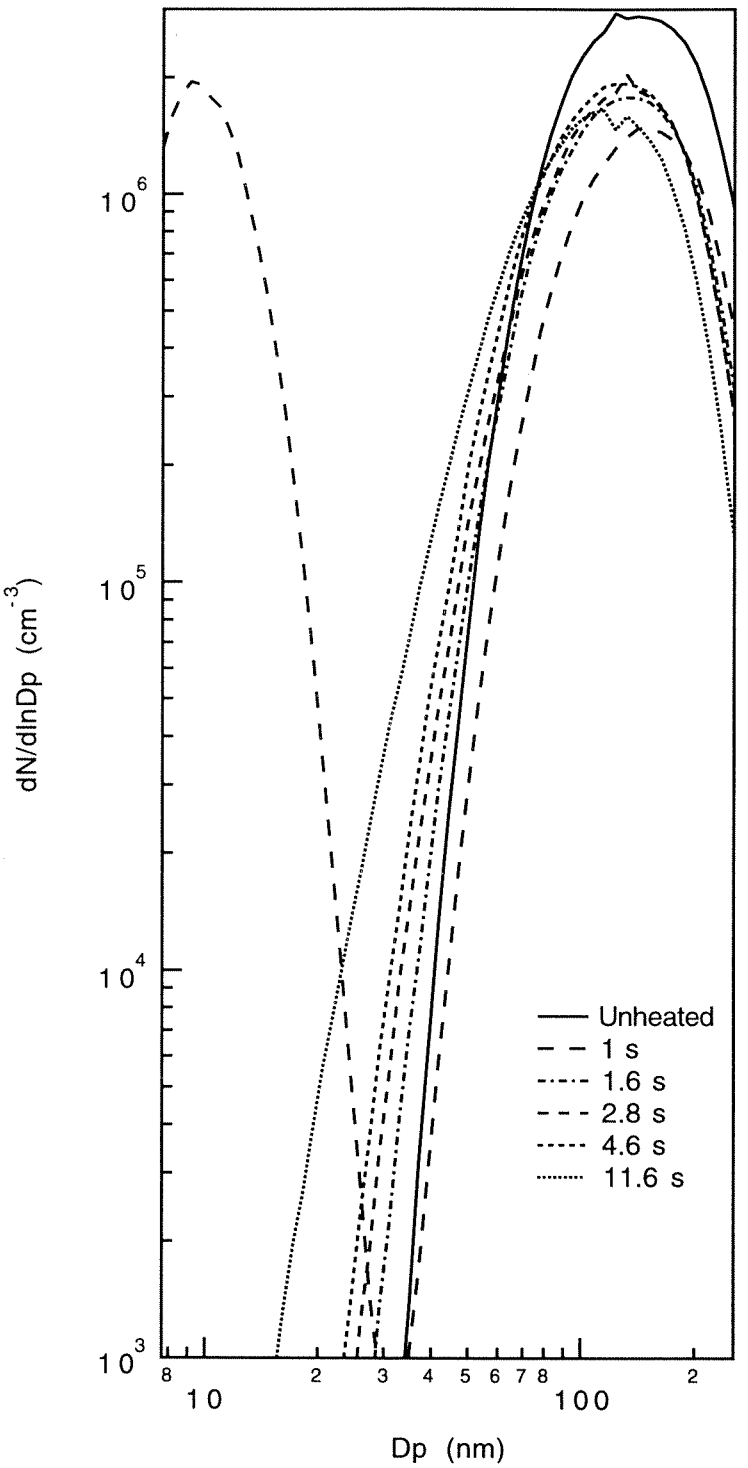

Figure 4.11: Size distributions of the agglomerated aerosol sintered at 1100 °C for different times.

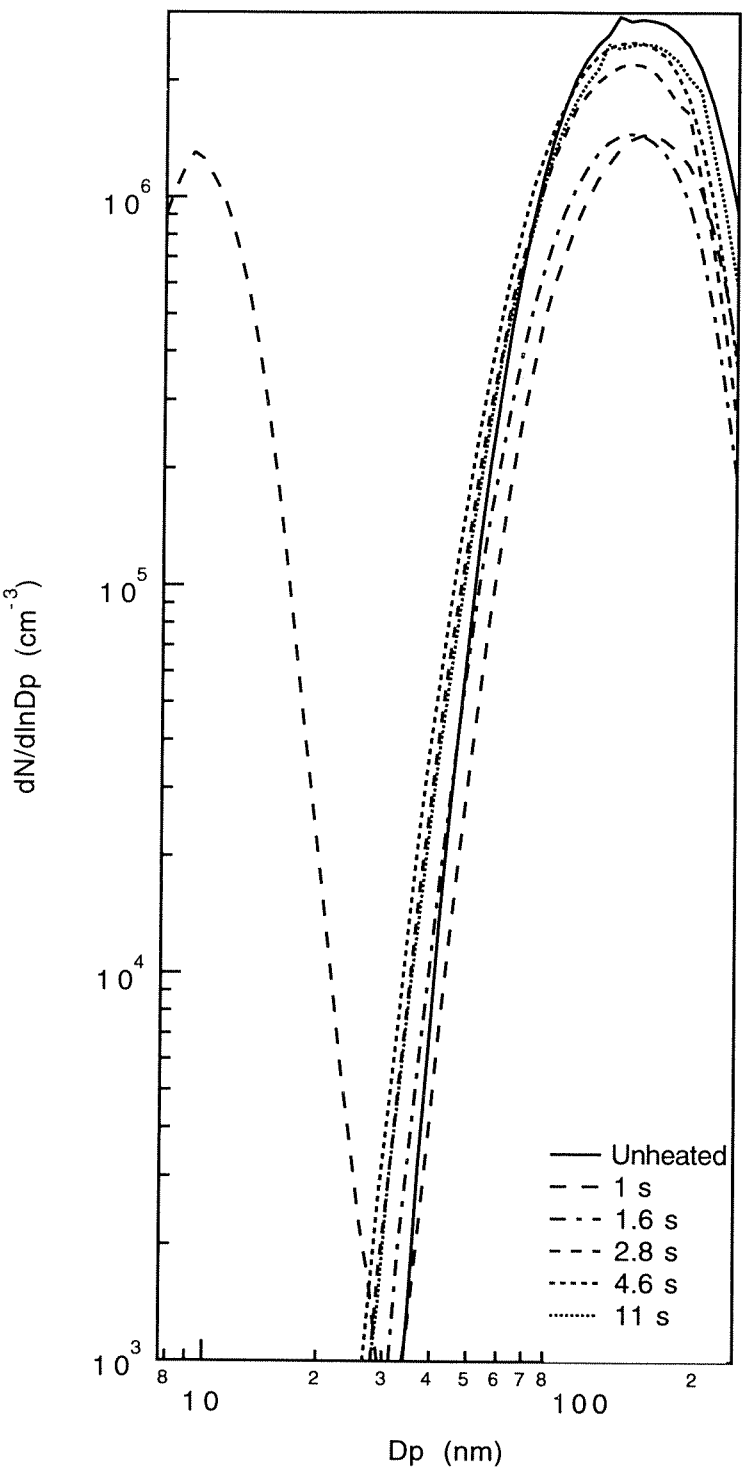

Figure 4.12: Size distributions of the agglomerated aerosol sintered at 1200 °C for different times.

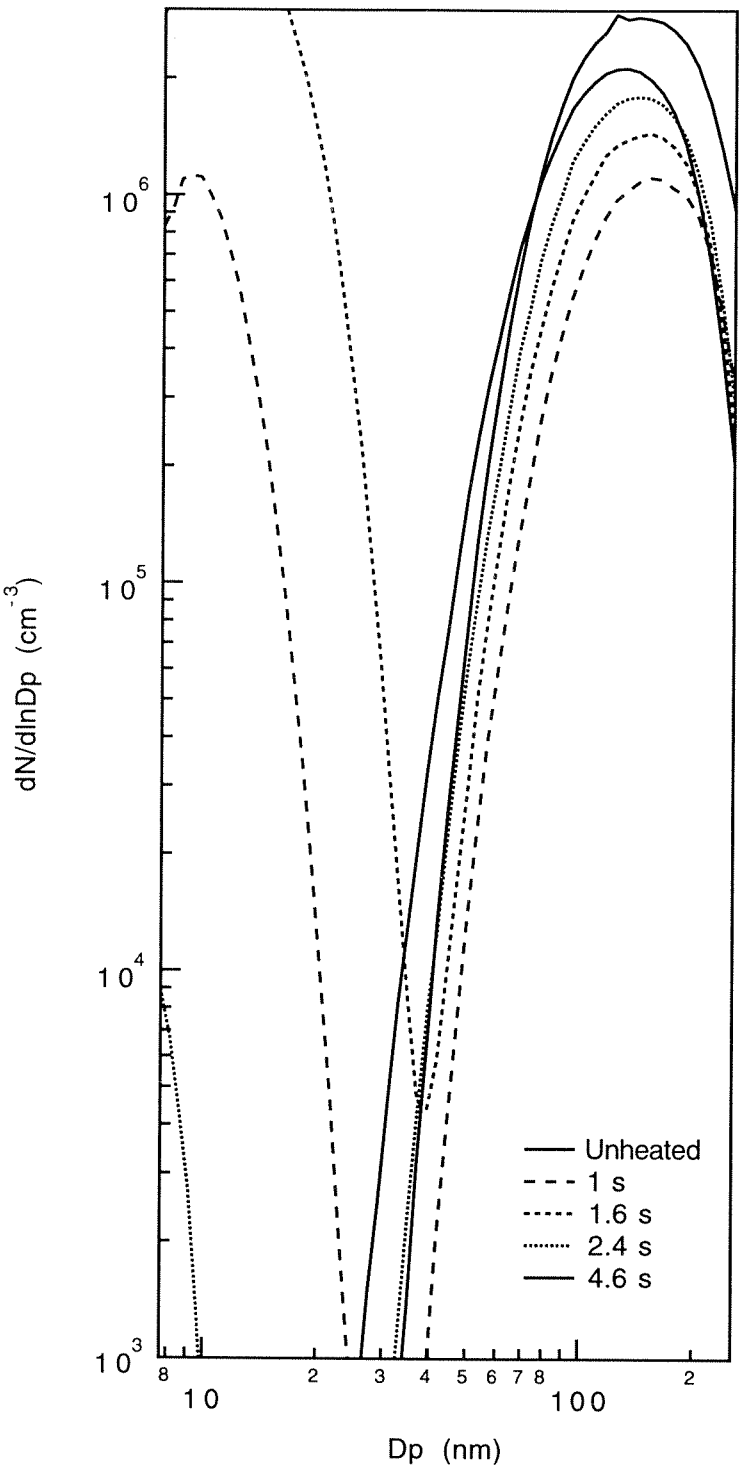

Figure 4.13: Size distributions of the agglomerated aerosol sintered at 1300 °C for different times.

Fig. 4.20. Few surface structures are seen on the particles processed at the highest flow rates. Those that are present are concentrated at the vertices of the crystallites (Fig 4.23). It is important to note, however, that these surface features are generated as neck growth is being quenched by cooling. Thus, in spite of the complexity that they add to the particle structure, they are unlikely to significantly influence the neck growth that is the primary factor of this work.

The particles sometimes show extensive surface faceting, particularly those particles processed at 1200 °C. At 1100 °C, the particles with the most faceting occur at 2 sec, Fig. 4.17. Some faceting does occur at longer times, as shown in Fig. 4.32 for a particle sintered at 1100 °C for 11.8 sec. For 1200 °C, there is significant faceting at all residence times, however it peaks at 4.6 sec. (Fig. 4.23). After the agglomerate has completely sintered, however, the particle regains a spherical shape (Fig. 4.25). Indeed, sintering was employed in the densification reactor to produce the spherical particles from which the bispheres were generated. This suggests that the spherical shape is the favored morphology at the temperature of our experiments and raises the question of why facets appear at intermediate states.

One possible cause for facet development is the deposition of secondary nuclei on the surface of the larger particles. The very small radius of curvature at the junction between large and small particles leads to rapid diffusive motions that may contribute to faceting and explain why the deposited fine particles are usually found at a vertex of the facets. High cooling rates favor nucleation and, therefore, increase the frequency of depositions of the fine particles onto the larger ones. The densification reactor

represents the extreme in our experiments, with residence times on the order of 13 to 15 s and gradual cooling of the aerosol leaving the reactor. No faceting or deposited fine particles were observed in the particles leaving this reactor. Thus, the faceting appears to be an artifact of the rapid quench. While the change in the particle morphology is dramatic, the sizes of the necks between the larger particles should not be significantly perturbed by this rearrangement that occurs late in the cooling process.

The appearance of facets in the particle surface minimizes the total surface free energy. Why, then, do particles return to the spherical shape late in the sintering process? A mechanisms that can transport material to unfavorable locations is required. Material evaporated from small particles with high overall surface energy may condense on relatively unfavorable locations on larger particles. A high rate of such mass transfer couples with limited surface mobility may account for the return to the spherical shape. Clearly, the structural rearrangements associated with fine particle deposition are an intriguing area for future research.

4.6 Discussion

4.6.1 Sintering Mechanism

The sinterability of silicon was first studied by Greskovich and Rosolowski [63]. Covalent solids such as silicon are generally difficult to densify. This suggests that the predominant mechanism is one that causes adhesion without densification. Based

upon scaling laws proposed by Herring [64] and on observations of weight loss during sintering, Greskovich and Rosolowski concluded that evaporation and condensation was the predominant mechanism of material transport. All of the powders used in their experiments had been exposed to oxygen prior to sintering and were assumed to have an oxide layer on particle surfaces.

These conclusions came into question when the measurement of surface diffusivity of silicon [51] suggested that surface diffusion, and not vapor-phase transport, should dominate in silicon. Subsequent studies by Shaw and Heuer [65] once again suggested that vapor-phase transport dominated by Si-0 could account for the observed lack of sintering and weight loss, but they did acknowledge the contradiction presented by the surface diffusion data. Studies on ultrafine silicon powders (0.02 to 0.1 μm in size) by Möller and Welsch [66] concluded from measurements of the activation energy for densification that a diffusion process is the dominant densification mechanism, although their results also showed evidence of vapor-phase transport. They also reported that no apparent sintering occurred below 1100 °C. More recently, Coblenz stated that surface diffusion was the predominant sintering mechanism in silicon [67]. In his experiment, he was able to observe the sintering that occurred after the oxide layer had been removed. He concluded that oxide layers that develop rapidly when silicon is exposed to air inhibit surface diffusion and allow competing sintering mechanisms to dominate.

Our results support surface diffusion as the predominant sintering mechanism for silicon. The model results shown in Figs. 4.8 and 4.9 show that sintering should

occur almost entirely by surface diffusion. Furthermore, the development of surface facets suggests a high degree of surface mobility in as-synthesized silicon particles. The presence of the deposited structures that resulted from vaporization suggest that it might contribute to sintering. However, the material vaporizing from the particle surface is much more likely to move into the gas surrounding the particles (where the relative vapor pressure is low) than to the neck of the particle.

4.6.2 Neck Growth

Neck growth appears to cease at an intermediate point, and subsequent evolution of the particle is dominated by surface changes. Lange and Kellett [12] predicted this behavior in their study of the role of the dihedral angle in sintering. They modelled the densification of particles using a thermodynamic approach to simple particle arrays. The energy per particle was written by summing the energies associated with the particle's free surface, A_s, and grain boundary, A_b as

$$E = \gamma_s A_s + \gamma_b A_b \tag{4.4}$$

where γ_s and γ_b are the energies per unit area associated with the surface and grain boundaries, respectively. These energies are related through Young's equation,

$$\gamma_b = 2\gamma_s \cos(\phi_e/2), \tag{4.5}$$

where ϕ_e is the equilibrium or dihedral angle associated with the intersection of a surface and grain boundary. Thus, the total system energy becomes

$$E = \gamma_s[A_s + 2\cos(\phi_e/2)A_b]. \tag{4.6}$$

Differentiation of Eq. (4.6) with respect to A_s shows that the neck will cease to grow when $dA_s/dA_b = -2\cos(\phi_e/2)$.

Neck interface angles were measured for the particles sintered at 1100 °C and 1200 °C and the results are presented in Fig. 4.14. The particles sintered at the higher tempererature have larger angles, and the angle increases slightly with increasing sintering time. These results suggest that the equalibrium configuration has been approached, and that the equalibrium angle increases with temperature.

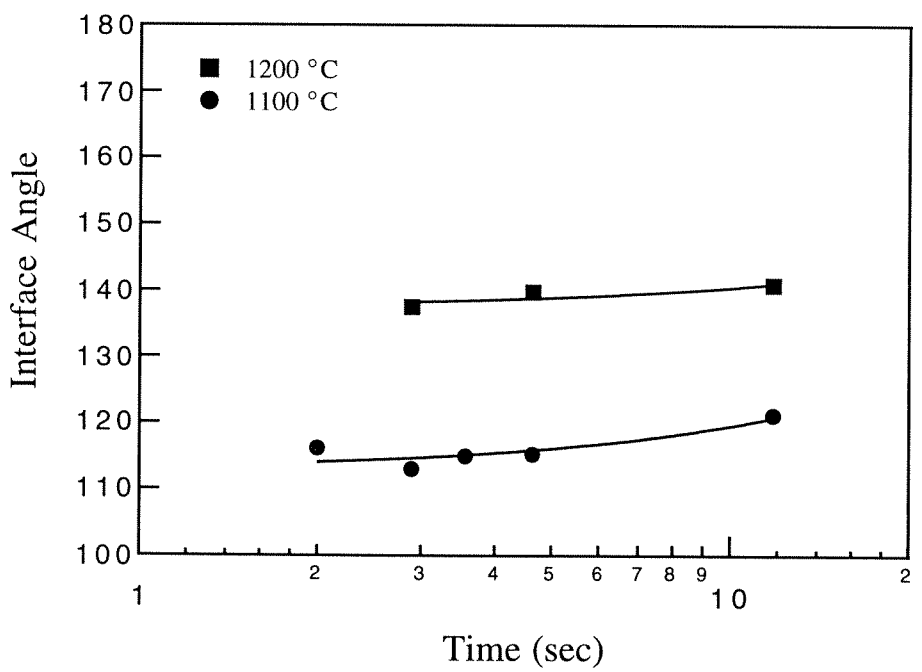

Figure 4.14: Measured grain boundary interface angles for particles sintered at 1100 °C and 1200 °C.

Obviously, this equilibrium applies only to the driving force for neck growth. The system still seeks to lower its excess surface area. From this point, the system will seek to lower its energy through interparticle mass transport, or coarsening, where one particle grows at the expense of another [13]. The evaporation of material from the surface of one particle may contribute to the restructuring of others. At the same time, variation in the local surface curvature continues to drive local surface flows. During this phase of coalescence, the grain boundary may become unpinned and move through the smaller particle. Its ability to do this will depend upon the dihedral angle and the size difference between the two particles. A schematic of these configurational changes is shown in Fig. 4.15. Figure 4.33 shows a particle that appears to exhibit this phenomena.

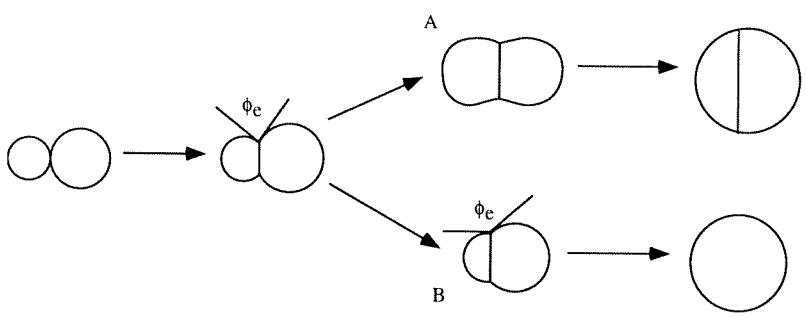

Figure 4.15: Configurational changes during sintering and interparticle mass transport. In (B), the grain boundary becomes unpinned and moves out of the particle during coarsening.

The present results indicate that the sintering has proceeded to equilibrium with respect to the grain boundary energy. The fact that the equilibrium angle appears to increase slightly with sintering time implies that coarsening is occurring. Some particles have progressed beyond this equilibrium point, and the grain boundary

appears to be moving out of particle system (Figs. 4.33 and 4.34). Figure 4.35 shows a three-particle system in which the grain boundaries seem to be moving through the center particle, resulting in a new two particle configuration.

4.7 Conclusions

Aerosol techniqes have proven useful for the study of sintering. The ability to produce dimers of spherical particles makes it possible to measure structure changes due to unconstrained sintering from a well characterized initial geometry. Sintering can be performed in situ, with particles sintered while still entrained in the gas stream in which they were formed, giving a high degree of control over the process. Contaminating factors associated with sample preparation and introduction into a sintering furnace are avoided.

The results from the experiments were somewhat surprising. There was little change in the extent of sintering for particles heated at the same temperature and different residence times, although sintering theory predicts that neck growth should have progressed much further. The two spheres have reached an equilibrium with respect to the grain boundary energy, as predicted by Lange and Kellett [12]. Measurements on interface angles support this conclusion. Some photos show grain boundaries that have become unpinned and appear to be moving out of the particle system.

Coarsening is an important phase of aerosol agglomerate coalescence that has been omitted from previous theoretical investigations. The neck grows quickly until the difference between the surface energy and the grain boundary energy of the ag-

glomerate becomes small and a metastable dihedral angel is formed. Following the rapid particle neck growth, we observed that the surface structures of small silicon agglomerates evolve slowly. Only after this rearrangement did the particles coalesce.

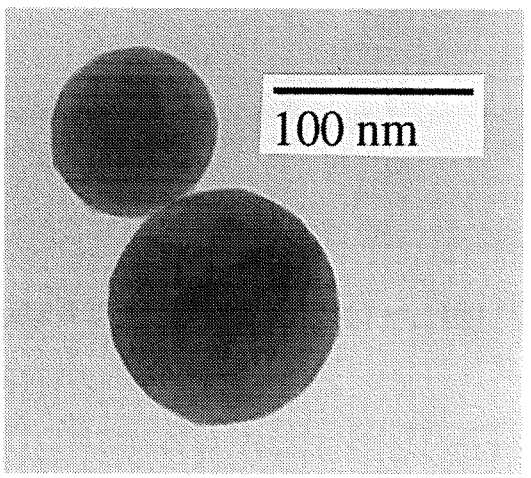

Figure 4.16: Bisphere sintered at 1000 °C for 4.6 sec.

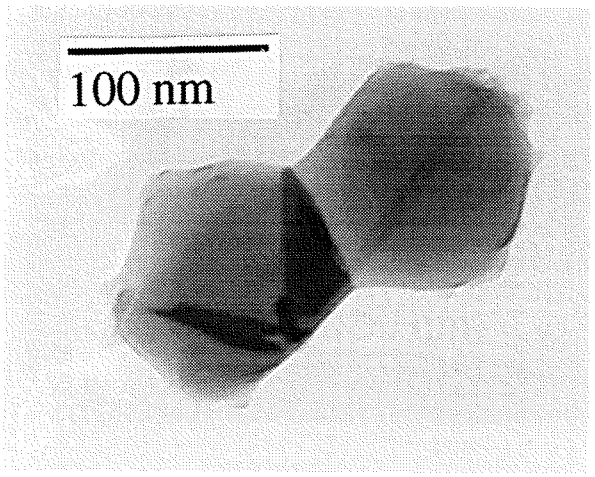

Figure 4.17: Bisphere sintered at 1100 °C for 2 sec.

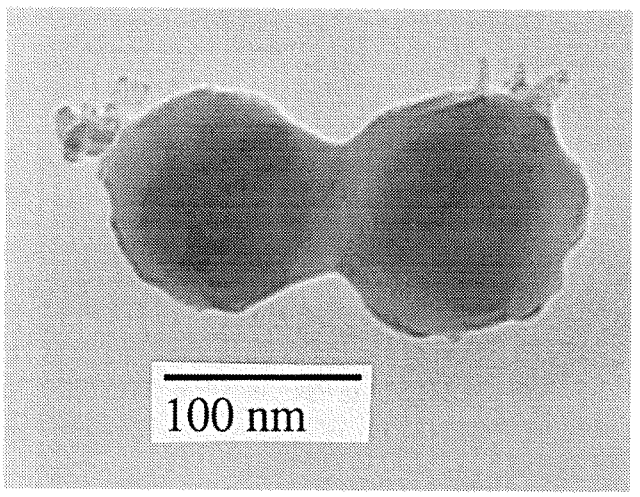

Figure 4.18: Bisphere sintered at 1100 °C for 2.9 sec.

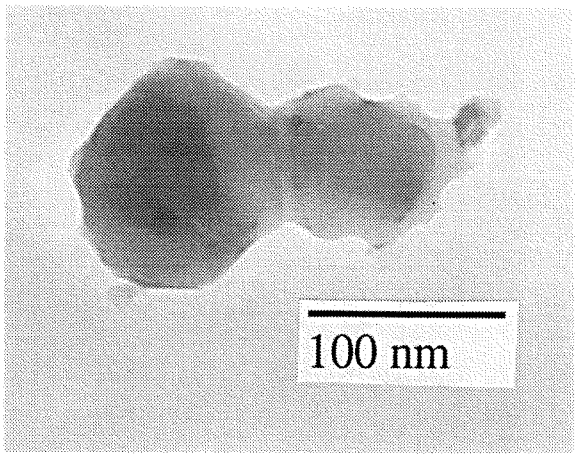

Figure 4.19: Bisphere sintered at 1100 °C for 3.56 sec.

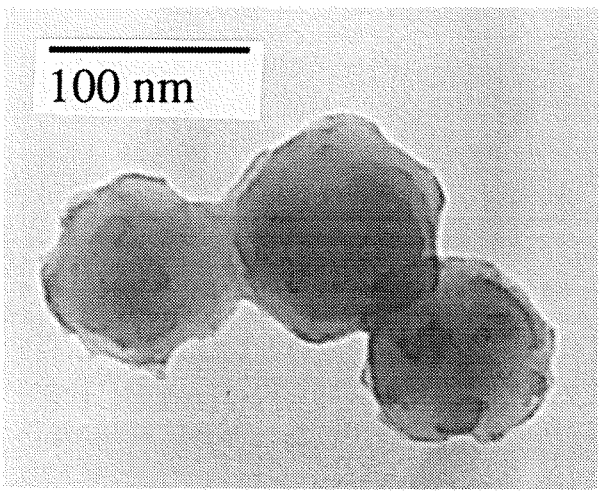

Figure 4.20: Three spheres sintered at 1100 °C for 4.6 sec.

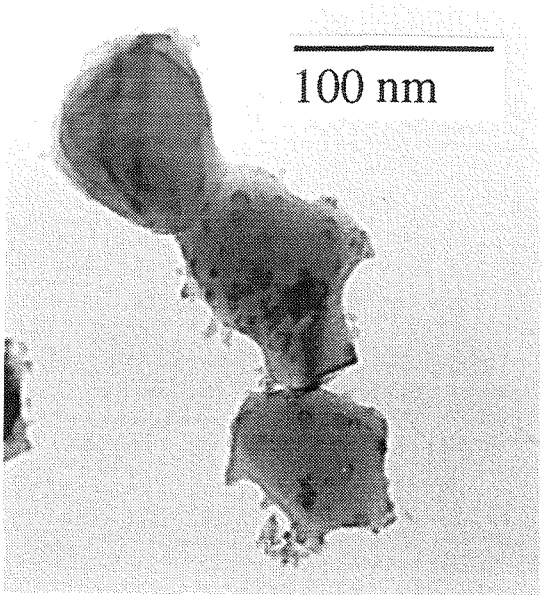

Figure 4.21: Bisphere sintered at 1100 °C for 11.8 sec.

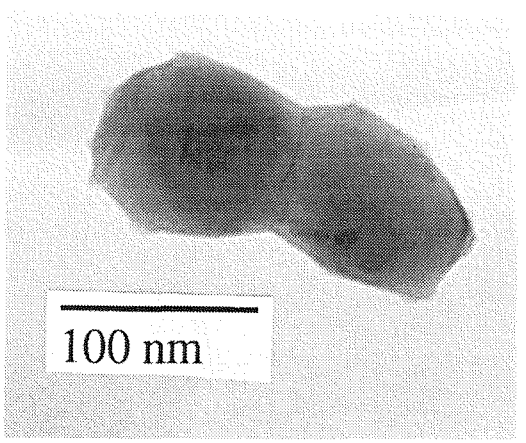

Figure 4.22: Bisphere sintered at 1200 °C for 2.89 sec.

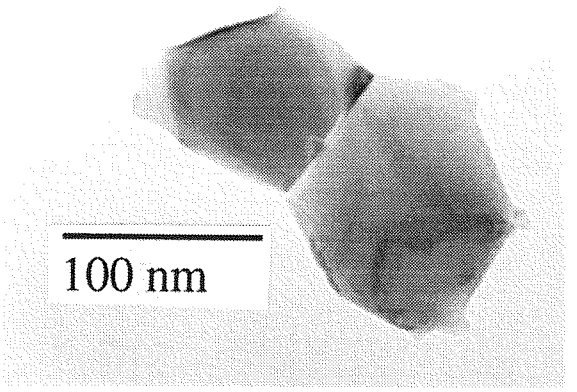

Figure 4.23: Bisphere sintered at 1200 °C for 4.6 sec.

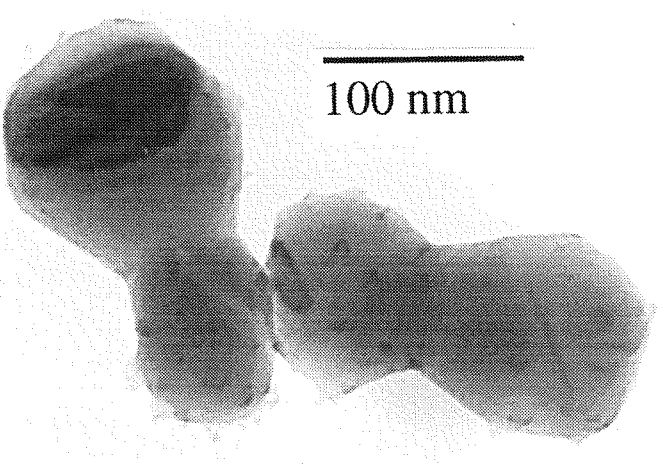

Figure 4.24: Bispheres sintered at 1200 °C for 11.8 sec.

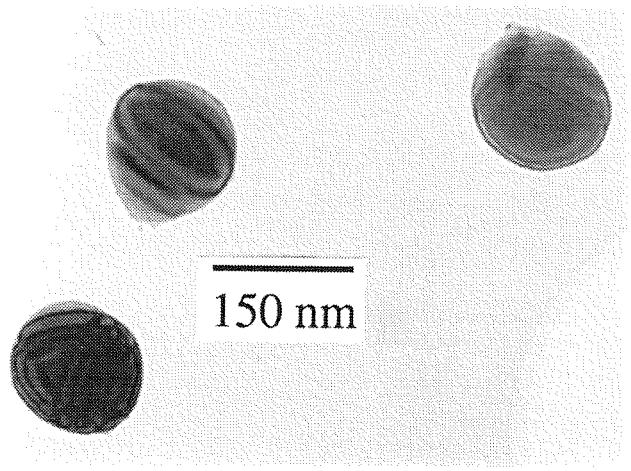

Figure 4.25: Three particles that have been sintered at 1300 °C for 4.6 sec.

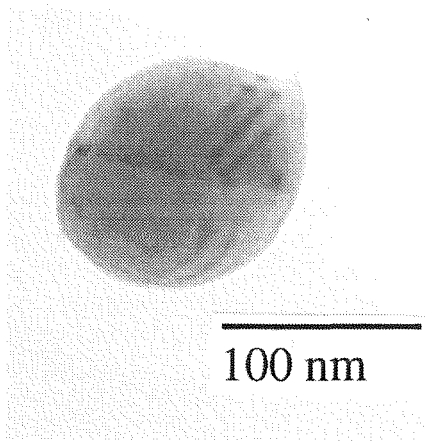

Figure 4.26: Bisphere sintered at 1300 °C for 4.6 sec.

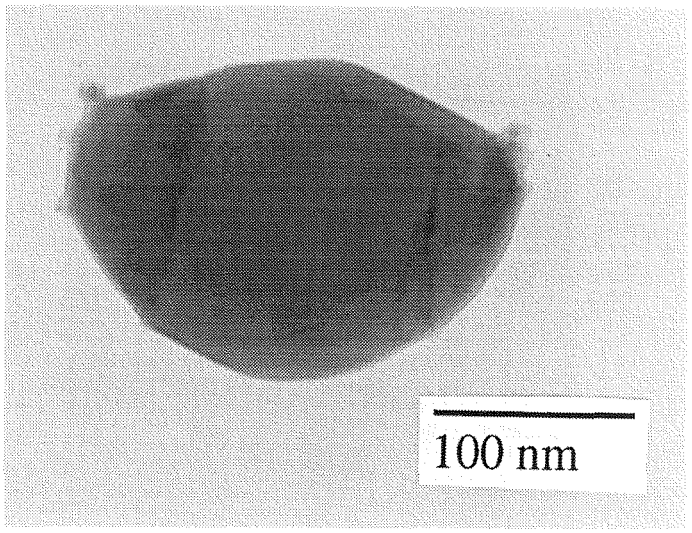

Figure 4.27: Three particles sintered 1300 °C for 4.6 sec that are approaching a final, spherical shape.

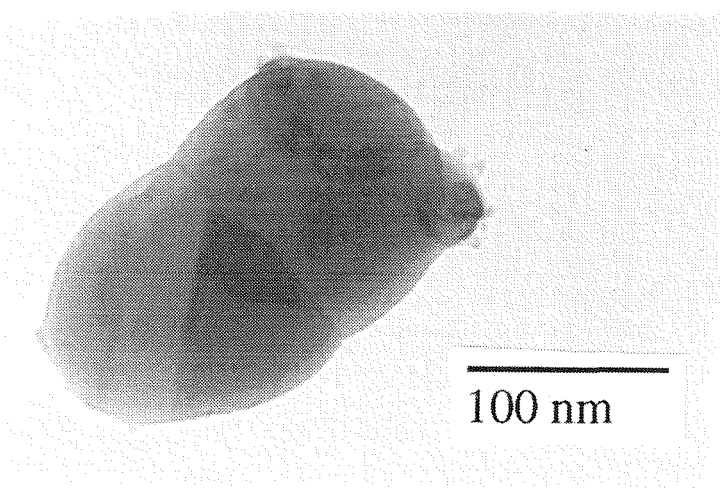

Figure 4.28: Bisphere sintered at 1300 °C for 2.4 sec.

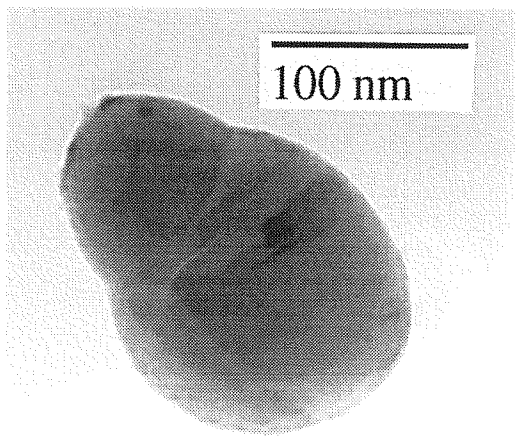

Figure 4.29: Bisphere sintered at 1300 °C for 1.6 sec.

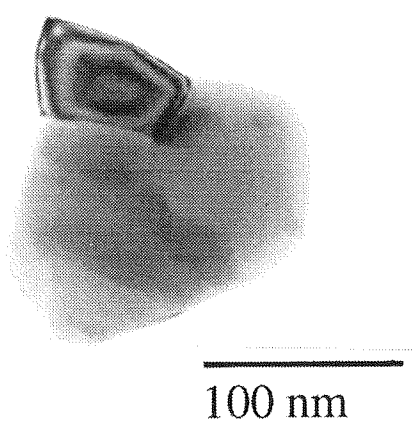

Figure 4.30: Three particles that have been sintered at 1200 °C for 11.8 sec. All three have appeared to sinter to each other simultaneously.

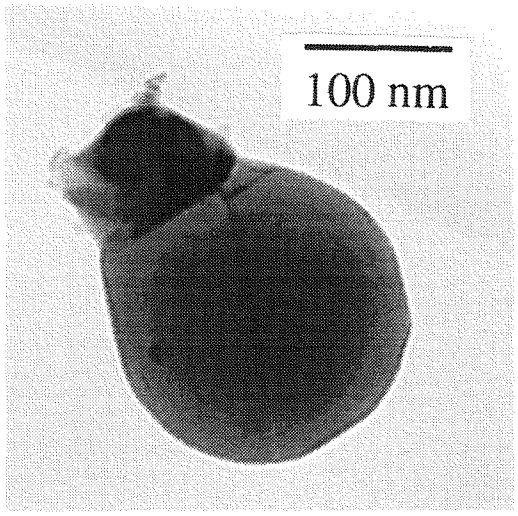

Figure 4.31: Bisphere sintered at 1200 °C for 2.89 sec showing how a large particle size mismatch sinters.

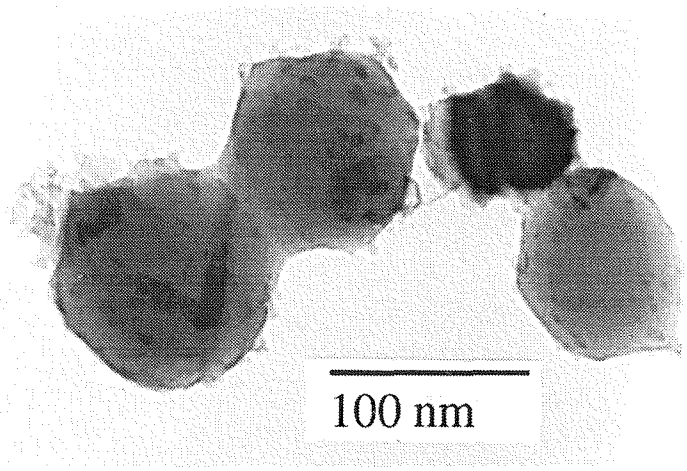

Figure 4.32: Faceting of a bisphere sintered at 1100 °C for 11.8 sec.

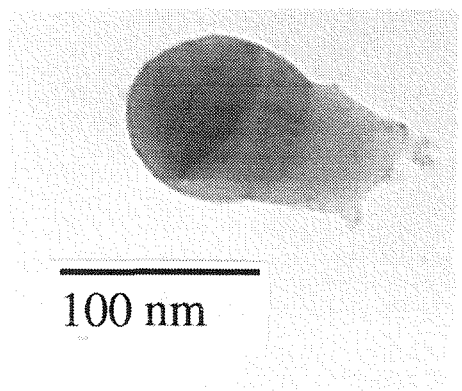

Figure 4.33: Picture of a bisphere sintered at 1200 °C for 11.8 sec in which the grain boundary appears to be moving out of the smaller particle.

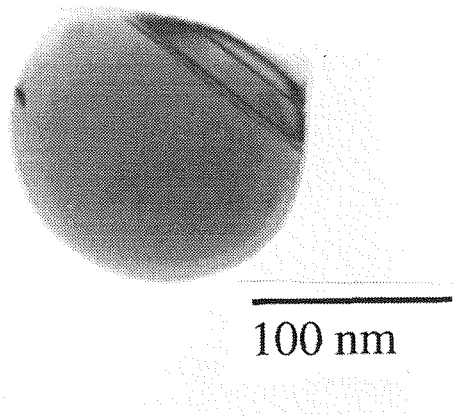

Figure 4.34: Picture of a bisphere sintered at 1300 °C for 4.6 sec in which the grain boundary appears to be moving out of the particle system.

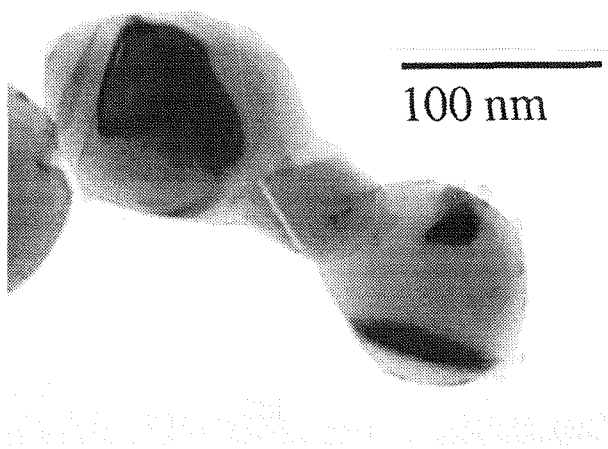

Figure 4.35: Picture of three spheres that have sintered together at 1200 °C. The grain boundaries appear to be moving through the middle particle.

Chapter 5

Structural Evolution of Model Silicon Aerosol Agglomerates Due to Sintering

5.1 Introduction

A variety of aerosol methods have been used to produce powders of ceramic materials. Oxides are produced by vapor phase oxidation of metal halides in flames and furnaces [37, 21, 22, 38, 39]. Silicon powder has been obtained by thermal decomposition of silane [59]. Powders of silicon, silicon nitride, silicon carbide, and other materials have been generated by laser induced chemical reactions of gaseous precursors [58]. Particles produced with these different methods often exhibit a common structure, i.e. they are aggregates of approximately uniformly sized primary particles. These aggregates, however, are generally undesirable in ceramic powders because they inhibit densification, leading to substantial density variations in the green compact, large voids that are major causes for failure in the final part. The ideal powder for

ceramic applications consists of spherical, non-aggregated particles with a controlled size distribution. A better understanding and, ultimately, improved control of the synthesis process is needed to produce such particles.

In the initial stage of these high temperature processes, condensible vapors accumulate until they are sufficiently supersaturated to nucleate. The fine particles thus produced then coagulate rapidly. While the particles are small, they coalesce rapidly upon coagulation. As growth continues, the time required for coalescence increases due to the increase in particle size and decrease in process temperature. In most systems, a time is eventually reached when particles only partially coalesce between coagulation events. From that time on, the particles evolve as aggregates comprised of small primary particles that are partially fused together into a ramified or fractal particle shape. This process is illustrated schematically in Fig. 5.1.

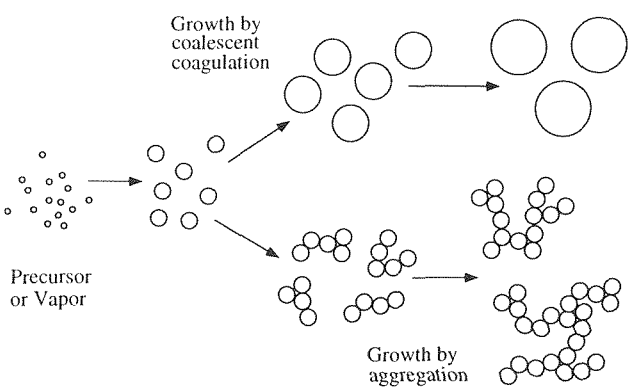

Figure 5.1: Representation of the coagulation/coalescence evolution of an aerosol population.

The equations that govern coagulation of spherical particles, i.e., those produced when coalescence is instantaneous, are well developed. This is not the case, however, when coagulation and coalescence take place on comparable time scales. A number of

models have been devised that incorporate a coalescence term into the usual aerosol population balance equations [37, 22, 68, 24]. The coalescence terms used in these models have been derived from traditional sintering theory that describes the growth of the neck between two particles. These sintering models involve assumptions that are valid only for the initial neck formation, and may not accurately describe the entire coalescence process. Furthermore, these models assume that only one transport mechanism contributes to coalescence. In reality, several transport mechanisms may simultaneously contribute to coalescence.

These models of coupled coagulation and coalescence use either the total aggregate surface area or the number and size of the primary particles as descriptors of the aggregate system [22, 68, 25, 44, 28] and track changes in these quantities as the aerosol population grows. Few touch on how the structure of the aggregate changes [25]. The difficulty in describing the aggregate structures lies in the complex nature of the particles. Even if the coalescence terms are neglected, the inclusion of a realistic description of their structure, usually involving characterization of the particles as fractals complicates the coagulation equations. Both the collision cross sections and particle diffusivities for fractal particles can differ greatly from those derived for spheres [69]. The extent to which coagulation rates change as a result of these variations is still an active subject of research.

Given these complexities and uncertainties, it is difficult to isolate the separate effects of particle form and from those due to the sintering. Model predictions frequently appear to agree with experimental observations of changes in aggregate size

with temperature [24, 26, 28]. This agreement is, however, assured by estimating the diffusivities by fitting observations in similar sintering experiments, rather than using values derived from independent measurements. It is difficult to validate the coalescence terms used in the combined coagulation/coalescence models using results from experiments in which both coalescence and coagulation are active. In particular, the initial conditions from which the extent of sintering can be measured are difficult to define at best.

With the present work, we seek to understand how sintering affects the structure of agglomerates. To that end, we have separated coagulation from coalescence by producing model agglomerates by low temperature, non-coalescent coagulation. Size-classified aggregate particles were then thermally processed while still entrained in the carrier gas, and subsequently collected for electron microscope analysis of neck growth and other structural parameters. Changes in the physical structure and aerodynamic drag of these particles has been examined. The observed neck growth was compared to predictions using a model developed elsewhere (Chapter 3) that uses a simplified, but realistic geometry to follow the contribution of different sintering mechanisms to the rate of neck growth.

5.2 Particle Mobility

The size of an aggregate particle is ambiguous because it possesses several length scales. Microscopy reveals the sizes of the primary particles that are bound together to produce much larger structures. The particle's aerodynamic characteristics and,

hence, its diffusivity and coagulation kinetics are governed by the larger structure. The aerodynamic response of aerosol particles can be probed directly by attaching charge to the particles (ideally a single elementary charge of ± e) and classifying the particles according to their electrical mobility, Z, which is defined as the ratio of the terminal migration velocity to the strength of the applied electric field, i.e.,

$$Z = \frac{U_{term}}{E}. \tag{5.1}$$

The mobility is, in turn, related to the charge on the particle and the aerodynamic resistance to motion,

$$Z = \frac{ne}{f} = \frac{F_{appl}}{U_{term}}, \tag{5.2}$$

where f is the ratio of the force acting of the particle to the terminal migration velocity. For spheres, $f = 3\pi\mu D_p/C_c$, where C_c is a slip correction factor that accounts for noncontinuum effects. No exact result exists for agglomerate particles although Rogak and Flagan [70] have shown that f is proportional to the projected area of the agglomerate.

Mobility is measured using a differential mobility analyzer (DMA). Particles entering the DMA first pass through a bipolar charger in which a ^{85}Kr source generates bipolar gas ions that attach to the particles, producing a steady-state distribution of neutral, positive and negative charges [60]. The charged aerosol then passes through a coaxial electrostatic precipitator in which they are separated according to their migration velocities in the applied electric field. The aerosol particles are transmitted

across a particle-free sheath gas that flows between the coaxial electrodes. A small fraction of the charged aerosol has the correct mobility to migrate across the gap between the two electrodes and pass through the aerosol exit slot. In the experiments that are described below, the particles were mobility classified prior to sintering. Mobility distribution measurements of the sintered particles reveal changes that are caused by the structural rearrangements. However, particle morphology cannot be deduced directly from such measurements.

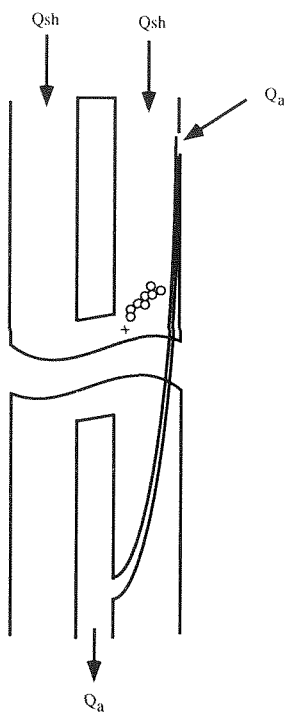

Figure 5.2: The Differential Mobility Analyzer.

Orientation effects in the DMA can affect the projected area of the charged particle. In the DMA, an elongated particle may become aligned with the direction of the motion, depending upon the location of the charges on the particles surface as illustrated in Fig. 5.2. Under the attraction of the electric field, the particle would

show a preferred orientation rather than an orientation-averages projected area. In non-conducting particles, this effect might be quite pronounced as the charge would have limited mobility on the surface.

5.3 Experimental Method

Two experimental systems that were used to generate and sinter aerosol agglomerates are illustrated in Figs. 5.3 and 5.4. Initial experiments were conducted using system A. Based upon the results and experience of these experiments, an improved system, system B, was constructed. In both systems, a precursor gas of silane is pyrolyzed to produce aggregate silicon particles which was then densified into spherical particles. These dense spheres were allowed to coagulate at ambient temperatures to produce agglomerates. A mobility classifier was used to select particles of a particular size from the aerosol stream for subsequent on-line heat treatment to examine sintering and the accompanying mobility shift.

The two systems are similar, but changes made to system B increase experimental flexibility. While system A was restricted to a single residence time, additional nitrogen could be added to the particle stream at the entrance of the sintering reactor to produce range of residence times for a single processing temperature. By sintering the agglomerates in the large reactor, temperature control was improved and residence times was increased in system B. The two smaller reactors were used to create the spherical particles.

Before any of the reactors were turned on, the entire system was evacuated to

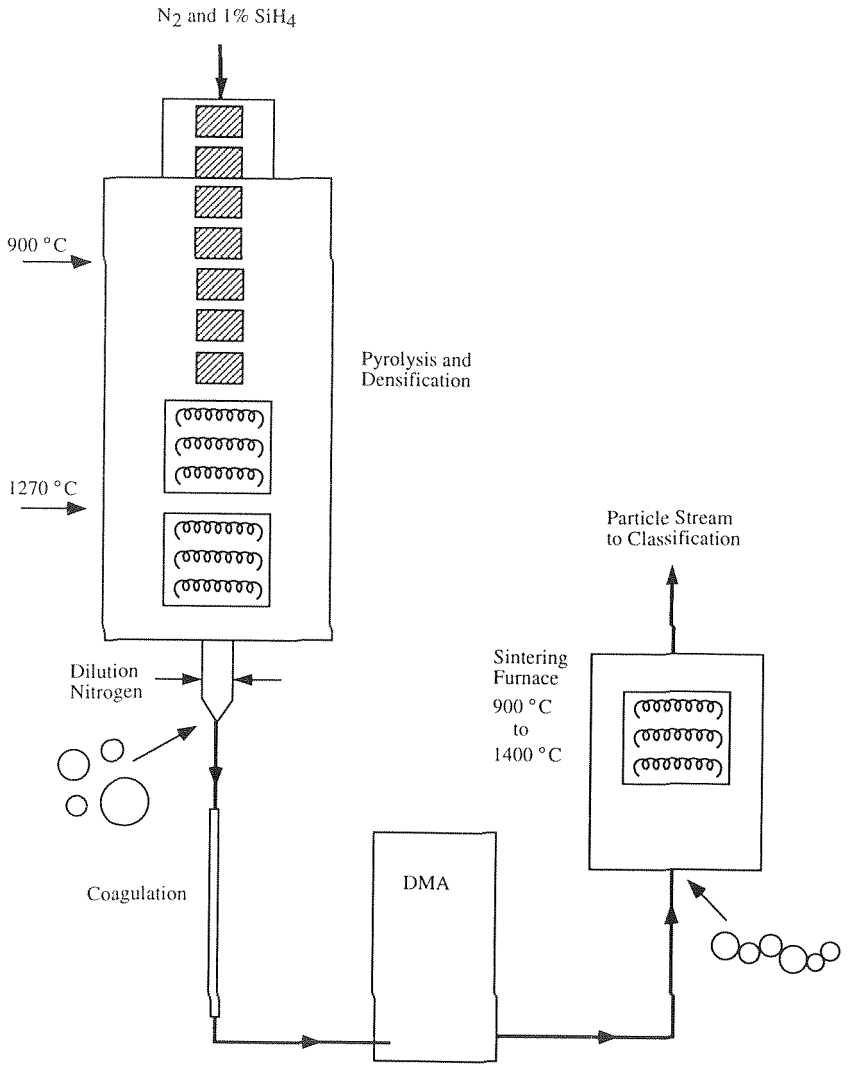

Figure 5.3: Original experimental apparatus used to produce and sinter model aerosol agglomerates.

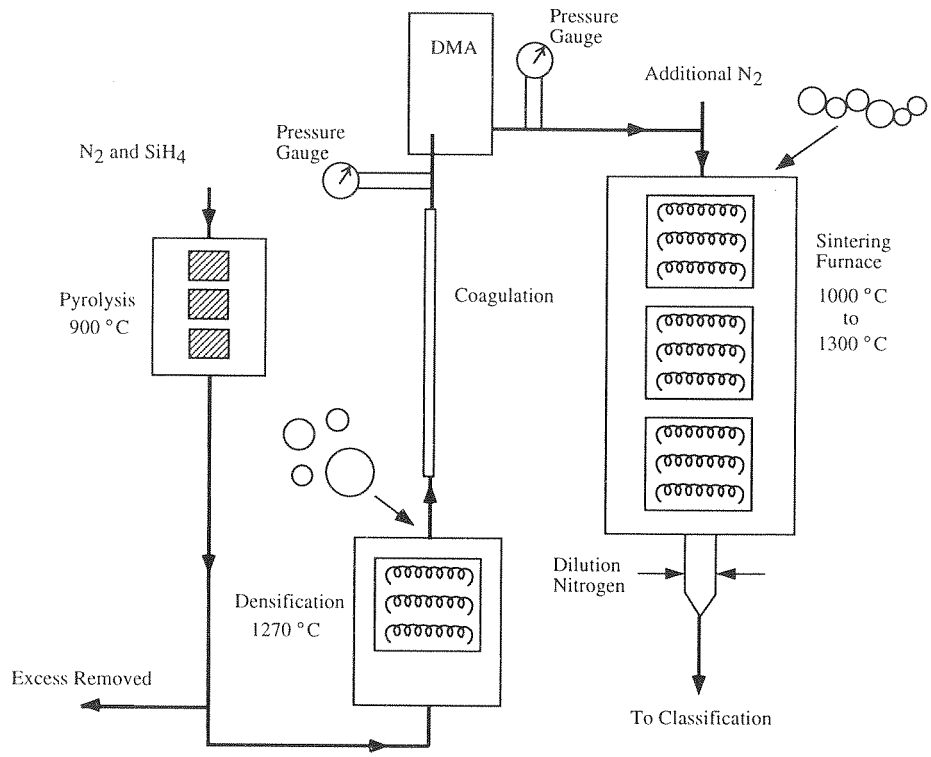

Figure 5.4: Schematic of the three furnace experimental setup used to produce and sinter model aerosol agglomerates.

approximately 14 mTorr and repeatedly purged with high-purity nitrogen (99.996%) that had been passed over hot copper shavings for additional oxygen removal. Following the purging, this high-purity nitrogen flowed continuously through the entire system. This minimized oxygen contamination during experimentation.

In system A, the first reactor, a three-zone Lindberg tube furnace (Model No. 54259-VS), was used to both form the silicon aggregates and densify them. A dilute mixture of silane in nitrogen that was prepared by mixing silane (1% in N_2, Matheson) with additional high-purity nitrogen was introduced into the top of the reactor at a flow rate of 0.79 L min^{-1}. The reactor consists of a 1.0 cm i.d., 130 cm long quartz tube, with a total heated length of 99 cm. The reactor was divided into two

heating zones. The first, 51 cm of length was heated using nichrome resistance wires heating elements to 900 °C. In this relatively cool region, silane pyrolyzed, forming particles that then agglomerated. The second region, 48 cm in length, was heated to 1270 °C using silicon carbide heating elements. As the aerosol passed into this higher temperature region, the aggregates coalesce into spheres. A number of K type and Pt/5%PtRh thermocouples attached to the surface of the quartz tube were used to monitor the temperature profile. The aerosol stream exiting the bottom of the Lindberg furnace was cooled by dilution with high-purity nitrogen that was transpired through a porous, sintered-stainless-steel tube to reduce the gas temperature and minimize particle loss due to thermophoretic deposition onto the cold walls.

System B used a combination of two smaller furnaces to produce the dense spherical particles. The first furnace consists of a 1.3 cm i.d., 51 cm long quartz tube. A 25 cm length of the tube was heated with nichrome resistance wire heating elements to a temperature of 900 °C. The dilute silane mixture was introduced into the top of this furnace at a flow rate of 3.1 L min^{-1}. This high flow rate was necessary to achieve small aggregates that were sufficiently small to produce dense particles of reasonable size.

After exiting the first reactor, 90% of the flow was exhausted, reducing flow through the later reactor zones and increasing the residence times. The resulting particle stream was introduced into the bottom of the densification reactor at a flow rate of 0.3 L min^{-1}. This reactor consists of a 1.9 cm i.d., 70 cm long alumina tube. A 23 cm length of the tube was heated using Kanthal 33 reactor heating elements

to a temperature of 1270 °C. The residence time in this furnace was approximately 13 s.

Following densification, the spherical silicon particles were allowed to coagulate in the cooled gases to produce agglomerates. In both systems, coagulation occurred in a 7/8 in i.d. stainless steel tube. In system A, the residence time was approximately 18.5 sec, and in system B, the residence time was approximately 1.5 min. In both cases, after coagulation the aerosol population consisted of agglomerates with weak or "soft" bonds between individual spheres.

After coagulation, the aerosol stream was passed through a DMA (TSI Model 3071). In system A, the sheath gas across which the particles migrate was recirculated using a diaphragm pump with 1-L reservoirs on either side to damp out pump variations. In system B, the recycled sheath flow was replaced with metered nitrogen which was immediately exhausted. The classified agglomerates were passed from the DMA to the final furnace for sintering.

In system A, the sintering reactor consists of a 1.9 cm i.d., 70 cm long alumina tube. (It was the same reactor used in system B to densify the silicon aggregates.) A 23 cm length of the tube was heated to a temperature of 1270 °C. The residence time in this furnace was approximately 2.6 s. In system B, the particles were sintered in the longer three zone Lindberg furnace. All three zones were heated with silicon carbide heating elements, giving a total heated length of 65 cm. Insulation that had been installed between the heating zones for system A was removed in order to ensure an isothermal environment. Five Pt/5% PtRh thermocouples were attached to the

surface of the quartz tube to monitor the heating profile. Residence times in this reactor varied from 1 to 10 s.

The size distribution of aerosol leaving the sintering reactor was measured using a DMA in combination with a condensation nuclei counter (CNC,TSI Model 3760) as a detector. Particles that fall within a certain mobility range are extracted from the DMA and counted with the CNC. The instrument was operated as a Scanning Electrical Mobility Spectrometer (SEMS) in which the size distribution is obtained by exponentially ramping the voltage with computer control, and monitoring the counts obtained as a function of time [61]. This allows complete size distributions to be obtained in as little as 1 min, although scans of 3 min. duration were used in the present study to minimize distortion associated with high scan rates.

To determine particle structure, samples were collected on grids using the thermophoretic sampling probe illustrated in Fig. 5.5 [62] for examination with a transmission electron microscope (TEM). The thermophoretic probe collected particles directly onto the sampling grid by heating the aerosol stream and then passing it over a TEM grid that is mounted on the end of a copper rod that was cooled by immersion of the opposite end in ice water or liquid nitrogen. Thermal diffusion of the particles in the sharp temperature gradient, a process called thermophoresis, drives particles from the hot gas onto the cold grid. The number of particles collected was controlled by adjusting the temperature gradient and collection time. The collection conditions were adjusted so that the particle coverage on the grids would be sparse, allowing for individual particles to be analyzed. Particles were collected on 400 mesh

copper grids (Ted Pella Inc.) covered with a formvar or parlodian film.

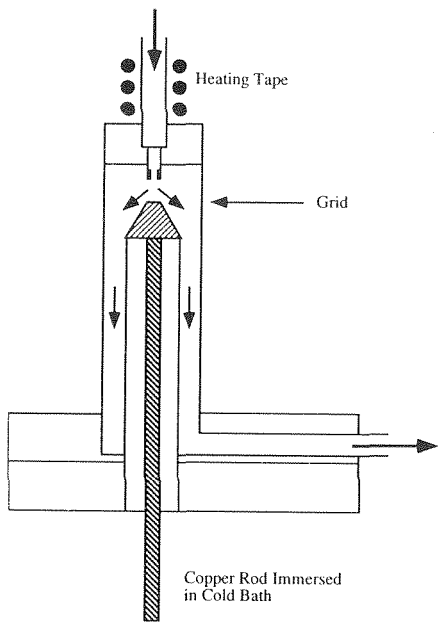

Figure 5.5: Schematic of the thermophoretic sampler used to sample particles entrained in the gas stream.

There was some difficulty collecting particles at the low number concentrations encountered in experiment B, on the order of 10^3 particles/cm^{-3}. After numerous attempts, a few very sparse depositions of particles were collected for a limited number of residence times at 1100 °C. Attempts at lengthening sampling times and increasing the temperature gradient did not result in any deposited particles. There appears to be a concentration gradient below which the current sampling system does not collect efficiently. Except for those mentioned above, we were unable to obtain samples at all other experimental conditions.

5.4 Image Analysis

The TEM (Model 210, Phillips Electronic Instruments) magnifications were determined to within 5 percent using a precision grating. During the microscope session, particles were selected and photographed randomly in order to minimize operator bias.

The TEM negatives were printed at approximately 7X magnification. Neck and particle sizes resulting from experiment A were measured directly from the print. The results from experiment B were scanned (HP ScanJet IIcx) into a microcomputer (Macintosh Quadra 800) using 100 dots per inch resolution. The background was removed using an image processing program (Adobe Illustrator, v3.0) manually because shading differences in the prints made automatic background removal difficult. During this procedure, the extraneous surface features of the particles that weren't related to neck growth were removed. In addition, the component particles in each aggregate were separated at the adjoining neck so individual particles could be measured.

After background removal, the particles were imported into an image analysis program. (NIH Image, v1.52) The particle images were calibrated and thresholded. The particle perimeter, and major and minor lengths were measured, as were the projected area and the major and minor ellipse axes fitting each of the component particles. Using these values, the particle volume was inferred from the two-dimensional images.

5.5 Results

Figure 5.6 shows a representative photo of the type of results of the experiments from system A. After sintering agglomerates for approximately 2.6 sec in this system, the individual primary particles remained spherical, but some neck growth is discernible. Figure 5.7 shows an agglomerate that has been sintered at 1400 °C, with some necks indicated by arrows. Even at this high temperature there was no discernible shift in the mobility measurements of the particle size distribution of the particles.

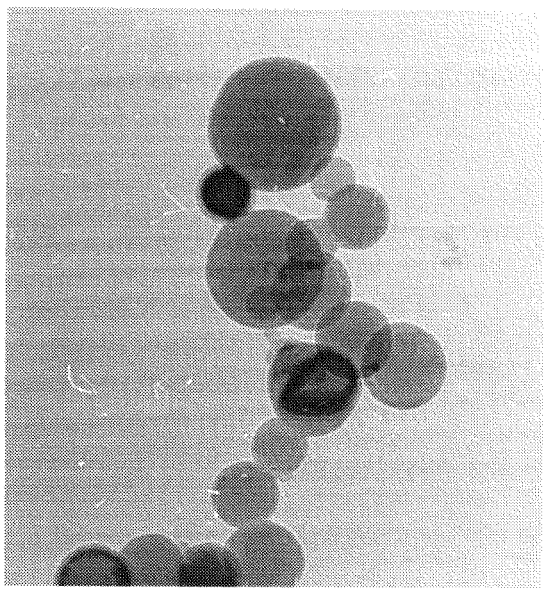

Figure 5.6: Picture of a model agglomerate that has been sintered for 2.6 sec at 1400°C.

Neck and particle sizes were measured directly from the photos with care being taken to choose necks between particles that appeared to be lying flat. Because the particles were partially transparent, a dark region at the neck of overlapping particles was discernible. Figure 5.8 summarizes the sizes of the necks that were measured at 900 °C, 1200 °C and 1400°C. Neck growth is presented as the neck size, x_n, divided

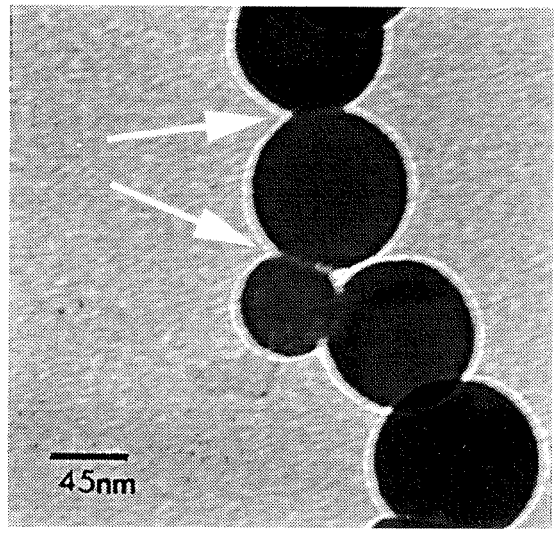

Figure 5.7: Picture of a model agglomerate that has been sintered for 2.6 sec at 1400°C. Measurable necks are indicated by arrows.

by the particle radius, a. Because the sintered neck was usually between particles of differing sizes, two values are presented for each neck measured. For all temperatures, neck growth decreases with increasing particle size. The slope of this decrease seems to increase with increasing temperature. Figure 5.9 shows how the neck growth varies with the ratio between the two particle sizes for 900 °C, 1200 °C and 1400°C, respectively. In general, neck growth based upon the smaller radius shows a marked increase, while growth based upon the larger radius seems to decrease slightly.

Figure 5.10 shows the average neck growth at each temperature based upon the two particle radii. Neck growth increases with increasing sintering temperature. To directly compare results to the model, neck growth results for particles with a ratio of 1.0 to 1.1 (two particles with approximately the same size) for the temperatures 1200 °C and 1400 °C are presented separately in Fig. 5.11. Figure 5.12 compares

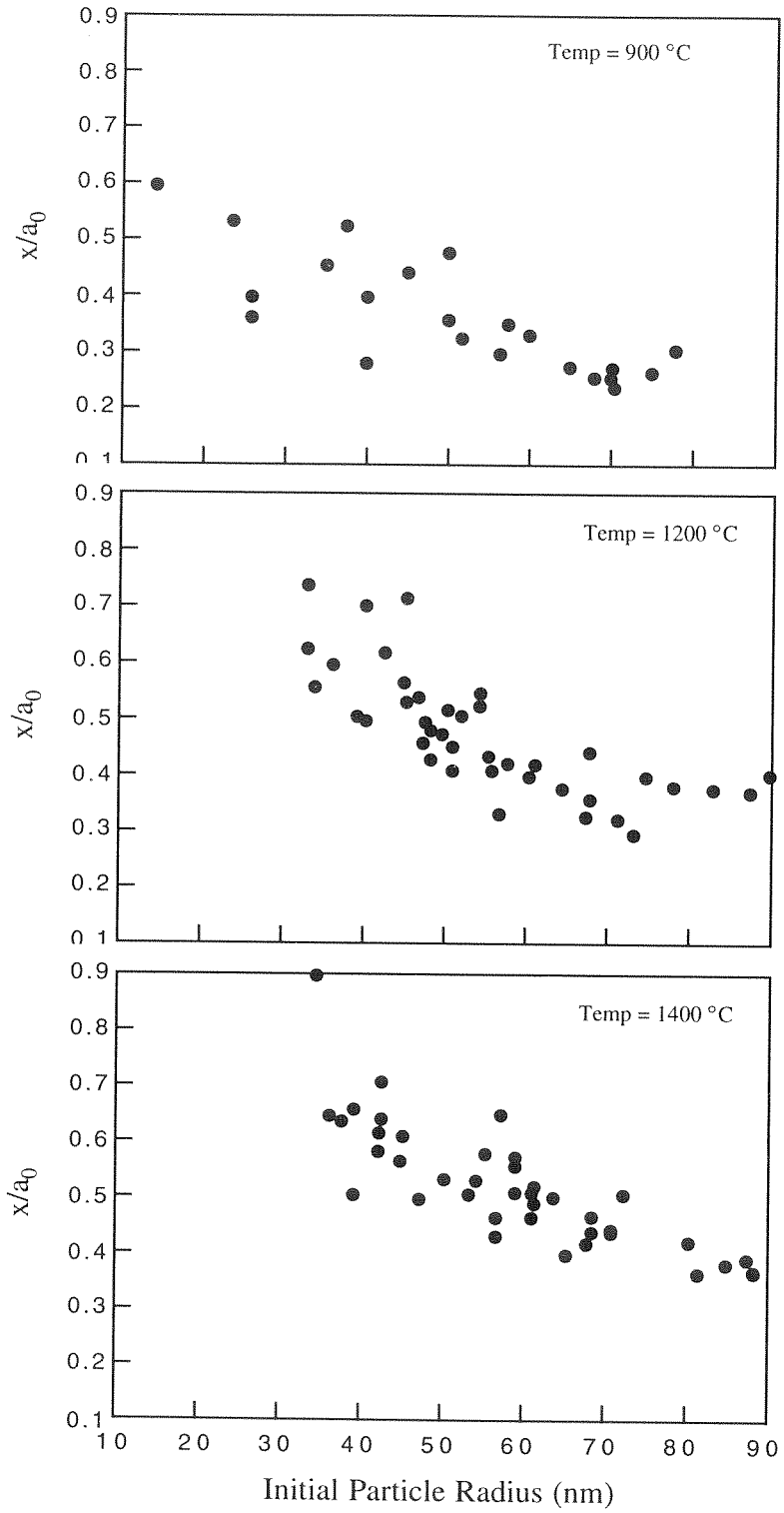

Figure 5.8: Measurements of neck growth as a function of particle size for 900 °C, 1200°C and 1400°C, respectively. The empty circles are nondimensional neck growth (x/a) based upon the smaller particle radius, and the filled circles are based upon the larger radius.

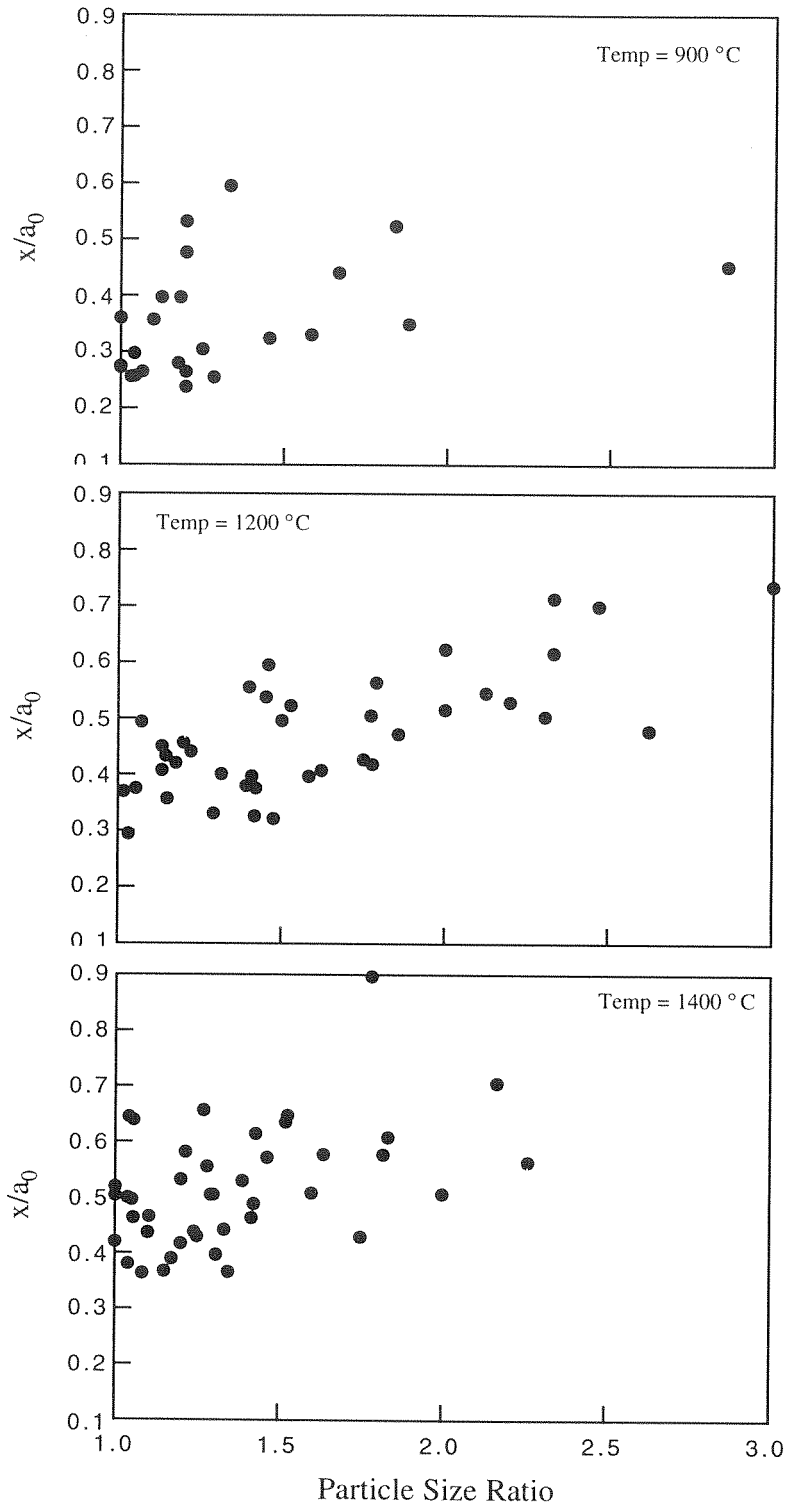

Figure 5.9: Measurements of neck growth as a function of particle size ratio for 900 °C, 1200°C and 1400°C, respectively. The empty circles are nondimensional neck growth (x/a) based upon the smaller particle radius, and the filled circles are based upon the larger radius.

model predictions to average neck growth for the average particle size. The model predictions based on published diffusivities for silicon obviously severely underestimate the time required to achieve the observed neck growth.

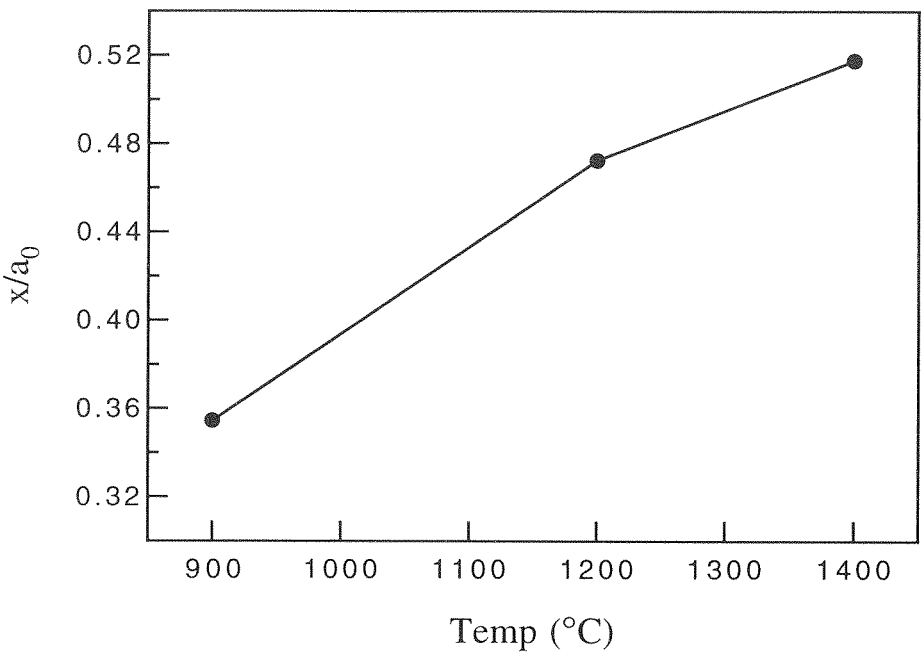

Figure 5.10: Average neck growth for 900 °C, 1200 °C and 1400 °C, respectively.

The agglomerates resulting from system B show remarkably different structure. Fig. 5.13 shows a representative agglomerate that was sintered at 1100 °C for 4 s. Although the processing times do not differ significantly, sintering has progressed much further in these agglomerates. A key difference between the two systems is the elimination of the sheath gas recycle pump from system A. We suspect that a small amount of oxygen leaked into the recirculation system. Surface oxidation of the silicon particles would then produce a thin layer of silicon that would prevent surface diffusion. To test this hypothesis, model calculations were performed from which surface diffusion was removed as a contributing mechanism. Without surface

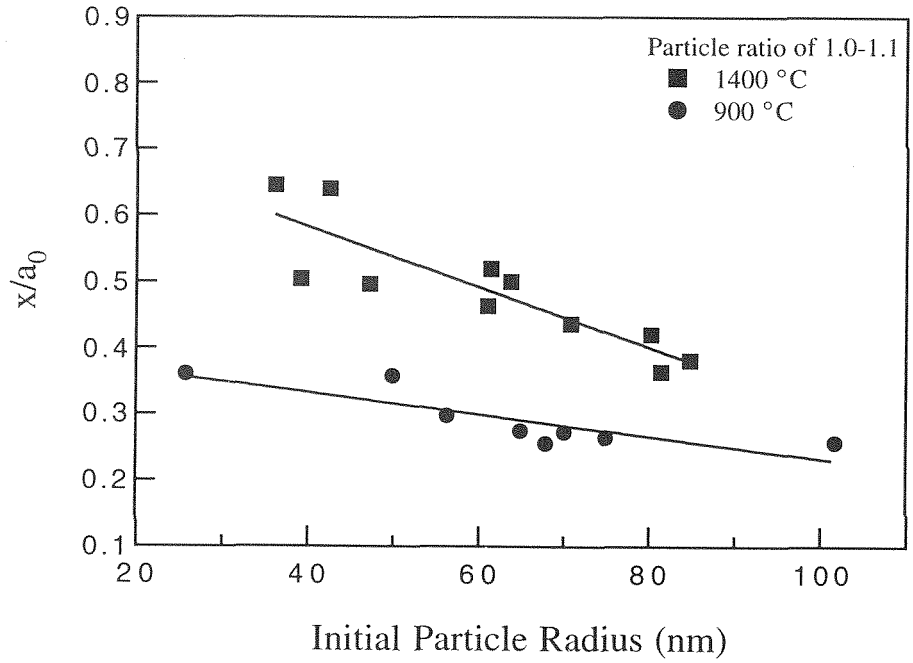

Figure 5.11: Neck growth results for particles of approximately the same size (particle size ratio of 1 to 1.1) for 1200 °C and 1400 °C, respectively.

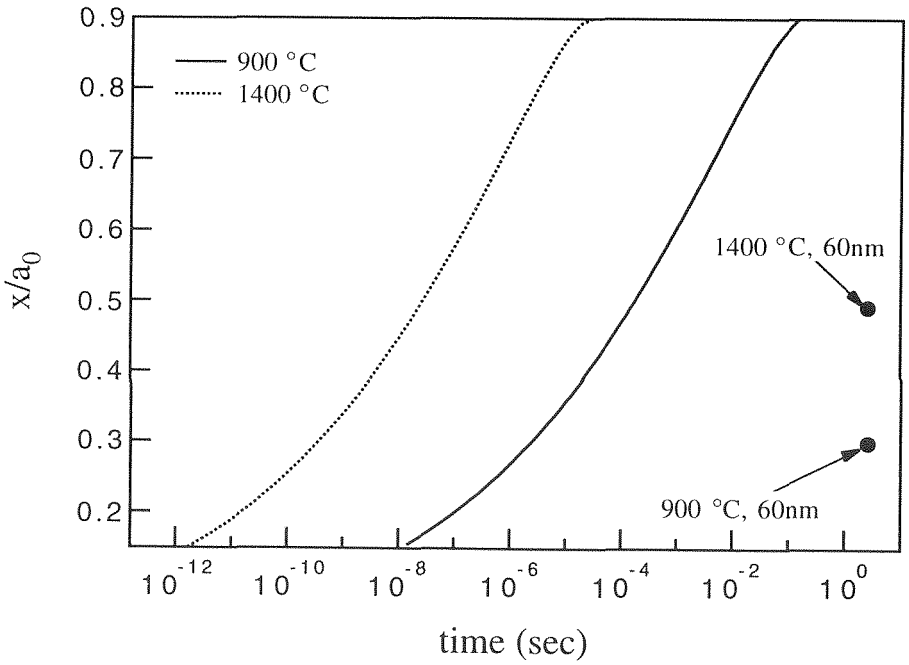

Figure 5.12: Present model results compared to averaged neck growth data for equal sized particles sintered at 900 °C and 1400 °C, respectively.

diffusion, the time required for sintering increases tremendously, as seen in Fig. 5.14, and the agreement between theory and experiment improves markedly.

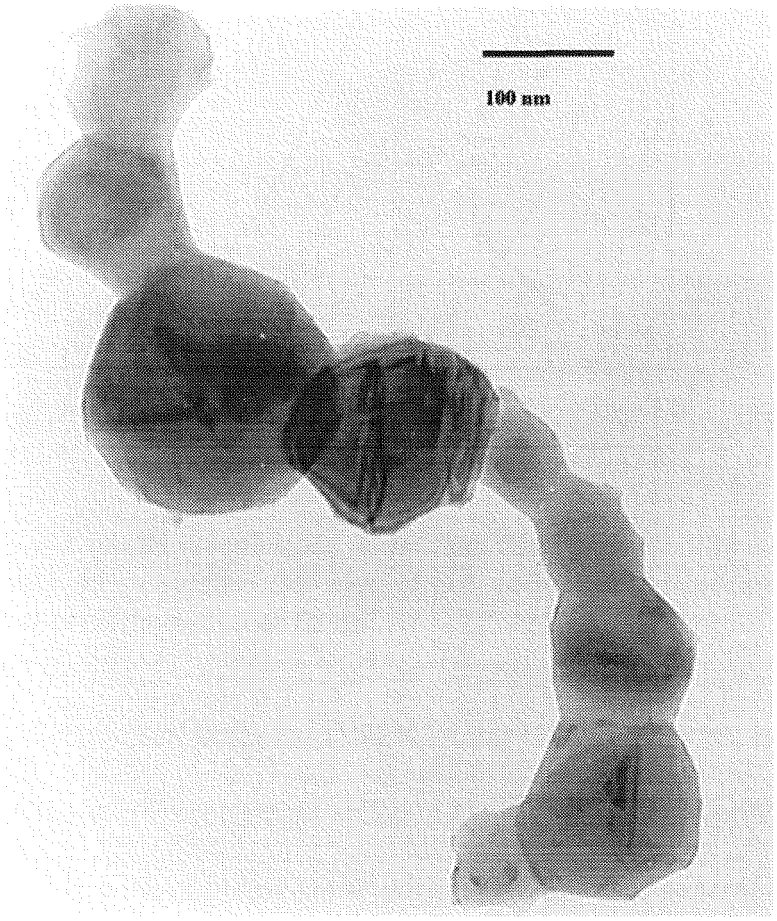

Figure 5.13: Picture of a model agglomerate that has been sintered for 4 s at 1100°C in setup B.

Once the source of oxygen was identified and removed from the system, the agglomerate mobility shifted significantly upon sintering. Beginning with a mobility size of 200 nm, no shift in the distribution was observed at 1050 °C, as seen in Fig. 5.15. When the temperature was raised slightly to 1075 °C, there was a detectable mobility shift as shown in Fig. 5.16. The mobility shift becomes more pronounced with increasing sintering temperature, and the distributions broaden. Figures 5.17, 5.18,

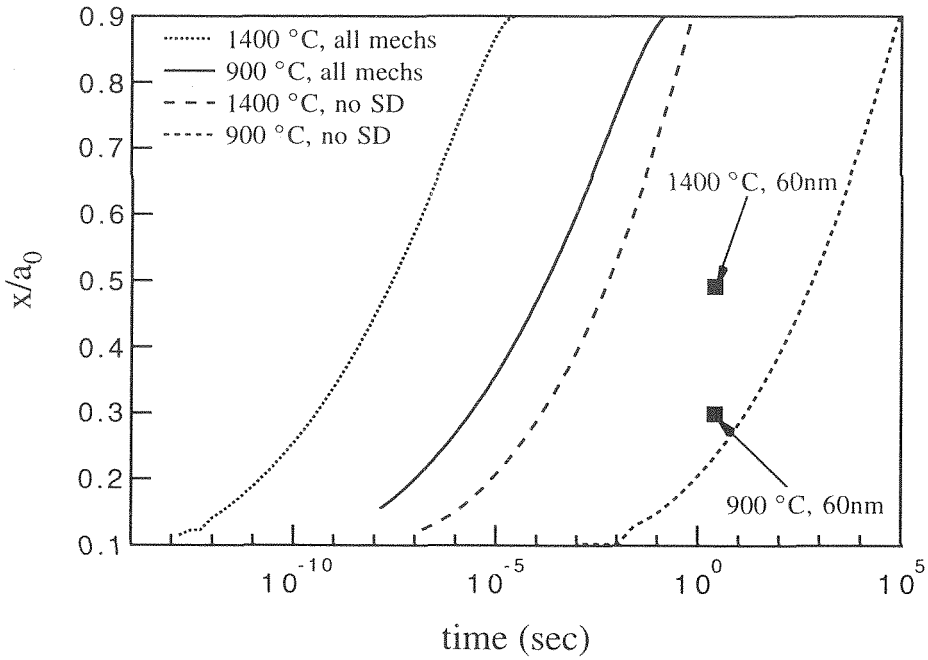

Figure 5.14: Results of model calculations show that time predicted for neck growth increases significantly when surface diffusion is not active. Calculations were performed for an initial particle radius of 50 nm.

and 5.19 show size distribution shifts for 1100 °C, 1150 °C and 1200 °C, respectively.

Figure 5.20 summarizes the observed shifts in the mobility corresponding to the peak in the distribution with sintering time. Although there is a general decrease in the mobility diameter with sintering temperature and time, results for 1075 °C and 1100 °C temperatures show an apparent increase in the mobility size after some sintering has occurred, at 4 s for 1075 °C and 6 s for 1100 °C. This apparent increase can be explained by a bending of the chain-like agglomerates that align with the electric field during the initial classification. Unfortunately, sampling difficulties precluded direct observation of those particles that would be needed to confirm this hypothesis.

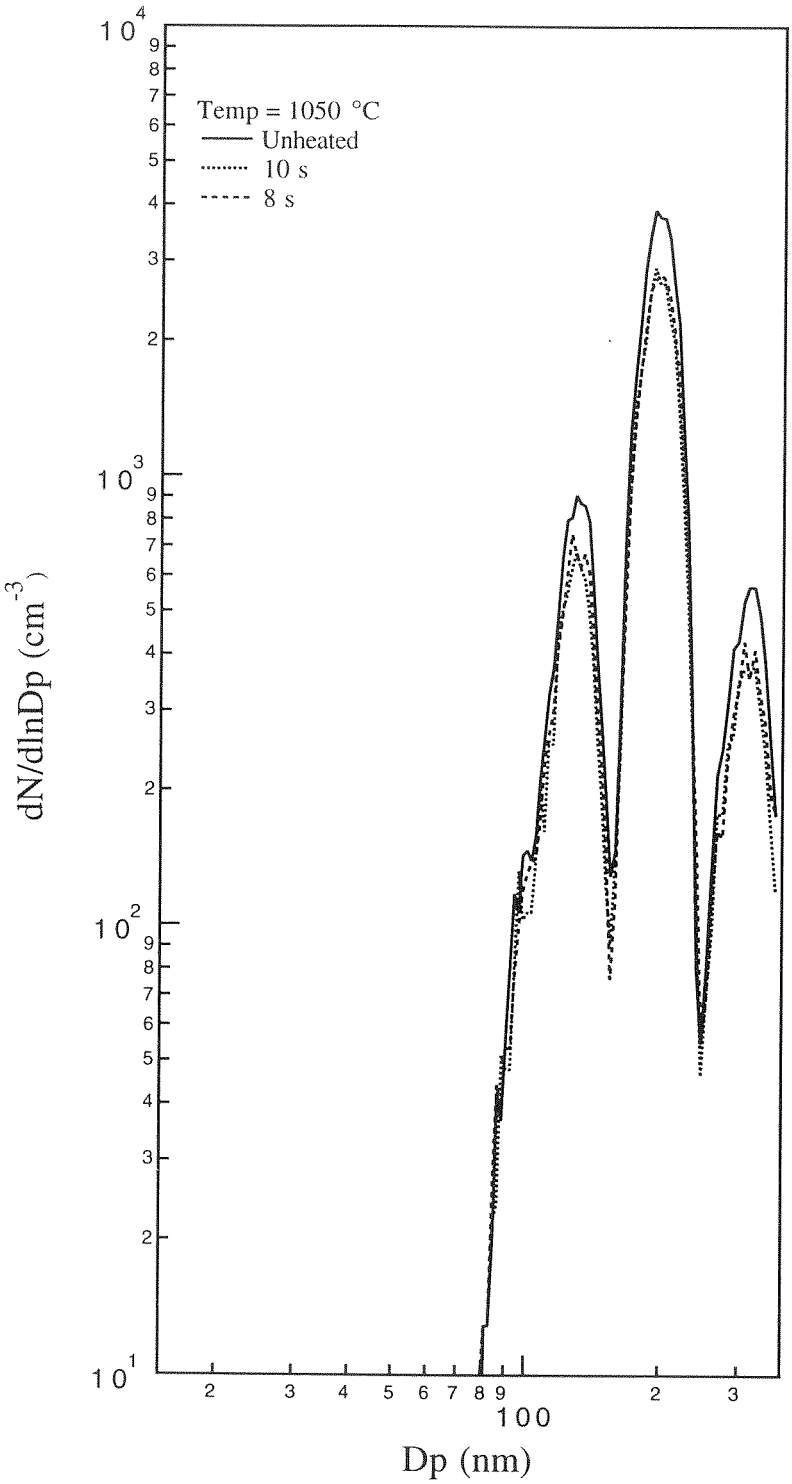

Figure 5.15: Size distributions for a 200 nm classified aerosol heated at 1050 °C for different times.

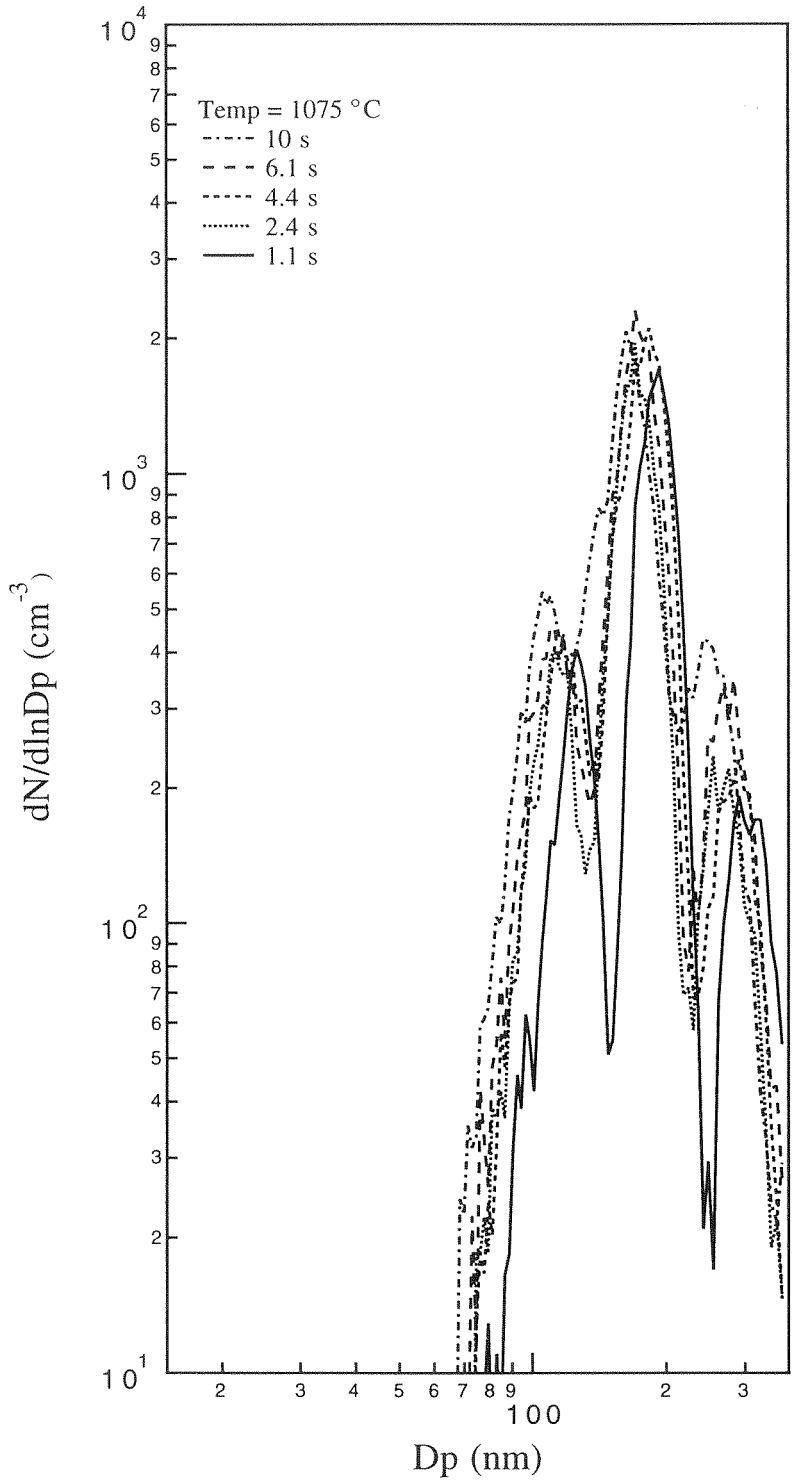

Figure 5.16: Size distributions for a 200 nm classified aerosol heated at 1075 °C for different times.

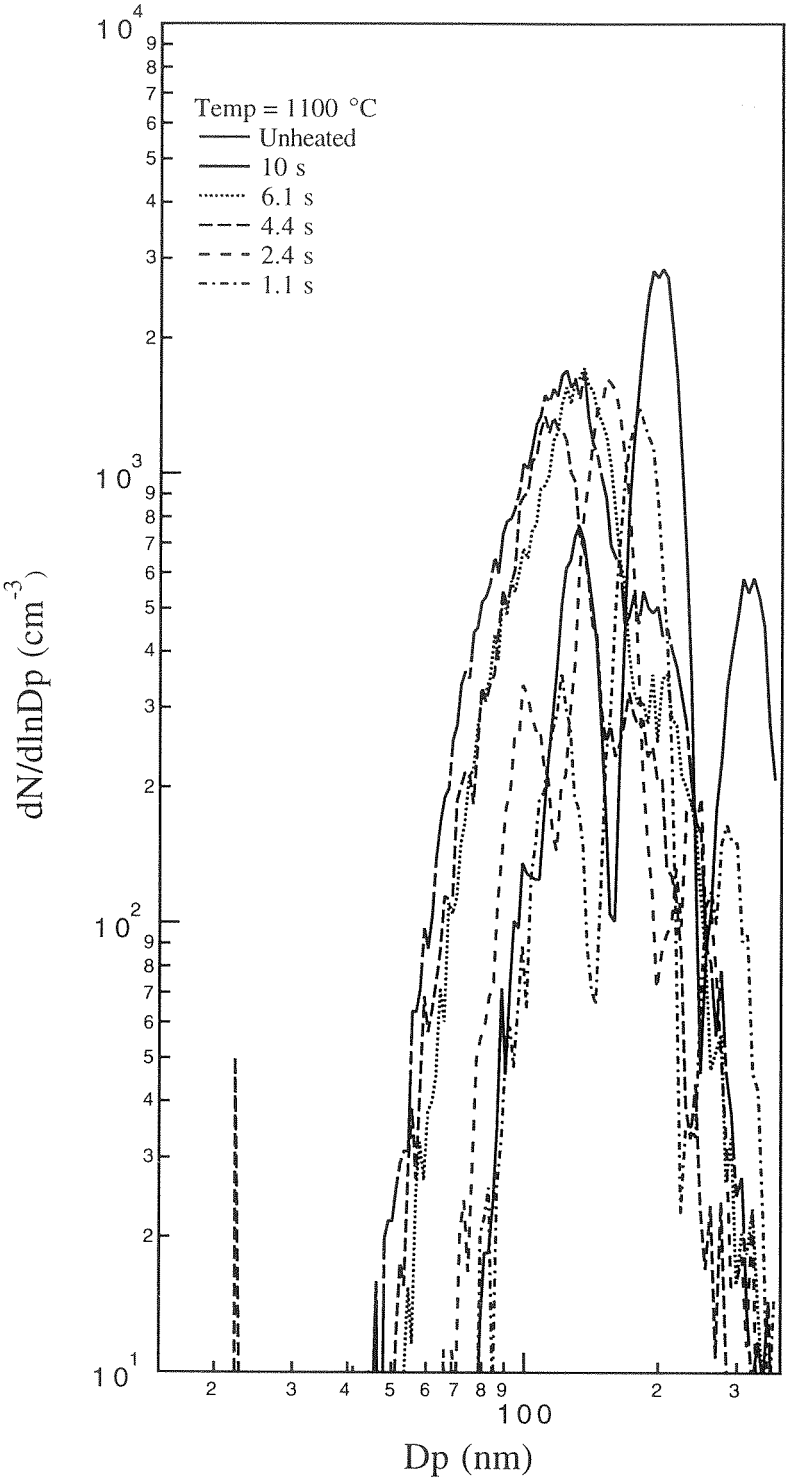

Figure 5.17: Size distributions for a 200 nm classified aerosol heated at 1100 °C for different times.

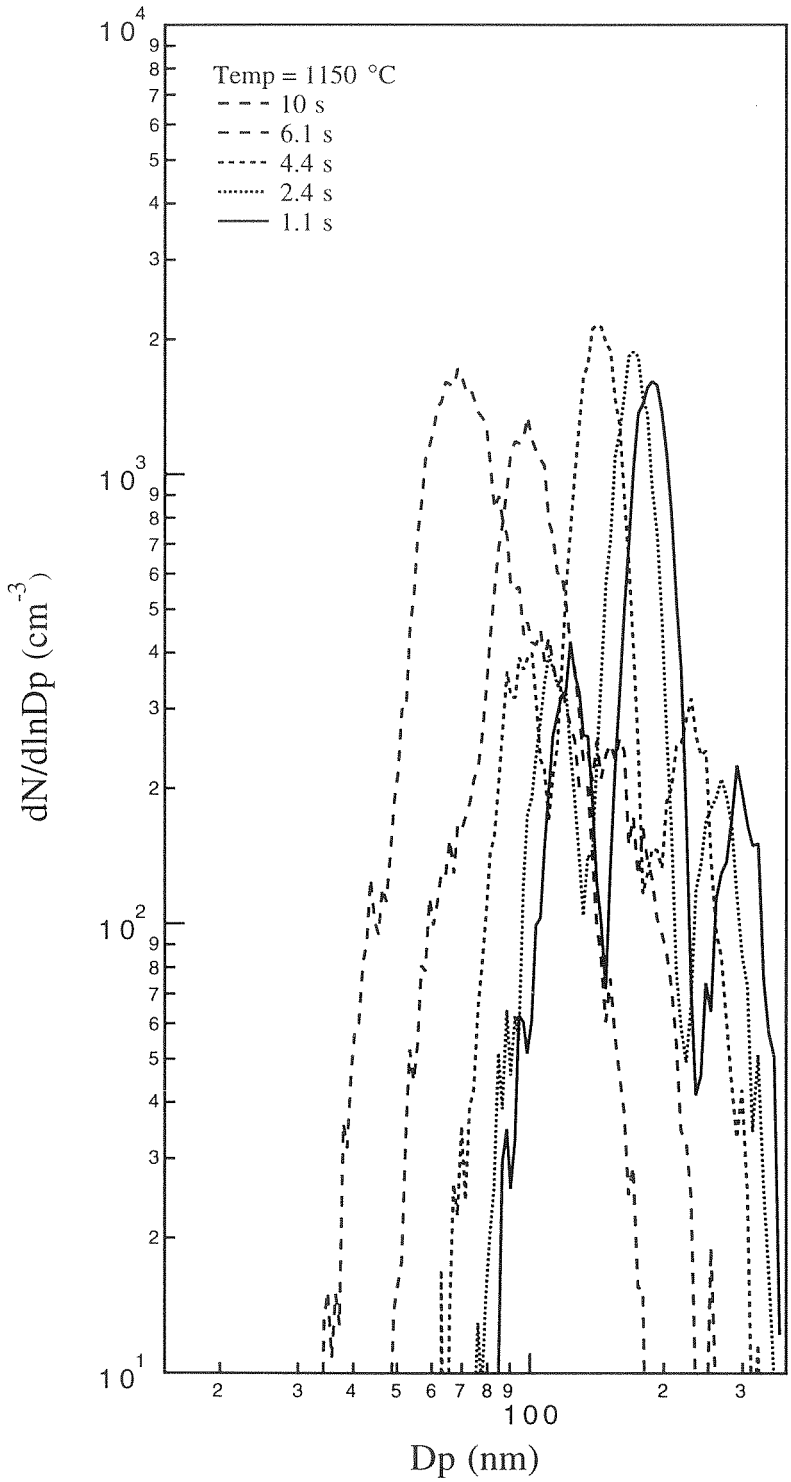

Figure 5.18: Size distributions for a 200 nm classified aerosol heated at 1150 °C for different times.

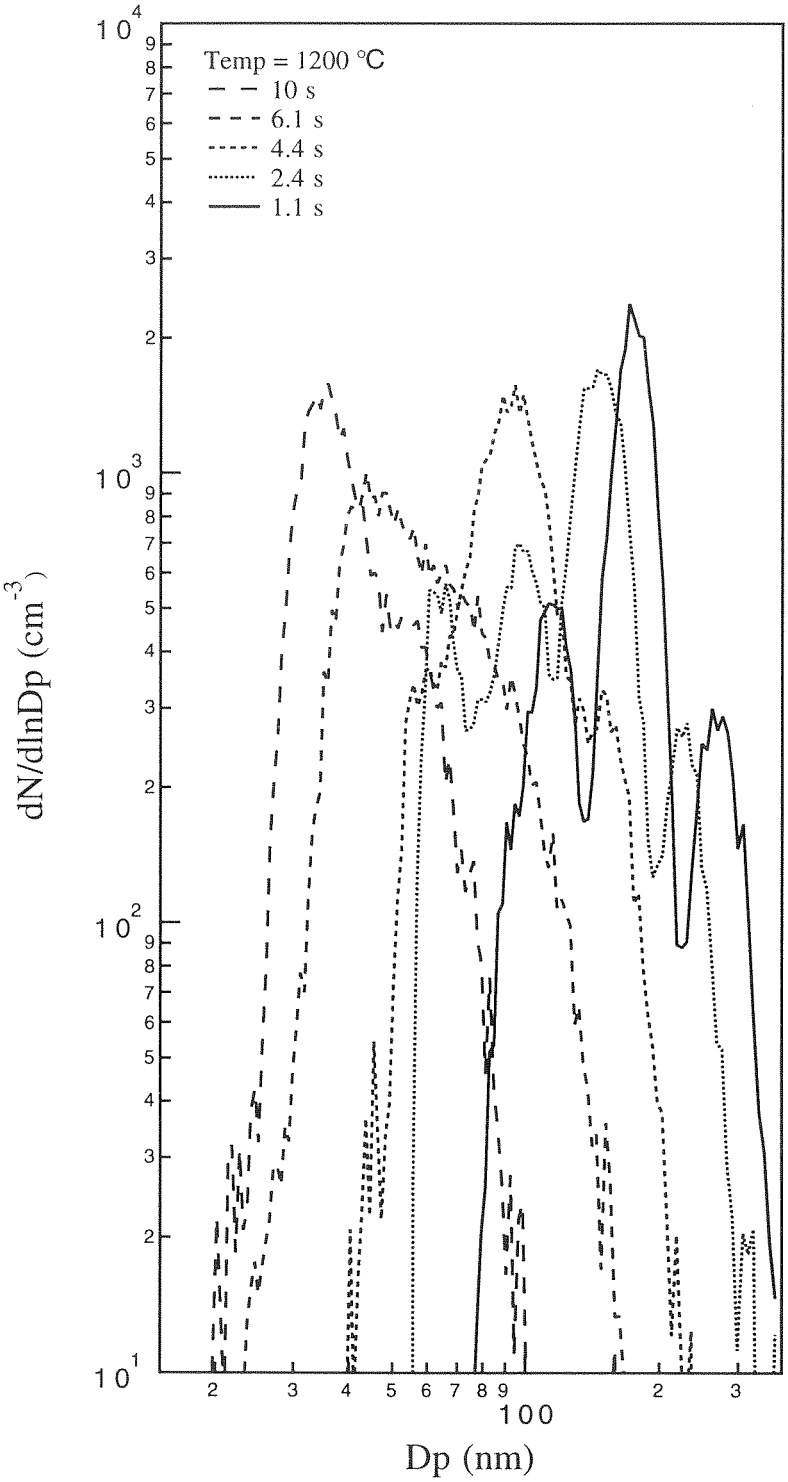

Figure 5.19: Size distributions for a 200 nm classified aerosol heated at 1200 °C for different times.

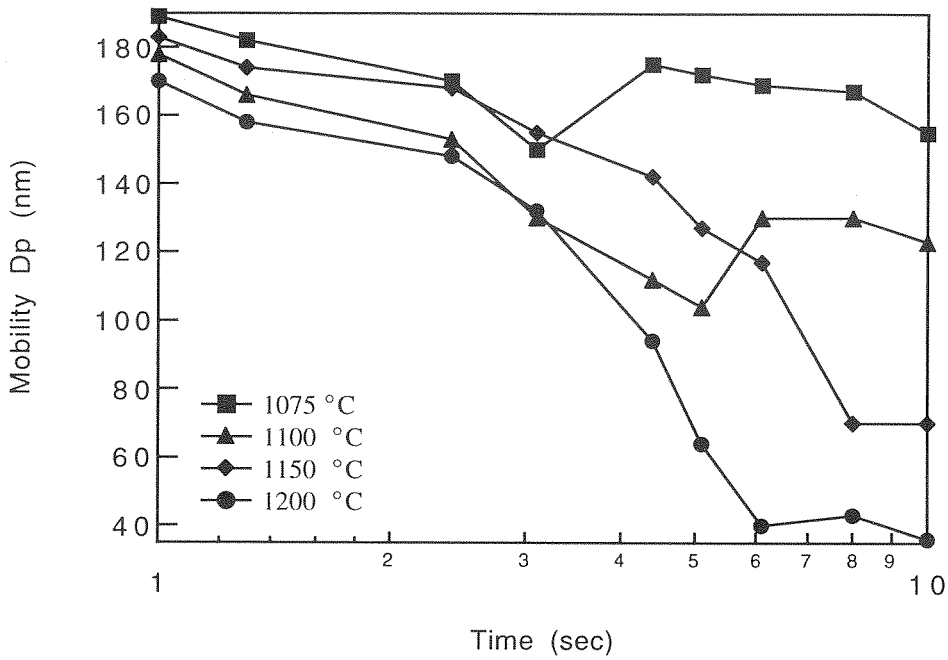

Figure 5.20: Agglomerate mobility diameter as a function of heating time for 1075 °C, 1100 °C, 1150 °C and 1200 °C.

5.6 Discussion

5.6.1 Sintering Mechanisms for Silicon

A number of condensed phase transport mechanisms contribute to the coalescence of agglomerates. The driving force for coalescence is the excess free energy of the aggregate. Variations in local surface curvature produces gradients in local vapor pressure, stress, and chemical potential, causing material to migrate into the neck region that joins two primary particles. Mechanisms that contribute to sintering include: diffusion through the particle volume, grain boundary, or surface, transport through the vapor phase, and viscous flow. The contribution of any of these mechanisms depends upon the material properties and the environment in which sintering takes place.

The sinterability of silicon was first studied by Greskovich and Rosolowski [63]. Their experiments showed very little densification and significant weight loss during sintering. Based upon their experiments, they concluded that evaporation & condensation was the predominant mechanisms contributing to the sintering of silicon. Subsequent studies supported this assertion. Shaw and Heuer [65] observed weight loss that was due, they suggested, to vapor-phase transport dominated by Si-O. Möller and Welsch [66] concluded from measurements of the activation energy for densification that a solid-state diffusion process dominates densification, but that vapor-phase transport was also evident. They observed no apparent sintering occurred below 1100 °C. All of these investigators used powder that had been exposed to air prior to sintering, and was assumed to have an oxide layer on the particle surface.

In the meantime, measurements of the surface diffusivity of silicon [51] suggested that it should be the dominant sintering mechanism. This discrepancy between experimental observations and the measured diffusivity was explained by Coblenz [67]. who studied the sintering of silicon after the oxide layer had been removed. He concluded that the oxide layers that develop rapidly when silicon is exposed to air inhibit surface diffusion and allow competing sintering mechanisms to dominate. Model predictions and experiments performed by the present authors on bispheres of silicon particles (Chapter 4) further support this assertion.

Sintering experiments performed in system A exposed the agglomerates to oxygen due to a small leak in the sheath gas recycle system in the DMA, allowing a direct comparison of sintering with and without a surface oxide layer. The oxide layer slowed

sintering below that observed in the oxygen-free experiments (system B) or predicted taking all sintering mechanisms into account. Model calculations performed with surface diffusion removed as a contributing mechanism yielded much better agreement between predictions and observed neck growth. The model predictions have been used to examine the relative importance of the different sintering mechanisms in this case. As shown in Fig. 5.21, these results suggest that, in the absence of surface diffusion, grain boundary diffusion dominates as Coblenz [67] predicted.

5.6.2 Variation in Mobility due to Sintering

A decrease in the mobility diameter is expected as the agglomerate sinters. As the agglomerate coalesces, its surface area and average projected area decrease and it approaches a more spherical shape. The agglomerates produced in system B had an average of 7 primary particles of mean diameter 70 nm. When fully densified, these particles be produce spheres of approximately 130 nm. In some cases, however, the measured mobility diameters were much smaller that expected, i.e., than that of a sphere of equivalent volume. Orientation of the agglomerates in the DMA could account for this anomalous behavior. The as-produced agglomerates were long chain-like structures. In some cases, the sintered aggregates appear rod-like. A charge attached close to one end might align such a particle with the electric field in the DMA reducing the projected area nearly to the primary particle area. In such an extreme case, the projected area of a rod-like aggregate such as that shown if Fig. 5.23 could be as small as 60 nm in spite of substantial neck growth.

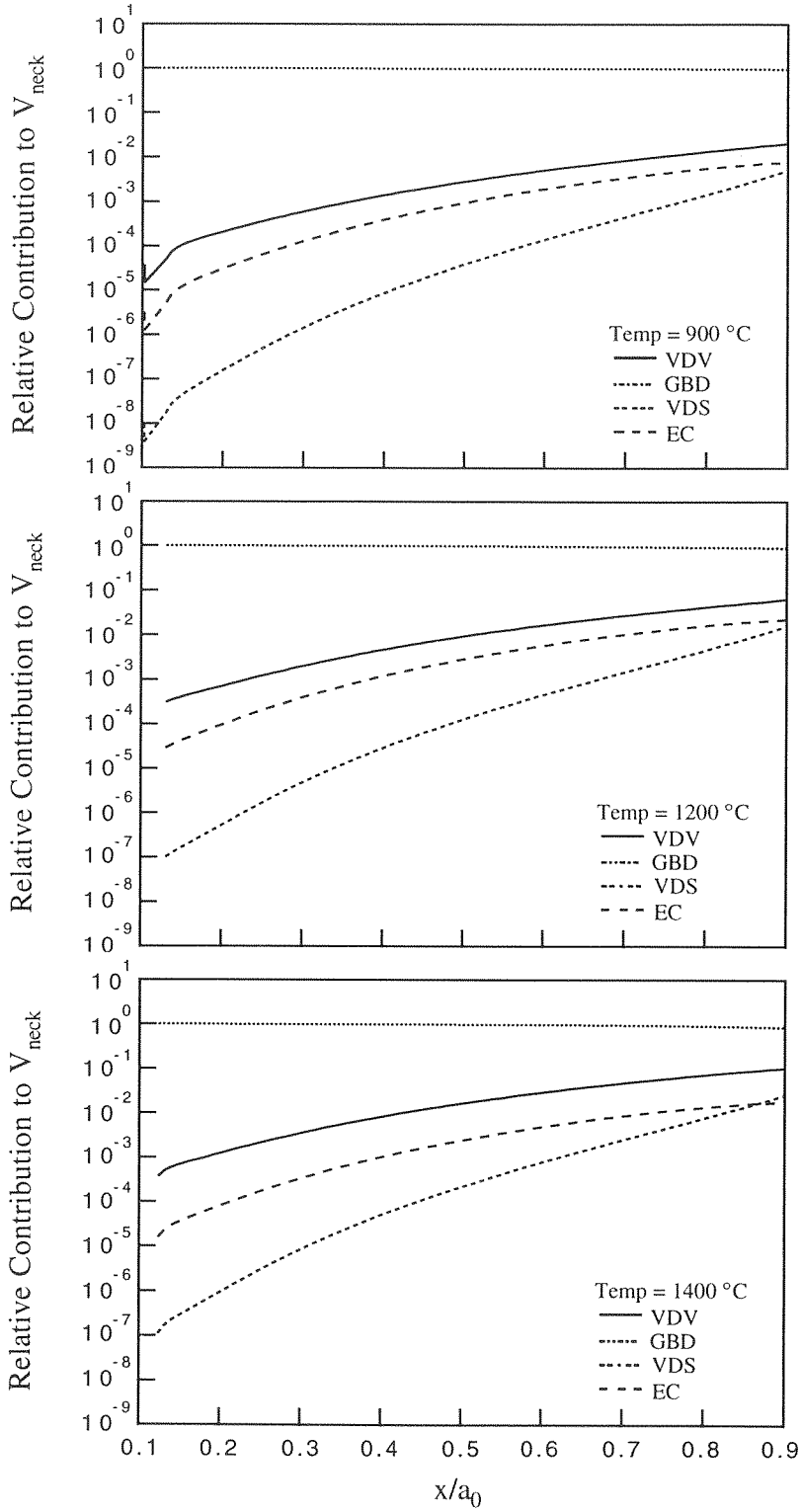

Figure 5.21: Contribution of each sintering mechanisms for 900 °C, 1200°C and 1400°C, respectively. Model results are calculated with the contribution from surface diffusion removed.

For agglomerates sintered at 1075 °C and 1100 °C, the mobility size shows an apparent increase after some sintering has occurred. This apparent size increase can be explained by the bending of the aggregates as they sinter. During sintering, the individual primary particles may "roll around" on their surfaces until a preferred grain boundary orientation is achieved. Evidence that this can occur was presented by Bonevich and Marks [71]. They produced long chains of ultrafine alumina particles with a mean radius of 20 to 30 nm by arc discharge of aluminum. In larger aggregates, they found that surface diffusion was sufficiently fast as to "lock-in" initial contact orientation before significant neck growth occurred. All primary particles showed significant faceting. However, particles that appeared more spherical did appear to rotate to a preferred grain boundary orientation. The sintered particles in the present study do not show the degree of faceting seen in Bonevich and Marks and thus may reorient during sintering, as illustrated in Fig. 5.22.

Particles collected at 1100 °C that suggest possible reorientation are shown in Figs. 5.24 through 5.26. The presence of well-defined, consistent dihedral angles within each aggregate, as seen in Fig. 5.24, supports the hypothesis that particles do rotate to preferred orientations. This reorientation could increase the apparent particle mobility size, i.e. the particle shown in Fig. 5.25 presents a larger projected area than a straighter agglomerate with an equal number of primary particles. Even a small bend, like that in the particle shown in Fig. 5.26, would increase the projected area.

The mobility diameters of agglomerates sintered at 1150°C and 1200°C decreases

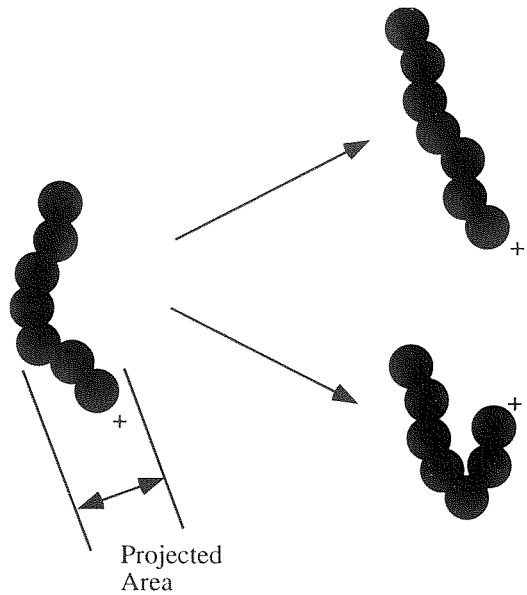

Figure 5.22: Schematic of how the projected area of an agglomerate may change due to individual primary particles rotating to a preferred grain boundary orientation.

below that values that can reasonably be expected even for completely straight aggregates, possibly due to vaporization from the particle surface. As the particles exit the furnace, this vapor will nucleate to produce its own aerosol population of small agglomerates. The size distributions resulting from these two phenomena may overlap, making it difficult to resolve what is occurring from the size distribution without micrographs. The dramatic decrease in particle size during sintering at 1150°C and 1200°C (Figs. 5.18 and 5.19 at longer residence times) may also result from vaporization. Unfortunately, we were unable to collect samples at these temperatures, so these conclusions cannot be verified through microscopy.

5.7 Conclusions

Powders produced by synthesis from vapor phase precursors usually evolve as aggregates. Efforts to incorporate a coalescence term into the aerosol population balance equations, have focussed on predicting the evolution of primary particle size or total aggregate surface area. Few studies have addressed the way that coalescence changes that structure or mobility of the particle. Neither has any direct validation of these models been reported, even though the mobility diameter is the most widely measured parameter of a coalescing aerosol.

This paper has reported on controlled experimental investigations of the structural evolution of model agglomerate particles. Aggregate particle densification studies have been performed using mobility classified particles produced by low temperature, non-coalescent coagulation. The particles were heat treated while still entrained in the gas phase. The change in particle mobility was measured as a function of processing time and temperature. Some particles were collected for TEM analysis of neck growth and other structural parameters.

Agglomerates that had been exposed to a small amount of oxygen showed little sintering and no detectable mobility diameter decrease. Neck growth measurements showed that sintering increased with increasing temperature, decreasing particle size, and increasing particle size ratio. Agglomerates that were exposed to oxygen sintered much more slowly than those that were sintered without oxide contamination. Using a previously developed sintering model, we have been able to predict this dramatic change in sintering rate by removing surface diffusion as an active mechanism. This

suggests that surface diffusion is the primary mechanisms for sintering in silicon.

The agglomerates that were sintered without oxygen exposure showed significant changes in their mobility diameter during sintering. As the agglomerates sintered, their mobility diameter decreased. This decrease, however, seems to be related to orientation effects in the DMA rather than significant densification. Some temperatures showed an apparent mobility size increase. It is postulated that this is due to the rotation of individual particles to preferred grain boundary orientations. This rotation would increase the projected area of the particle and lead to an increase in aggregate mobility.

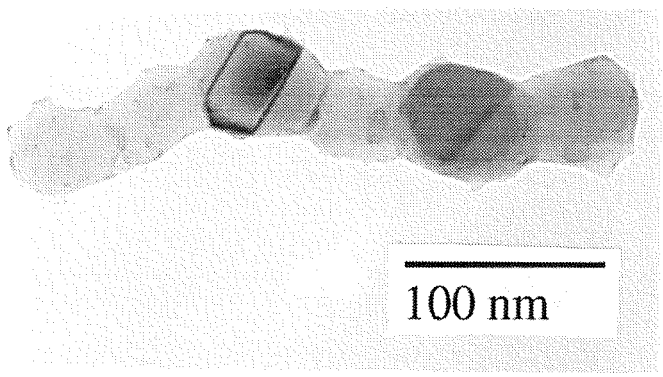

Figure 5.23: Picture of an agglomerate sintered at 1100°C that shows an elongated or rod-like structure.

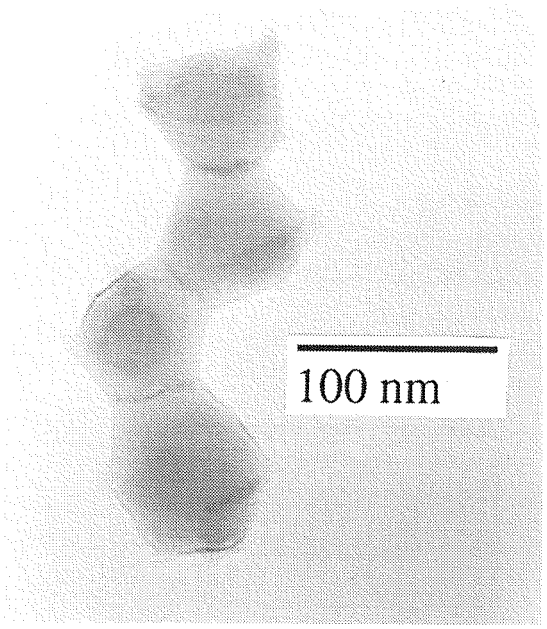

Figure 5.24: An agglomerate sintered at 1100°C that shows uniformity in dihedral angle.

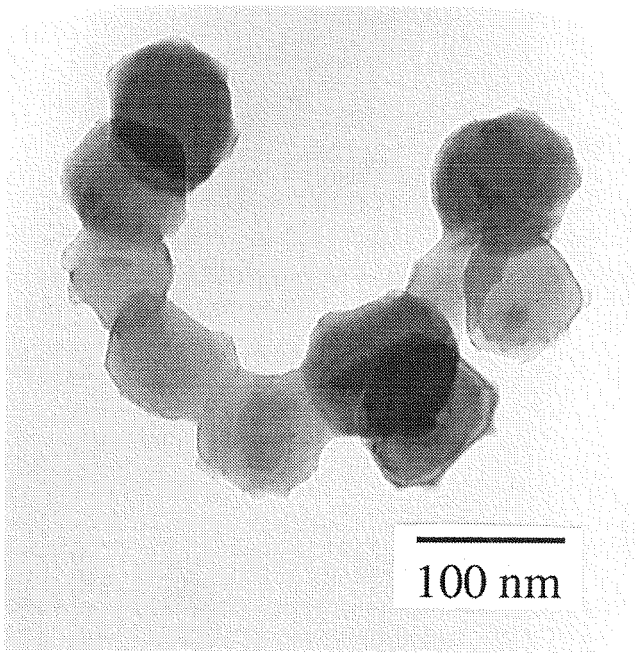

Figure 5.25: An agglomerate sintered at 1100°C that may have "bent" during sintering, increasing its mobility diameter.

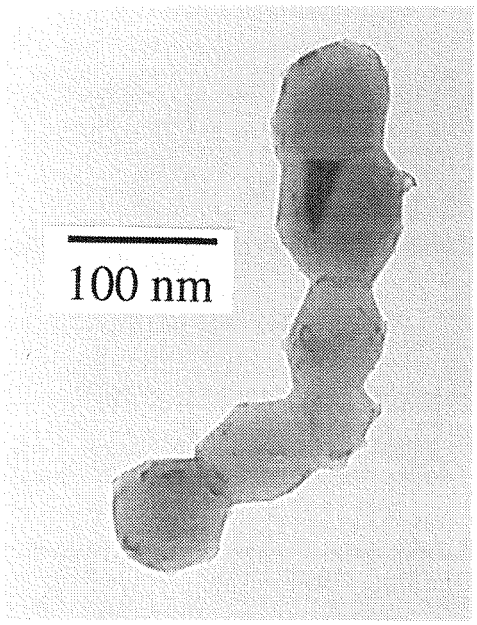

Figure 5.26: An agglomerate sintered at 1100°C with a slight bend that would increase its projected area.

Chapter 6

Conclusions

Sintering has lately been recognized as an important process in the aerosol synthesis of refractory particles from the vapor phase. The rate at which aerosol agglomerates coalesce is determined by the sintering kinetics, therefore an understanding of these kinetics is necessary to predict the structure of the resulting particles. Previous investigators have proposed number of heuristic models that incorporate a coalescence term into the aerosol population balance equation. However, in the development of these terms, little attention has been paid to the fundamental processes and assumptions involved in describing sintering kinetics.

Sintering has been the subject of numerous theoretical investigations. Many simple theoretical models exist to describe the sintering kinetics. Historically, sintering models have derived power-law relationships for neck growth as a function of time. To derive these simple expressions, assumptions concerning particle morphology are made that limit their applicability to a neck size $x/a_i < 0.3$. Moreover, it has been necessary to consider only the contribution of a single material transport mechanism

to neck growth. Multiple transport mechanisms will, in general, contribute simultaneously to neck growth.

A model has been developed to overcome some of these limitations. The model solves the evolving geometry as particles sinter, allowing neck growth to be calculated beyond the small neck limit. Contributions due to multiple mechanisms are calculated by integrating the sum of the individual sintering mechanisms fluxes. The model tracks the contributions of the individual mechanisms to neck growth throughout the sintering process. Although the present work has focussed on isothermal conditions, the computer simulations are readily extended to variable temperature systems encountered in practical aerosol synthesis. The model does not yet extend to prediction of neck growth beyond the "pill" shape, when the neck surface becomes cylindrical. This extension will be needed to develop a complete description of refractory aerosol growth.

Aerosol techniques have been used to study sintering. Experiments performed on model bispheres of silicon show that neck formation occurs quickly, until the difference between the surface free energy and the grain boundary energy of the aggregate becomes small. This metastable configuration of the particle system depends upon the equilibrium, or dihedral, angle for the material. Following the neck growth, coalescence proceeds slowly through interparticle mass transport.

The apparent existence of two "growth regimes" in sintering has important ramifications for aerosol growth. An aggregate will spend most of its time in this second coarsening phase of coalescence. It is logical to assume that the characteristic times

for the two regimes will differ. The development of a coalescence term for inclusion in the aerosol dynamic equations must take this complexity into account.

The projected area and, hence, the mobility-equivalent diameter of an agglomerate will generally decrease as coalescence occurs, although experimental observations reveal some unexpected behavior including apparent increases in the mobility-equivalent size. These effects may be caused by particle orientation in the mobility classifier. Hence, particle morphology cannot be determined by mobility measurements alone. To explain increases in projected area during sintering, it is postulated that the rotation of individual particles to preferred grain boundary orientations.

These experimental investigations lead to more questions than answers, suggesting many possibilities for continuing work. It is important to extend the sintering studies to other materials. Silicon is generally considered difficult to sinter. Metals or other refractory materials would allow different transport mechanisms to be explored. In order to minimize the ambiguity in reconciling experimental observations with theory, materials should be selected for which the material properties are relatively well established.

Two specific phenomena, the coarsening phase of coalescence and the observed mobility increase upon heating, beg for more experimental investigation. Bispheres can be produced with specific particle sizes and particle size ratios using two mobility classified dense particle streams. Heating times need to be expanded, and/or particle size decreased, so that both neck formation and ultimate coalescece both be observed experimentally. In addition, experiments with agglomerates that proceed past their

first generation primary particle size are needed to determine how the primaries evolve during coalescence. In particular, experiments that can discriminate between the separate neck growth and coalescence phases are needed.

Additional mobility size investigation should be performed with agglomerates of different primary particle sizes to determine the role of this important structure parameter in sintering. Different materials with different predominant sintering mechanisms may also affect the individual particles ability to rearrange during neck growth. Results from model agglomerates should be compared to aggregates resulting from combined coagulation/coalescence growth. These aggregates already have significant neck growth and may not show an mobility diameter increase during sintering.

A more efficient means of collecting samples for microscopy is needed. Electrostatic collection should prove viable since in many cases the particles already carry a charge. Preliminary attempts have yielded promising results. In addition, high resolution imaging of the grain boundary between sintered particles should be performed to determine if there is a preferred orientation for neck growth.

Bibliography

[1] W.D. Kingery, H.K. Bowen, and D.R. Uhlmann. *Introduction to Ceramics.* John Wiley and Sons, second edition, 1976.

[2] J. Frenkel. Viscous flow of crystalline bodies under the action of surface tension. *Journal of Physics U.S.S.R.*, 4(5):385–391, 1945.

[3] G.C. Kuczinski. Self-diffusion in sintering of metallic particles. *Trans. Amer. Inst. Min. (Metall.) Engr.*, 185:169–178, 1949.

[4] W.D. Kingery and M. Berg. Study of the initial stages of sintering solids by viscous flow, evaporation-condensation, and self-diffusion. *J. Appl. Phys.*, 26(10):1205–1212, 1955.

[5] J.G.R. Rockland. On the rate equation for sintering by surface diffusion. *Acta Metallurgica*, 14:1273–1279, 1966.

[6] J.G.R. Rockland. The determination of the mechanism of sintering. *Acta Metallurgica*, 15:277–286, 1966.

[7] D.L. Johnson. New method of obtaining volume, grain-boundary, and surface diffusion coefficients from sintering data. *J. Appl. Phys.*, 40(1):192–200, 1968.

[8] F.A. Nichols and W.W. Mullins. Morphological changes of a surface of revolution due to capillarity-induced surface diffusion. *J. Appl. Phys.*, 36(6):1826–1835, 1965.

[9] F.A. Nichols. Coalescence of two spheres by surface diffusion. *J. Appl. Phys.*, 37(1):2805–2808, 1966.

[10] P. Bross and H.E. Exner. Computer simulation of sintering processes. *Acta Metall.*, 27:1013–1020, 1979.

[11] F. Amar, J. Bernholc, R.S. Berry, J. Jellineck, and P. Salamon. The shape of first-stage sinters. *J. Appl. Phys.*, 65(8):3219–3225, 1989.

[12] B.J. Kellett and F.F. Lange. Thermodynamics of densification: I, Sintering of simple particle arrays, equilibrium configurations, pore stability, and shrinkage. *Journal of the American Ceramic Society*, 72(5):725–734, 1989.

[13] F.F. Lange and B.J. Kellett. Thermodynamics of densification: II, Grain growth in porous compacts and relation to densification. *Journal of the American Ceramic Society*, 72(5):735–741, 1989.

[14] L.R. Madhavrao and R. Rajagopalan. Monte carlo simulations for sintering of particle aggregates. *Journal of Materials Research*, 4(5):1251–1256, 1989.

[15] H.J. Leu, T. Hare, and R.O. Scattergood. A computer simulation method for particle sintering. *Acta Metallurgica*, 36(8):1977–1987, 1988.

[16] G.W. Scherer. Sintering of low-density glasses: I, Theory. *Journal of the American Ceramic Society*, 60:236–239, 1977.

[17] Y. Hiram and A. Nir. A simulation of surface tension driven coalescence. *Journal of Colloid and Interface Science*, 95(2):462–470, 1983.

[18] H.K. Kuiken. Viscous sintering: the surface-tension-driven flow of a liquid form under the influence of curvature gradients at its surface. *Journal of Fluid Mechanics*, 214:503–515, 1990.

[19] A. Jagota and P.R. Dawson. Simulation of the viscous sintering of two particles. *Journal of the American Ceramic Society*, 73(1):173–177, 1990.

[20] J.I. Martinez-Herrera and J.J. Derby. Viscous sintering of spherical particles via finite element analysis. *Journal of the American Ceramic Society*, 78:645–649, 1995.

[21] G.D. Ulrich, B.A. Milnes, and N.S. Subramanian. Particle growth in flames II. Experimental results for silica particles. *Combustion Science and Technology*, 14:243, 1976.

[22] G.D. Ulrich and N.S. Subramanian. Particle growth in flames III. Coalescence as a rate-controlling process. *Combustion Science and Technology*, 17:119–126, 1977.

[23] W. Koch and S.K. Friedlander. The effect of particle coalescence of the surface area of a coagulating aerosol. *Journal of colloid and Interface Science*, 140(2):419–427, 1990.

[24] A. Kobata, K. Kusakabe, and S. Morooka. Growth and transformation of TiO_2 crystallites in aerosol reactor. *AIChE Journal*, 37(3):347–359, 1991.

[25] Y. Xiong and S.E. Pratsinis. Formation of agglomerate particles by coagulation and sintering. 1. A 2-dimensional solution of the population balance equation. *Journal of Aerosol Science*, 24:283–300, 1993.

[26] Y. Xiong and S.E. Pratsinis. Formation of agglomerate particles by coagulation and sintering. 2. The evolution of the morphology of aerosol-made titania, silica, and silica-doped titania powders. *Journal of Aerosol Science*, 24:301–313, 1993.

[27] M.K. Wu, R.S. Windeler, C.K.R. Steiner, T. Bors, and S.K. Friedlander. Controlled synthesis of nanosized particles by aerosol process. *Aerosol Science and Technology*, 19:527–548, 1993.

[28] T. Seto, M. Shimada, and K. Okuyama. Evaluation of sintering of nanometer-sized titania using aerosol method. *Aerosol Science and Technology*, In Press.

[29] R.L. Coble. Initial sintering of alumina and hemitite. *Journal of the American Ceramic Society*, 41:55–62, 1958.

[30] B.H. Alexander and R.W. Balluffi. The mechanisms of sintering of copper. *Acta Metallurgica*, 5:666–677, 1957.

[31] G.C. Kuczinski. Measurement of self-diffusion of silver without radioactive tracers. *J. Appl. Phys.*, 21:632–635, 1950.

[32] H. Exner. Principles of single phase sintering. *Rev. Powder Metall. and Phys. Ceram.*, 1:1–251, 1979.

[33] Conyers Herring. *The Physics of Powder Metallurgy*, pages 143–179. McGraw Hill Book Co., 1951.

[34] J. Bardeen and C. Herring. *Atom Movements*, pages 87–111. American Society for Metals, 1951.

[35] D.L. Johnson. Solid state sintering models. In G.C. Kuczinski, editor, *Sintering Processes*, pages 97–106. Plenum, 1980.

[36] D.L. Johnson and T.M. Clarke. Grain boundary and volume diffusion in the sintering of silver. *Acta Metallurgica*, 12:1173–1179, 1964.

[37] G.D. Ulrich. Theory of particle formation and growth in oxide synthesis flames. *Combustion Science and Technology*, 4:47–57, 1971.

[38] K Okuyama, Y. Kousaka, N. Tohge, S. Yamamoto, J.J. Wu, R.C. Flangan, and J.H. Seinfeld. Production of ultrafine metal oxide aerosol particles by thermal decomposition of metal alkoxide vapors. *AIChE Journal*, 32:2010–2019, 1986.

[39] K. Okuyama, J.T. Jeung, Y. Kousaka, H.V. Hguyen, J.J Wu, and R.C. Flagan. Experimental control of ultrafine TiO_2 particle generation from thermal decomposition of titanium tetraisopropoxide vapor. *Chemical Engineering Science*, 44:1369–1375, 1989.

[40] J.J. Helble and A.F. Sarofim. Factors determining the primary particle size of flame-generated inorganic aerosols. *Journal of Colloid and Interface Science*, 128(2):348–362, 1989.

[41] M. Shiojiri, C. Kaito, H. Sasaki, and K Fujita. Coalescence growth of metal smoke particles prepared by gas evaporation. *Journal of Crystal Growth*, 52:168–172, 1981.

[42] H.G. Scheibel and J. Porstendörfer. Generation of monodisperse Ag- and NaCl-aerosols with particle diameters between 2 and 300 nm. *Journal of Aerosol Science*, 14(2):113–126, 1983.

[43] C. Roth. Generation of ultrafine gold aerosols. *Journal of Aerosol Science*, 17(3):447–480, 1986.

[44] F.E. Kruis, K.A. Kusters, S.E. Pratsinis, and B. Scarlett. A simple model for the evolution of the characteristics of aggregate particles undergoing coagulation and sintering. *Aerosol Science and Technology*, 19:514–526, 1993.

[45] K.S. Hwang and R.M.German. Analysis of initial stage sintering by computer simulation. In *Sintering and Heterogeneous Catalysis*, pages 35–47, 1983.

[46] F.B. Swinkels and M.F. Ashby. A second report on sintering diagrams. *Acta Metallurgica*, 29:259–281, 1981.

[47] R.M. German and Z.A. Munir. *Met. Trans.*, 68:289, 1975.

[48] D. Kahaner, C. Moler, and S. Nash. *Numerical Methods and Software.* Prentice Hall, 1989.

[49] W.H. Press, S.A. Teukolsky, W.T. Vetterling, and B.P. Flannery. *Numerical Recipies in Fortran.* Cambridge University Press, second edition, 1992.

[50] C.L. Yaws, L.L Dickens, R. Lutwack, and G. Hsu. Semiconductor industry silicon: Physical and thermodynamic properties. *Solid State Technology*, pages 87–92, 1981.

[51] Wayne M. Robertson. Thermal etching and grain-boundary grooving of silicon ceramics. *Journal of the American Ceramic Society*, 64(1):9–13, 1981.

[52] Kalinowksi and Sequin. *Applied Physics Letters*, 35:211, 1979.

[53] T.L. Wilson and P.G. Shewmon. The role of interfacial diffusion in the sintering of copper. *Transactions of the Metallurgical Society of AIME*, 236:48–58, 1966.

[54] D. Phillips and G. Vogt. Plasma synthesis of ceramic powders. *MRS Bulletin*, pages 54–58, 1987.

[55] C. Pickles and A. McLean. Production of fused refractory oxide spheres and ultrafine oxide particles in an extended arc. *Journal of the American Ceramic Society*, 62:1004–1009, 1983.

[56] S.L. Girshick and C.P. Chu. Homogeneous nucleation of particles from the vapor phase in thermal plasma synthesis. *Plasma Chem. Plasma Process*, 9:355–369, 1989.

[57] K. Kijima, H. Noguchi, and M. Konishi. Sintering of ultrafine SiC powders prepared by plasma cvd. *Journal of Materials Science*, 24:2929–2933, 1989.

[58] W.R. Cannon, S.C. Danforth, J.H. Flint, J.S. Haggerty, and R.A. Marra. Sinterable ceramic powders from laser-driven reactions. *Journal of the American Ceramic Society*, 65:324–335, 1982.

[59] J.J. Wu, H.V. Nguyen, and R.C. Flagan. *Langmuir*, 3:266, 1987.

[60] N.A. Fuchs. *The Mechanics of Aerosols.* Pergamon Press, 1964.

[61] S.C. Wang and R.C. Flagan. Scanning electrical mobility spectrometer. *Aerosol Science and Technology*, 13:230–240, 1990.

[62] S.N. Rogak and R.C. Flagan. The mobility and structure of aerosol agglomerates. *Aerosol Science and Technology*, 18:25–47, 1993.

[63] C. Greskovich and J.H. Rosolowski. Sintering of covalent solids. *Journal of the American Ceramic Society*, 59(7–8):336–343, 1976.

[64] Conyers Herring. Effect of change of scale on sintering phenomena. *J. Appl. Phys.*, 21:301–303, 1949.

[65] N.J. Shaw and A.H. Heuer. On particle coarsening during sintering of silicon. *Acta Metallurgica*, 31:55–59, 1983.

[66] H.J. Möller and G. Welsch. Sintering of ultrafine silicon powder. *Journal of the American Ceramic Society*, 68(6):320–325, 1985.

[67] W.P. Coblenz. The physics and chemistry of the sintering of silicon. *Journal of Materials Science*, 25:2754–2764, 1990.

[68] W. Koch and S.K. Friedlander. Particle growth by coalescence and agglomeration. *Part. Syst. Charact.*, 8:86–89, 1991.

[69] S.N. Rogak and R.C. Flagan. Cogulation of aerosol agglomerates in the transition regime. *Journal of Colloid and Interface Science*, 151:203–224, 1992.

[70] S.N. Rogak and R.C. Flagan. Stokes drag on self-similar clusters of spheres. *Journal of Colloid and Interface Science*, 134:206, 1990.

[71] J.E. Bonevich and L.D. Marks. The sintering behavior of ultrafine alumina powers. *Journal of Materials Research*, 7(6):1489–1500, 1992.